27. Electrochemical Hydrogen Production

Ting He, Mahaprasad Kar, Neal D. McDaniel, Bruce B. Randolph

The electrochemical−photoelectrochemical production of hydrogen has been widely investigated for decades, largely driven by the potential to reduce environmental impact, satisfy distributed demand, and enhance public perception. As an alternative to steam methane reforming for hydrogen production, these approaches have enjoyed renewed vigor over the last several years. This chapter reviews recent progress in low-temperature electrolysis, high-temperature electrolysis, and photoelectrochemical techniques. Perspectives are given on the electricity consumption, carbon dioxide emission, costs of hydrogen production, and competitive landscape in the future hydrogen market.

Part E | 27

The modern hydrogen market is almost entirely satisfied by steam methane reforming (SMR). Originating in the 1920s, hydrogen production by SMR involves the well understood, thermally driven oxidation of methane by steam, producing hydrogen gas and carbon dioxide. Owing to the maturity of the field, the material and energy efficiencies of SMR have been extensively optimized. In addition, SMR has a long track record of reliable operation, which is of utmost importance to the commodity industries that rely heavily on it for a steady supply of hydrogen. The feedstock, methane, is currently in plentiful supply due in large part to recent implementation of shale gas technology, making it difficult to envision competing with this inexpensive source of both hydrogen and energy [27.1].

However, some key drawbacks must also be acknowledged when considering SMR to supply hydrogen. Chief among these is the low cost-scaling factor (≈ 0.7) of a conventional reformer [27.2]. Optimized for refinery-scale production volumes, these reformers scale up much more affordably than they scale down. For distributed or small-scale applications, SMR is a relatively expensive option. This problem is exacerbated by the necessity for operating at high temperatures ($700-850\,^\circ$C) [27.3], requiring reliable material

performance and also significant fuel consumption for process heat. Additionally, the hydrogen produced by SMR is accompanied at $\approx 20\%$ volume by carbon dioxide and trace carbon monoxide. If the downstream, hydrogen-consuming process requires pure hydrogen, the product of an SMR must first be purified (conventionally using a pressure-swing adsorber or amine-based solvent) and cleaned up, and then delivered to the consumer. Finally, SMR produces carbon dioxide both as part of the stoichiometric process and in the generation of heat necessary to drive the reaction. In a hypothetical economic environment that penalizes carbon dioxide emission, SMR-derived hydrogen could be significantly disadvantaged relative to low-carbon, competing technologies. Electrolysis of water may prove to be a viable alternative to SMR in specific applications. First, most methods of electrochemical hydrogen production have cost-scaling factors that are closer to unity (≥ 0.85) [27.4]. This may enable them to compete fiscally against the conventional SMR when production scale is small, for instance in neighborhood or otherwise distributed production. Second, electrolytic hydrogen production usually generates pure hydrogen, requiring little or no downstream gas separation. The most anticipated impurity is water, which can

be conveniently and inexpensively removed. Most electrochemical hydrogen production methods are capable of operating over a wide range of pressures, and water can be removed from the products without necessitating a pressure drop. Also, the oxygen byproduct of water electrolysis, collected separately from the hydrogen, is a useful co-product that can be sold for use in a variety of industrial processes, such as welding, oxy-firing, and chemical oxidation. Finally, electrolysis is not directly accompanied by carbon dioxide. Because the vast majority of the power is being supplied electrically (a small amount is thermal, but $\approx 25\%$ thermal energy in high-temperature electrolysis (HTE)), electrolysis of water potentially has a flexible carbon budget. It may be powered by conventional coal, emerging wind and/or solar, or any intermediary power source. The carbon footprint associated with hydrogen from electrolysis is due in very large part to the carbon associated with electricity generation.

The first instance of water electrolysis is credited to an experiment performed by van Troostwijk and Deiman in 1789, powered by an electrostatic generator [27.5, 6]. In 1800, Alessandro Volta invented the first battery [27.7], allowing Nicholson and Carlisle to repeat the electrolysis of water 11 years after it was first reported, this time powered by several batteries in series [27.8]. Michael Faraday, one of the founders of electrochemistry, published in 1834 the laws of electrolysis and popularized the terms anode, cathode, electrode, and ion [27.9]. The first industrial electrolyzer based on a filter-press design was presented in Zurich in 1900 [27.10]. By 1902, there were more than 400 industrial water electrolyzers in operation. The increasing demand for ammonia in the fertilizer industry continued to expand electrolyzer service into the 1920s and 1930s, at which time steam reforming was only just starting to be commercialized. Norway and Canada built numerous hydropower-based electrolysis plants exceeding 100 MW of installed power [27.11]. In 1939, the first large-scale water electrolysis plant was built, with a hydrogen generation capacity of $10\,000\,\mathrm{Nm^3/h}$. Pressurized electrolysis was developed and patented by *Noeggerath* in the early 1930s [27.12, 13]. In 1948, Zdansky designed the first pressurized industrial electrolyzer. Following Zdansky's technology, a German company called Lurgi produced and distributed high-pressure electrolyzers (3 MPa) starting in 1951 [27.14]. Currently, there are five major commercial vendors providing high-pressure alkaline electrolyzers: StatOil (Norsk Hydro, Stavanger, Norway), Hydrogenics (Stuart, Mississauga, Canada), ELT, Teledyne (CA, USA), and Avalence (CT, USA) [27.15].

A different methodology toward electrolysis was unlocked in the development of solid electrolytes by General Electric (CT, USA) as part of the space program in 1966 [27.16]. This breakthrough gave birth to the field of proton exchange membrane (PEM) or solid polymer electrolysis. Sulfonated polystyrene and subsequently Nafion, a sulfonated perfluorinated material patented by DuPont [27.17], were developed for the purpose with the latter prevailing in PEM research up to the present day. Small-scale PEM water electrolyzers were used for military and space applications in the early 1970s. In 1987, the first 100 kW PEM electrolyzer was built by BBC (now ABB). Currently, there are a few manufacturers that offer commercial PEM electrolyzers with hydrogen production rates as high as $30\,\mathrm{Nm^3/h}$, namely Proton Energy Systems, StatOil, and Hydrogenics.

HTE is most often accomplished by the use of solid oxide-based electrolysis cells and stacks (SOEC). SOEC technology emerged from the development of solid oxide fuel cells (SOFC), with the idea that, rather than utilizing a fuel to make electrical power, the reverse operation of using electrical power to produce a fuel (H_2) is possible. This process normally uses steam as the feed, and performed at temperatures of $750-900\,^{\circ}\mathrm{C}$. Pioneering work in this area dates back to the late 1960s [27.18] in Germany and the United States. In the 1980s, *Doenitz* and coworkers reported results from the *Hot Elly* project [27.19] and Westinghouse researchers also published work with tubular cell designs [27.20]. These early forays into SOEC technology development waned due to a combination of lower energy prices and technical challenges. However, in the past decade, interest has renewed in this area, due to significant technical progress using planar cells based on SOFC technology [27.21].

HTE using SOECs provides several benefits over low-temperature electrolysis technologies. high-temperature operation requires decreased electricity consumption. This lower electricity demand is offset by higher heat demand required to maintain the high temperature. However, when high-temperature heat is available at low cost, HTE offers a favorable energy balance compared to low-temperature alternatives. Additionally, operating an electrolyzer at high temperatures favors the reaction kinetics and therefore less noble (less expensive) materials such as Ni and conductive oxides can be used instead of Pt as electrocatalysts.

Recently, a new field of study has emerged in which water electrolysis is powered by light. This is a photoelectrochemical (PEC) process, originated from *Becquerel's* 1839 discovery that electrodes covered in a layer of silver halide exhibit an electrical response to illumination [27.22]. The first physical explanation for this *Becquerel effect* is attributed to Brattain and Garrett of Bell Labs, 1955. Studying germanium and silicon

electrodes, *Brattain* and *Garrett* were able to elucidate the underlying photovoltaic process behind the operation of PEC for the first time [27.23]. This work led into the investigation of PEC for chemicals production and power generation over the following decades [27.24]. Hydrogen production from the PEC decomposition of water was first proposed in 1972 by *Fujishima* and *Honda* who observed that the electrical component of water electrolysis could be greatly reduced by the utilization of ultraviolet light [27.25]. Since the time of that finding, the pursuit of PEC hydrogen production has grown into a vast body of research.

The water electrolysis technologies can be divided into three distinct categories, based on commercial availability. The first of these, referred to herein as low-temperature electrolysis, is already commercial and is the most mature of all the electrolysis categories. The second, HTE, is approaching the crossroads of commercialization, but challenges remain. The third of these technologies, photoelectrolysis, is the youngest and farthest from commercialization. This chapter reviews the recent development of electrochemical hydrogen production technologies, particularly in these three areas.

## 27.1 Theoretical Aspects of Electrochemical Hydrogen Production

Electrochemical energy conversion takes place from electrical to chemical energy in electrolyzers, and from chemical to electrical energy in power sources. The consumption of electric power in the former case, and the production of electric power in the latter, are proportional to $U \times I$, where U is the potential difference (voltage) applied to or existing at the terminals of the cell as current I flows across the cell. Generally, the goal is to minimize U in electrolyzers and maximize U in power sources, for a given I. The efficiency and rate of energy conversion are governed by two controlling factors: the first of these is the kinetics of chemical reactions occurring at the electrode–electrolyte interface, and is subject to the activity of catalysts used. Situations in which slow chemical reactions limit overall energy conversion fall under the so-called Tafel regime. The second controlling factor is the availability and mobility of ionic species throughout the electrolyte. Scenarios in which the slow transport of ions limits overall energy conversion fall under the Ohmic regime. In the case of photoelectrochemistry, overall energy conversion is also affected by a third factor, namely the photovoltaic efficiency of the electrode. The limitations and characterization of these essential processes are discussed in this section.

27.1.1 Thermodynamics of Water Electrolyzers

Water electrolyzers convert electrical energy directly into chemical fuels, namely hydrogen, by the decomposition of water in acidic, basic, or neutral media. An electric power source is connected to two electrodes that are placed in water. Hydrogen evolves at the cathode (the negatively charged electrode), and oxygen is produced at the anode (the positively charged electrode). The amount of hydrogen generated is pro-

portional to the total electrical charge conducted by the solution, with two electrons yielding one molecule of hydrogen in the ideal Faradaic case. The thermodynamic efficiency of an electrolyzer depends on the energy needed to overcome kinetic barriers, known as overpotential, as well as the thermal energy required for elevated temperature operations.

Every electrolyzer must contain two electrodes separated by an electrolyte and be connected to an external power source (aside from photoelectrolysis). Ions flow through the electrolyte from one electrode to the other, and electrons travel through the external conducting circuit, requiring electromotive force to drive the process. For water electrolysis in acidic media (e.g., using a PEM), a water oxidation reaction takes place at the positively charged anode, generating oxygen gas and giving electrons to the anode; whereas at the negatively charged cathode, a reduction of protons occurs, forming hydrogen gas and completing the external conducting circuit. At the interface between the electrode and electrolyte, the flow of current is continuous, but the identity of the charge-carrying species changes from an electron to a proton (H^+). The half-cell reactions at anode and cathode are

$$2H_2O \rightarrow O_2 + 4H^+ + 4e^- \quad \text{(anode)}, \quad (27.1)$$
$$2H^+ + 2e^- \rightarrow H_2 \quad \text{(cathode)}. \quad (27.2)$$
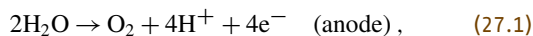
Combining these half-cell reactions yields the overall decomposition of water into oxygen and hydrogen
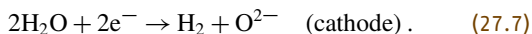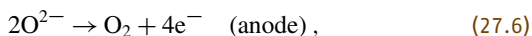
$$2H_2O \rightarrow 2H_2 + O_2 . \quad (27.3)$$

For water electrolysis in alkaline media (either liquid alkaline solution or a solid anion exchange membrane), the corresponding half-cell reactions at the anode and

cathode are

$$4OH^- \rightarrow O_2 + 2H_2O + 4e^- \quad \text{(anode)}, \quad (27.4)$$

$$2H_2O + 2e^- \rightarrow H_2 + 2OH^- \quad \text{(cathode)}, \quad (27.5)$$
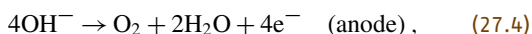
where hydroxide anions (OH^-) are now the charge-carrying species in the electrolyte. In the neutral case where a solid oxide membrane is used as the electrolyte (in HTE), the half-cell reactions at anode and cathode can be described as

$$2O^{2-} \rightarrow O_2 + 4e^- \quad \text{(anode)}, \quad (27.6)$$

$$2H_2O + 2e^- \rightarrow H_2 + O^{2-} \quad \text{(cathode)}. \quad (27.7)$$

It should be noted that, in practice, the electrochemical reactions in water electrolysis are more complicated than those described by the equations above. It is commonly agreed that each electrochemical reaction step involves only one electron and each reaction above involves multiple reaction steps and energy barriers.

The decomposition of water into hydrogen and oxygen is not thermodynamically favorable at standard temperature and pressure. The change of Gibbs free energy for the reaction in (27.3) has an ideal standard potential of -1.23 V at $25\,^\circ$C, which means that the reactions cannot occur without providing the necessary energy, usually supplied by an external electric power source. The 1.23 V is the minimum voltage needed to perform the water electrolysis, with the hydrogen production rates approaching zero. The actual cell voltage is much higher than this equilibrium value due to various irreversible losses, known as overpotentials, and depends on the hydrogen production rate as shown in Fig. 27.1.

The efficiency of any energy conversion device is defined as the ratio between useful energy output and energy input. In the case of an electrolyzer, the useful energy output is the enthalpy of hydrogen, that is, hydrogen's higher heating value (HHV) (W_{H_2}), and the energy input is the electrical (W_{el}) and thermal energies (W_{th}) used in electrolysis

$$\eta = \frac{\eta_{el}}{\left(1 + \frac{\eta_{el}}{\eta_{th}}\right)}, \quad (27.8)$$

where $\eta_{el} = W_{H_2}/W_{el}$ is the electrical efficiency and $\eta_{th} = W_{H_2}/W_{th}$ is the thermal contribution. If the amount of thermal energy input is very small (low-temperature electrolysis), the system efficiency is equivalent to the electrical efficiency. However, for the case of HTE, the thermal contribution term has to be taken into account. If a Faradaic efficiency of 100% is assumed for an electrolyzer operating at ambient
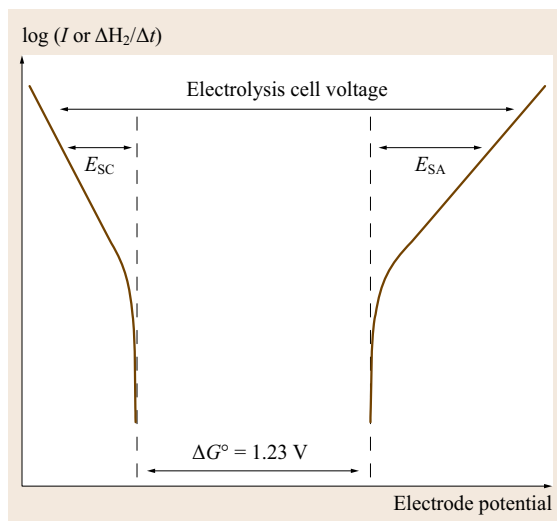

Fig. 27.1 The relationship between the hydrogen production rate and the overpotentials at the cathode and anode, where E_{SC} and E_{SA} are the surface overpotentials on the cathode and anode, respectively

conditions, the electrical efficiency can be defined as $1.482/U$, where U is the voltage applied to the cell and 1.482 is the thermoneutral voltage of water electrolysis at ambient conditions. It is noted that the maximum theoretical efficiency would be of no practical value, since an electrolysis cell operating at theoretical efficiency would generate negligible hydrogen.

Faraday's law relates the rate of reaction to the applied current. It states that the rate of production of a species is proportional to the current, and the total mass produced is proportional to the amount of charge passed multiplied by the equivalent weight of the species. For water electrolysis, Faraday's law can be written as

$$M_{H_2}(\text{g/(A s)}) = \frac{WI}{nF}, \quad (27.9)$$

where W is the formula weight of hydrogen (2.0159 g/mol), I is total current (in A), n is the number of electrons required to produce a molecule of hydrogen (27.2), and F is the Faraday constant (96 487 C/mol). The behavior of electrochemical systems is determined by the current density rather than by the total current, which is the product of the current density and the cross-sectional area (electrode area). From (27.9), the hydrogen production rate will be ≈ 9 kg hydrogen per day for every ampere of current (106 Nm³ hydrogen (Nm²/Ad)).

The hydrogen production rate from water electrolysis (27.9) is based on the assumption that the Faradaic efficiency for the cell is 100%. In the case of electrode

or membrane corrosion, charges are consumed without producing hydrogen, resulting in a lower Faradaic efficiency (η_F) and, hence, a lower system efficiency

$$\eta = \frac{\eta_{el}\eta_F}{\left(1 + \frac{\eta_{el}}{\eta_{th}}\right)} \ . \tag{27.10}$$

Under high operating potential and in aqueous solution, electrode corrosion can occur through a direct electrical dissolution of the metals or by an oxide formation and chemical dissolution of the oxide layers. The preference for one process over the others is a function of cell voltage and solution pH. Due to the instability of most metals and oxides at high electrochemical potentials, electrode corrosion is a chief concern in low-temperature electrolysis.

27.1.2 Chemical Kinetics at Electrodes

In electrochemical systems of practical importance, including corrosion, it is critical to understand the processes that occur at the electrode–electrolyte interface. Electrochemical reactions at an electrode involve both a transfer of electrical charge and a change in Gibbs free energy. The rate of electrochemical reaction is determined by the speed at which the electrons are consumed or released at the electrode surface, and is controlled by an energy barrier that the charge must overcome in order to transfer from a solid electrode to reactant species or vice versa. The rate of reagent consumption is proportional to their surface concentration. In the case of hydrogen reduction, (27.2), the flux J_{red} (mol/(s cm^2)) for the forward reaction and the flux J_{ox} for the backward reaction can be described by

$$J_{red} = k_{red}\,[H^+]^2 \ , \tag{27.11}$$
$$J_{ox} = k_{ox}\,[H_2] \ , \tag{27.12}$$

where k_{red} and k_{ox} are the reduction and oxidation rate coefficients that are functions of the Gibbs free energy, $k = k_B T/\hbar \exp(-\Delta G/RT)$, where k_B and $\hbar$ are Boltzmann's and Planck's constants, and $[H^+]$ and $[H_2]$ are the concentrations of the protons and hydrogen, respectively. The net charge transferred q (C/mol) is the difference between the electrons consumed and released

$$q = 2F\left(k_{red}[H^+]^2 - k_{ox}[H_2]\right) \ . \tag{27.13}$$

At equilibrium, the net charge transferred is equal to zero, although the reaction proceeds in both directions simultaneously. Therefore, for water electrolysis, a potential has to be applied to the hydrogen electrode to force current to flow; and the potential difference

between the hydrogen and oxygen electrodes is the driving force for the reactions shown in (27.1), (27.2), and (27.4)–(27.7). This driving force is termed the surface overpotential E_s. The rate of the reaction can often be related to the surface overpotential by

$$j = j_0 \left[\exp\left(\alpha_{ox}F\frac{E_s}{RT}\right) - \exp\left(\frac{-\alpha_{red}FE_s}{RT}\right)\right] \ , \tag{27.14}$$

where j_0 is the exchange current density, analogous to the rate constant used in chemical kinetics, and α is the transfer coefficient that is an additional parameter relating to how an applied potential favors one direction of the reaction over the other. Equation 27.14 is known as the Butler–Volmer equation, that is, a relationship between current and surface overpotential for an electrode. From the Butler–Volmer equation, the surface overpotential (E_s) at a given current density can be calculated, resulting in the overpotential plot shown in Fig. 27.1. For small values of E_s, the current density varies linearly with E_s, whereas the current density varies exponentially for large values of E_s. By plotting surface overpotential as a function of logarithm of current density, the well-known Tafel plot can be created.

The Butler–Volmer equation (27.14) can also be regarded as a result of cathodic and anodic reactions taking place independently, each with an exponential dependence on the corresponding surface overpotential. Generally speaking, the surface overpotential of a particular electrode reaction is related to the electrochemical potentials of reactants and products, for example, the surface overpotential for the reaction in (27.2) can be written as

$$E_s = -\frac{(\mu_{ec,H_2} - 2\mu_{ec,H^+} - 2\mu_{ec,e^-})}{2F} \ , \tag{27.15}$$

where $\mu_{ec,k}$ is the electrochemical potential of the species k consisting of chemical potential ($\mu_{c,k}$) and electrical potential (ϕ) by $\mu_{ec,k} = \mu_{c,k} + z_k F\phi$.

27.1.3 Transport in Electrolytes

The potential applied to an electrode creates a driving force for reactions at the electrode. The potential difference across two electrodes also creates a driving force for the flow of ionic species inside electrolyte. The driving force is the electric field (E), which is related to the gradient of potential ϕ by $E = -\nabla\phi$. The current density in electrolyte is the net flux of various charged species

$$j = \sum z_k Fjk \ , \tag{27.16}$$

where z_k and j_k are charge number and flux density of the ionic species k, respectively. While electrons in a conductor flow only in response to an electrical field, ionic species in an electrolyte move in response to an electric field (migration) and also in response to concentration gradients (diffusion) as well as bulk fluid motion (convection). The net flux of an ion is therefore the sum of the migration, diffusion, and convection terms. Very often, the transport of ionic species in electrolytes and/or the removal of product gases from electrodes are the rate-limiting processes.

The electric field, which creates a driving force for the movement of ionic species, drives cations toward the cathode and anions toward the anode, that is, cations move in the direction opposite to the gradient in potential. The flux density of a species is given by

$$j_{k,\mathrm{mig}} = -z_k u_k F [c_k] \nabla\phi \, , \tag{27.17}$$

where u_k is the mobility and $[c_k]$ is the concentration of the species k. Often, a transference number of an ion is reported for ionic species in electrolyte, which is defined as the fraction of the current that is carried by that ion in a solution of uniform composition $t_k = z_k F j_k / J$. For the case that the transference number of the reacting

ion is less than unity, there will be fluxes of the other ions in solution that will create a concentration gradient; this is particularly true for solution electrolytes. These concentration gradients drive mass transport by the process of diffusion, which occurs in addition to the process of migration above. The diffusional transport is a nonconvective flow that tends to equilibrate the concentrations in inhomogeneous nonequilibrium systems. The flux density of the diffusion can be described by the concentration gradient $\nabla[c_k]$

$$j_{k,\mathrm{dif}} = -D_k \nabla[c_k] \, , \tag{27.18}$$

where D_k is the diffusion coefficient of the species k. Equation (27.18) is incomplete for not specifying the reference frame of transport and neglecting the cross terms. The last one to be discussed is the convection term. Convection is the bulk movement of a fluid. The flux density of a species by convection is given by (27.19), where v is the velocity of the bulk fluid

$$j_{k,\mathrm{con}} = [c_k] v \, . \tag{27.19}$$

Convection includes natural convection which is caused by density gradient and forced convection caused by mechanical stirring or a pressure gradient. The latter is often used in practice to remove gases from electrodes to avoid electrode poisoning and to serve as an effective means to bring reactants to the electrode surfaces. However, in an electrically neutral solution, bulk convection alone does not cause a net current except affecting concentration profiles. Combining the migration (in *electrical units*; (27.17)) and diffusion (in *thermal units*; (27.18)) terms results in (27.20), where the term $\mu_{c,k} + z_k F\phi$ is the electrochemical potential of the species k ($\mu_{ec,k}$)

$$j_k = \frac{-D_k[c_k]}{RT} \nabla(\mu_{c,k} + z_k F\phi) \, . \tag{27.20}$$

Again, the interactions between ionic and electronic fluxes have been neglected by assuming that the cross coefficients in the matrix of the transport coefficients take zero value. By using (27.20), one can calculate the transport properties of charged species in electrolytes.

27.1.4 Temperature Effect

High-temperature steam electrolysis is most often accomplished with SOEC technology. At a very high level, SOEC operation is simply the reverse of SOFC operation. Instead of burning a fuel to provide electricity, electricity is used to produce hydrogen and oxygen from water splitting. A basic schematic of the process is shown in Fig. 27.2.
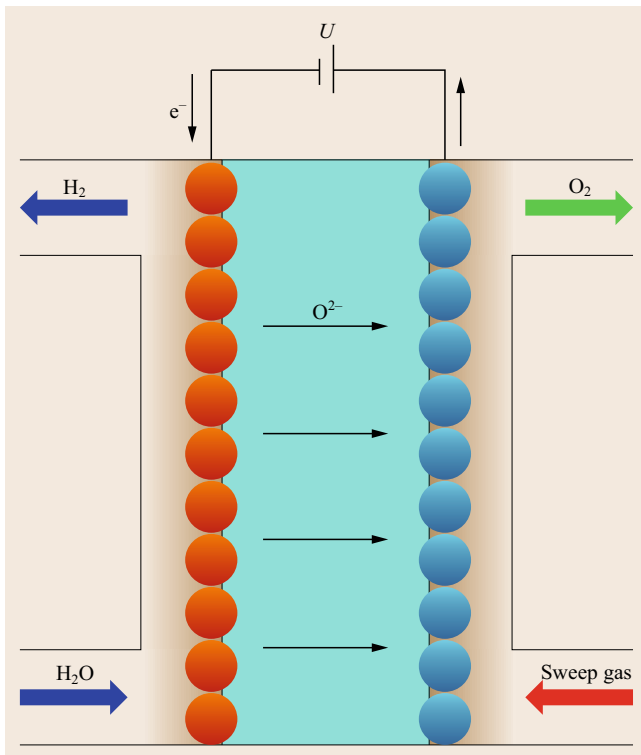

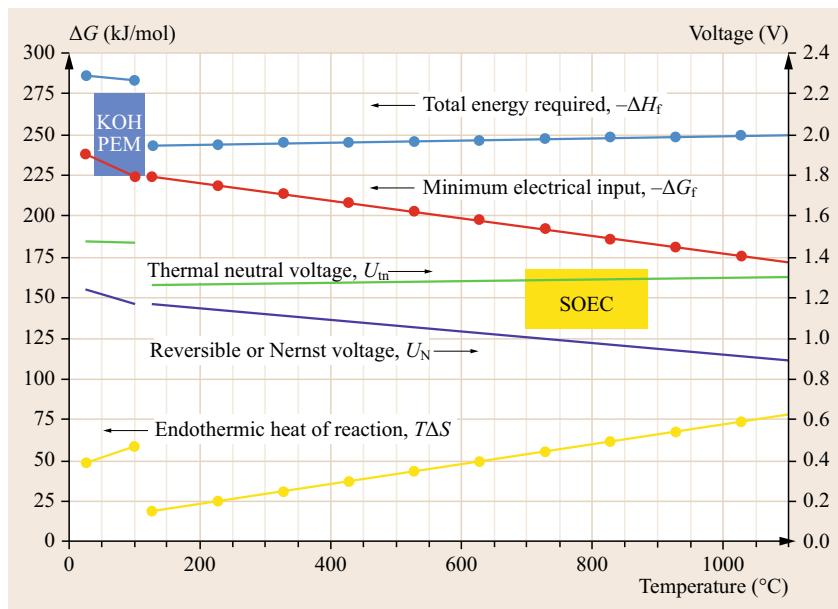**Fig. 27.2** Schematic of SOEC cell, with cathode on the *left* and anode on the *right*

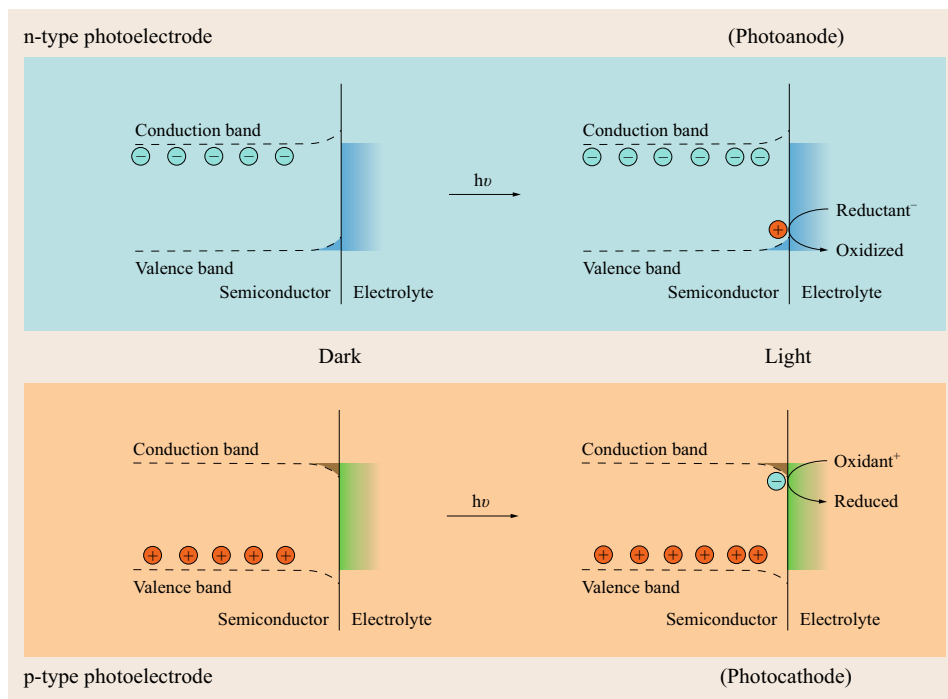**Fig. 27.3** Water-splitting thermodynamics (courtesy of Ceramatec)

Fig. 27.4 The photoresponses of an n-type and p-type photoelectrode

As in SOFC technology, there is a nonporous, dense, gas-tight electrolyte, sandwiched between an anode and a cathode. The electrolyte ideally has high oxygen anion (O^{2-}) conductivity, but low or no electronic conductivity. Both the anode and cathode are usually porous and have mixed ionic and electronic conduction. This allows gas reactants into the reaction sites

and establish a triple-phase boundary (TPB), where gas reactants, oxide ions, and electrons can react.

In SOEC mode, the cathode and anode reactions for hydrogen and oxygen production, respectively, are shown in (27.6) and (27.7). The overall water decomposition reaction (27.3) is governed by the Nernst equation (27.21), where ΔG^o is the Gibbs energy at standard

pressure and temperature, P_x are partial pressures of the gases, n is the number of electrons involved, and F is Faraday's constant

$$V = -\frac{\Delta G^{\circ}}{nF} - \left(\frac{RT}{nF}\right) \ln\left(\frac{\left(P_{H_2}^2 P_{O_2}\right)}{P_{H_2O}^2}\right) . \qquad (27.21)$$

At elevated temperatures, by taking into account the thermal energy, the minimum energy input required for water splitting is given by

$$\Delta G = \Delta H - T\Delta S , \qquad (27.22)$$

where ΔH and ΔS are the enthalpy and entropy for the water splitting reaction, respectively. It can be seen that the overall energy requirement decreases with increasing temperature. There are three basic operating regimes for SOEC: endothermic, exothermic, and thermoneutral [27.26] (Fig. 27.3). By virtue of electrical current passing through the cell, heat is generated due to internal resistances. When the electrical energy supplied to the cell is equal to the reaction enthalpy, the thermoneutral point is achieved, and this voltage is termed the thermoneutral voltage (U_{tn})

$$U_{tn} = \frac{\Delta H}{nF} . \qquad (27.23)$$

At the thermoneutral point, the gas outlet temperature is equal to the steam inlet temperature, and the electricity-to-hydrogen conversion efficiency is 100%. Entropy required for water splitting matches the heat generated by resistances and losses in the cell.

For the endothermic regime, the electrical potential applied to the system is below V_{tn}. As a result, additional energy (in the form of heat) must be supplied to maintain the desired temperature. Conversely, exothermic operations are those in which a potential greater than U_{tn} (energy input > ΔH) is supplied.

27.1.5 Photoelectrochemistry

Water electrolysis using solar energy occurs through a PEC process, whereby a semiconductor–electrolyte junction replaces the p–n junction of photovoltaic cell for charge separation. When a neutral, doped semicon-ductor is immersed in an electrolyte solution, its surface becomes charged. For positively doped (p-type) materials, equilibrium charge is reached when a small number of electrons are injected from the electrolyte into the easily accessible holes of the semiconductor's valence band, yielding a net negative charge in the solid. In contrast, the electrolyte removes a small number of easily accessible electrons from the conduction band of negatively doped (n-type) materials, leading to a net positive charge in the solid.

Polarization of the electrolyte then occurs at the surface of the electrode, resulting in band bending at the semiconductor–electrolyte interface in Fig. 27.4 [27.27]. This Schottky barrier, generated by bringing a doped semiconductor into contact with an appropriate electrolyte, is capable of separating electron/hole exciton pairs as they are formed, and therefore supplants the need for a solid-state p–n junction.

Under illumination, electrons begin to populate the conduction band of p-type semiconductors; meanwhile the number of holes in the valence band does not change appreciably considering the large number of holes that already existed under dark conditions. The converse is true when photons are absorbed by an n-type material: Accessible holes begin to appear in the valence band, meanwhile the number of electrons in the conduction band is largely unaltered. For all these reasons, p-type photoelectrodes thus exhibit a cathodic photoresponse (photocathodes) while n-type photoelectrodes exhibit an anodic response (photoanodes), as depicted in Fig. 27.4 [27.28].

For the water-splitting reaction, electrolyte pH is a controlling parameter. The electron affinity of an aqueous solution increases linearly with pH. For n-type materials, the semiconductor–electrolyte Schottky junction is therefore expected to be of greatest magnitude under acidic conditions, and to diminish as the pH increases. Meanwhile, the opposite behavior is expected for p-type electrodes. For this reason, it is important to note the reported conditions of operation for each study; from a survey of the most outstanding reports of PEC solar conversion efficiency for both photocathode [27.29] and photoanode [27.30], a minimal Schottky barrier appears to be favored (alkaline conditions are preferred for photoanodes, acidic conditions for photocathodes).

27.2 Electrochemical Hydrogen Production Methods

Three technologies define the scope of this chapter: low temperature, high temperature, and photo-driven electrolysis. Low-temperature electrolysis can be further dissected into that which uses a liquid electrolyte (usually referred to as alkaline electrolysis due to the preferred use of strongly alkaline conditions) and that which uses a solid, PEM electrolyte (usually referred to as PEM or acidic electrolysis, due to the acidic nature of the polymer membrane). HTE also operates using a solid electrolyte membrane, though utilizing very different materials for high-temperature compatibility. Finally, in photoelectrolysis there is negligible electrical power input, with the catch that the electrodes must now be photoactive in addition to electrocatalytic. Each of these practices faces a unique set of technical merits and challenges; the states of these fields are herein discussed.

27.2.1 Low–Temperature Electrolysis

Alkaline Electrolysis

Industrial scale electrolyzers may be broadly classified into unipolar (tank type) electrolyzers and bipolar (filter-press type) electrolyzers. In the tank-type electrolyzers, each cell consists of anodes and cathodes that are alternated and separated by diaphragms (Fig. 27.5). The electrodes are electrically connected outside the cell in parallel sets. This leads to a very simple design that provides easy maintenance, even during operation [27.11].

In filter-press electrolyzers, the electrodes are bipolar, with one face serving as an anode in one cell and the other as a cathode in the next cell (Fig. 27.5). A separator (binder) is present between the two cells. Diaphragms are used to separate gas collection spaces. By applying back pressure to the gas collection lines, filter-press electrolyzers can be operated to generate hydrogen and oxygen at pressures [27.14] For similar H_2 production rates, a filter-press electrolyzer is more compact and lightweight than a tank type electrolyzer. Moreover, less wiring is required as the current flows through the cells that are connected in series, (Fig. 27.5) [27.31–34].

Earlier designs exhibit the use of two separate electrodes with a separator or diaphragm in between. The ohmic loss associated with passing current through the electrolyte was reduced by appending the electrodes to the separator in the *zero-gap* electrode design introduced by *Costa* and *Grimes* in 1967 [27.35]. The design is a modified filter-press electrolyzer with porous nickel electrodes attached directly to a diaphragm (Fig. 27.6). For identical external dimensions, porous electrodes provide a higher specific surface area than nonporous electrodes for the electrochemical reactions. Furthermore, gas bubbles produced during electrolysis are pressurized to traverse the porous electrodes; hence the space between electrodes can be virtually kept free of bubbles. The electrolyte conductance is also increased as a result of the increase in operational temperature to about $110\,°C$. These operational features reduce various types of overpotentials and thus allow the electrolyzers to be operated at higher current density with improved electrical efficiency (Table 27.1) [27.31].

Materials. To attain low ohmic overpotentials, $25-30$ wt% KOH solution is typically used as the electrolyte in alkaline electrolyzers. Hence, the materials used require high corrosion resistance. Most of the electrolyzers also operate at slightly elevated temperatures ($70-90\,°C$). Under these conditions, nickel-plated steel provides adequate corrosion resistance as a containment material. The electrodes are typically made of a nickel or nickel-plated steel substrate with a catalyst coating.

Diaphragms are required to perform multiple functions: They keep hydrogen and oxygen from mixing, allow the electrolyte to permeate through, and have acceptable mechanical and electrochemical corrosion stability. Before being banned in all European countries, asbestos was considered as the most suitable candidate as a diaphragm. Recently, asbestos has been substituted by polymer-reinforced ceramic oxide composites. Zirfon is an example of a porous composite separator material composed of a polysulfone matrix and zirconia [27.37].

Table 27.1 Example operating parameters and performance data of different types of alkaline electrolyzers (after [27.31])

	Tank type	Filter press	Advanced zero-gap
Operating temperature (°C)	80−85	65−80	110
Operating pressure (atm)	−	30	20
Current density (A/cm^2)	0.04−0.06	0.07−0.3	0.85/1.7
Cell voltage (V)	1.90−2.40	−	1.78/1.99
Energy consumption (kWh/Nm^{3}H$_2$)	4.15−4.90	4.30−4.75	4.1
Efficiency (%)	60−70	63−70	73/83
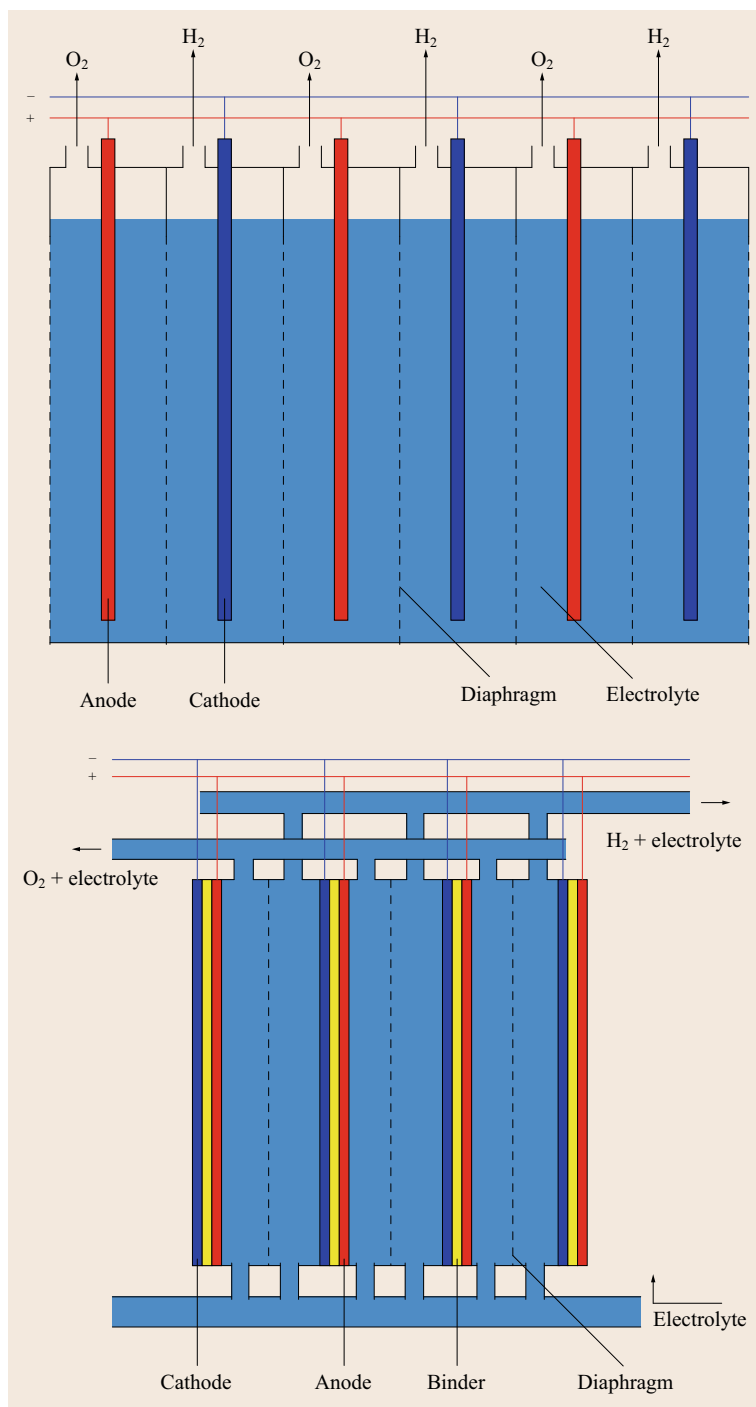
Fig. 27.5 Illustration of tank-type electrolyzer and filter-press type electrolyzer

Cathodic catalysts are primarily nickel based. Raney nickel has proven to be a good long-term stable catalyst at 80 °C. High surface-area nickel catalysts developed by *Raney* in 1925 are considered noteworthy contributions to the field of catalysis [27.39, 40]. The use of such catalysts in electrolyzers was patented by *Justi* et al. in 1954 [27.41]. Raney nickel was later used in a matrix of another metal (e.g., aluminum, zinc) to

Fig. 27.6 **(a)** Conventional electrolyzer configurations for gas-evolving electrodes, **(b)** zero-gap configuration with perforated plate electrodes pressed to either side of the diaphragm (after [27.36], courtesy of Wiley)
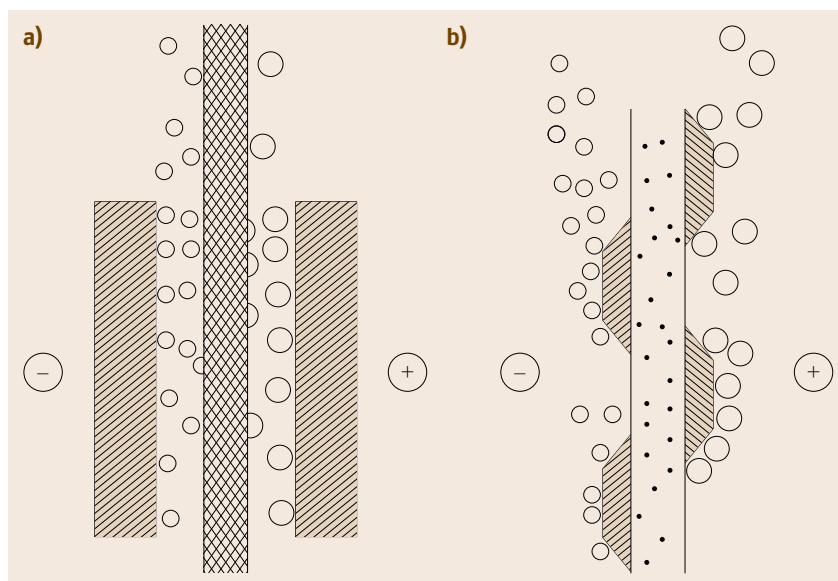
Table 27.2 Hydrogen overpotentials of different electrode materials (after [27.38], courtesy of Elsevier)

Composition formula	Method	T (°C)	Electrolyte	C (mol/dm^3)	j (A/m^2)	η_{hyd} (mV)
Ni–Fe–Mo–Zn	Codeposition	80	KOH	6	1350	83
Ni–S–Co	Electrodeposition	80	NaOH	28 wt%	1500	70
Ni50%-Zn	Electrodeposition	N/A	NaOH	6.25	1000	168
MnNi$_{3.6}$Co$_{0.75}$Mn$_{0.4}$Al$_{0.27}$	Arc melting	70	KOH	30 wt%	1000	39
Ti$_2$Ni	Arc melting	70	KOH	30 wt%	1000	16
Ni50%Al	Melting	25	NaOH	1	1000	114
Ni75%Mo25%	Codeposition	80	KOH	6	3000	185
Ni80%Fe18%	Codeposition	80	KOH	6	3000	270
Ni73%W25%	Codeposition	80	KOH	6	3000	280
Ni60%Zn40%	Codeposition	80	KOH	6	3000	225
Ni90%Cr10%	Codeposition	80	KOH	6	3000	445

improve the mechanical stability and the electrical conductivity of the electrode, consequently reducing the overpotentials.

Raney-type catalysts are synthesized by first preparing an alloy of the catalytically active catalyst (Ni, Co, Cu) with another support metal (Al, Zn). The support metal is then leached out in an alkaline solution, leaving behind a high surface area catalyst. Alternatively, high surface area Ni foams [27.42] and whiskers [27.43] have also been investigated as the cathode catalyst. Other compounds studied thus far include iron molybdates [27.44] and nickel molybdates [27.45], nickel borides, nickel sulfides, and nickel–cobalt thio-spinels. Adding 13% Mo to Ni improves the catalytic activity, and when doped with ceramics such as TiO$_2$ and ZrO$_2$ exhibits enhanced stability [27.46]. Applying these measures, the cathodic (hydrogen) overpotential at 1000 A/m^2 and 90 °C was reduced from 0.35 V down to 0.15−0.2 V. Non-nickel-based cathode catalysts such as PdTi, Hf$_2$Fe, Hf$_2$Co, PtMo$_3$, NbPd, and other transition metal alloys represent an important step toward the development of novel water reduction catalysts. Table 27.2 lists the hydrogen overpotentials (η_{hyd}) corresponding to various cathode catalysts.

Identifying efficient and stable anode catalysts has proven to be more challenging than cathode catalysts. The anode material has traditionally been made from nickel or nickel-coated steel, as it is inexpensive and corrosion resistant at positive potentials. However, a wide variety of materials have been investigated, as the overpotential associated with a Ni electrode can be as high as 20% (300−400 mV) of the overall cell voltage. At the end of 1970s, overpotentials of 150 mV less than Ni were achieved with polytetrafluoroethylene (PTFE)-bonded NiCo$_2$O$_4$; but the material exhibited long-term stability issues. In the 1980s, mixed oxides such as perovskites and spinels were examined. Nickel anodes with 2−3 mg/cm^2 of cobalt spinel demonstrated

Table 27.3 Oxygen overpotentials of different electrode materials

Composition formula	Method	T (°C)	Electrolyte	C (mol/dm^3)	j (A/m^2)	η_{oxy} (mV)
Ni + Spinel-type Co$_3$O$_4$	Thermodecomposition	25	KOH	1	1000	235± 7
Ni + La-doped Co$_3$O$_4$	Thermodecomposition	25	KOH	1	1000	224± 8
MnOx-modified Au	Electrodeposition	25	KOH	0.5	100	300
Li10% doped CO$_3$O$_4$	Spray pyrolysis	RT[a]	KOH	1	10	550
Ni	N/A	90	KOH	50 wt%	1000	300
La$_{0.5}$Sr$_{0.5}$CoO$_3$	Spray-stiner	90	KOH	50 wt%	1000	250
Ni$_{0.2}$Co$_{0.8}$LaO$_3$	Plasma jet projection	90	KOH	50 wt%	1000	270

[a] Room temperature
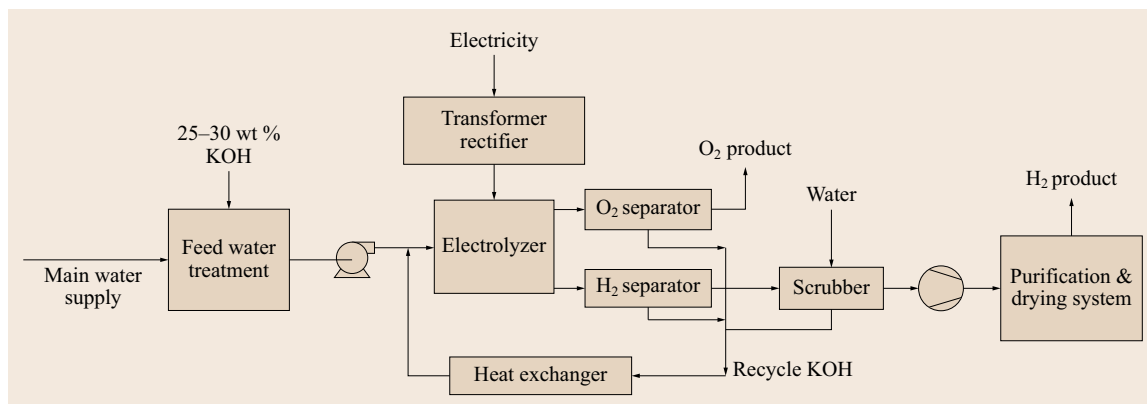
Fig. 27.7 Schematic of an alkaline water electrolysis plant (after [27.31–34])

80 mV lower overvoltage compared to plain Ni. In the mid 1980s, perovskites and spinels containing transition metals such as Ni$_2$Co$_4$, La$_{0.2}$Sr$_{0.8}$CoO$_3$, and Co$_3$O$_4$ were identified as promising catalysts owing to their activity, long-term stability, and affordability. To date, these transition metals based oxides have proven to be the most successful anode catalysts in operation. Table 27.3 lists the oxygen overpotentials (η_{oxy}) corresponding to various anode catalysts and electrolysis conditions.

Process Flow and Operating Conditions. The electrolyte, a 25−30 wt% aqueous KOH solution, is pumped into the electrolyzer. The transformer–rectifier converts the AC high-voltage supply into DC current input that is applied across the electrodes. Hydrogen and oxygen are produced in the electrolyzer via water electrolysis. The gases bubble up through the electrolyte to be conveyed by internal ducts into separation tanks at the front of the electrolyzer. This module consists of two gas separators, one each for O$_2$ and H$_2$, and the electrolyte recirculation system. In the separators, the electrolyte is recovered and is then chilled in the heat exchanger and recycled into the cell block.

The separated H$_2$ gas is sent to the scrubber to remove residual traces of the electrolyte and to re-

duce the temperature of the gas. The liquid from the scrubber containing the electrolyte is recycled into the electrolyzer. The hydrogen gas is compressed to the required level by one or more compressors. After the gas scrubber, the hydrogen has a purity of 99.9%. If higher purity is desired, the gas is further treated in the purification and drying system. The impurities primarily consist of oxygen and water (in addition to nitrogen). The oxygen is removed by a catalytic recombination with hydrogen in a deoxidizer. The gas is dehydrated by twin absorption towers packed with desiccant to absorb the water. One tower is always in operation, while the other one is being regenerated. The result is very high purity hydrogen – up to 99.993%, depending on the plant configuration. Optionally, a pressurized hydrogen storage system can be installed. A generic schematic is given in Fig. 27.7.

The applied voltage is a key parameter as it establishes the electrical efficiency and the power consumption of the electrolyzer. Current density is another important parameter that affects the efficiency directly. A higher current density directly results in an increased hydrogen generation rate. However, the rapid bubble formation raises the overpotential owing to increased bubble resistance, resulting in a lower efficiency. Therefore, alkaline electrolyzers are typically operated be-

tween 1000 and 3000 A/m^2 to compromise between hydrogen generation rates and electrical efficiencies. Most conventional alkaline water electrolyzers operate around 80−90 °C. Increasing the temperature of electrolysis decreases the equilibrium voltage, hence reducing the electrical power input. However, operating at elevated temperatures also affects the structural integrity of the materials and heat management issues [27.47]. To sustain long-term service, operating temperatures above 150 °C have been abandoned.

Another key parameter is the working pressure of the electrolyzer. Alkaline electrolyzers can be operated either at atmospheric pressures or higher depending on the end use of the hydrogen. High pressures are generated by controlling the exit valve of the evolving product gases. Operating at elevated pressures reduces the size and volume fraction of gas bubbles, minimizing the overpotentials due to them. However, the increase in efficiency at higher pressures is not significant when compared to atmospheric cells [27.16]. Yet, alkaline pressure electrolyzers save substantially on gas compression costs in systems where gaseous storage is applied.

Proton Exchange Membrane Electrolysis

PEM electrolyzers offer a number of advantages over traditional alkaline electrolysis technologies, while still avoiding the formation of explosive hydrogen–oxygen gas mixtures. First, only pure water with no added electrolyte is used in the electrolyzer. Second, a shorter electron path through the electrolyte ($< 250\,\mu$m) results in reduced ohmic loss, allowing higher current

densities ($> 1000\,$mA/cm^2) and hence a more compact design [27.49, 50]. However, the high cost and compromised longevity of polymer membranes make the electrolyzers too expensive for general applications [27.51]. Further, the prerequisites to use noble metal catalysts and special current collectors, due to the acidic nature of the polymer electrolyte, are disadvantages compared to alkaline electrolyzers [27.52].

The general design of a PEM electrolyzer is analogous to that of a PEM fuel cell. The electrolyzer consists of an anode and a cathode separated by a membrane as shown in Fig. 27.8. The catalysts are deposited on either side of the membrane, forming the membrane electrode assembly (MEA). Purified water is fed to the anode structure of the cell. The membrane conducts hydrated protons from the anode to the cathode side. Individual cells are stacked into modules with bipolar plates providing the manifolds for water feed and gas evacuation. The bipolar plates include flow-field structures to enhance the transport of water to the electrodes, and product gases out of the cell.

Anode. In PEM electrolyzers, the oxygen evolution electrode, or anode, has a higher overpotential than the cathode [27.53]. Oxygen evolution occurs on noble metal catalysts such as Pt, Au, Ir, Rh, Ru, and Ag, but oxides of noble metals such as IrO$_2$ and RuO$_2$ have gained considerable interest over the last few decades. Several factors influence the electrocatalytic evolution of oxygen, namely the crystal-field stabilization energy, mixed and doped oxides, dispersion, crystallinity, and crystallite size [27.54]. Ruthenium oxide is known to be
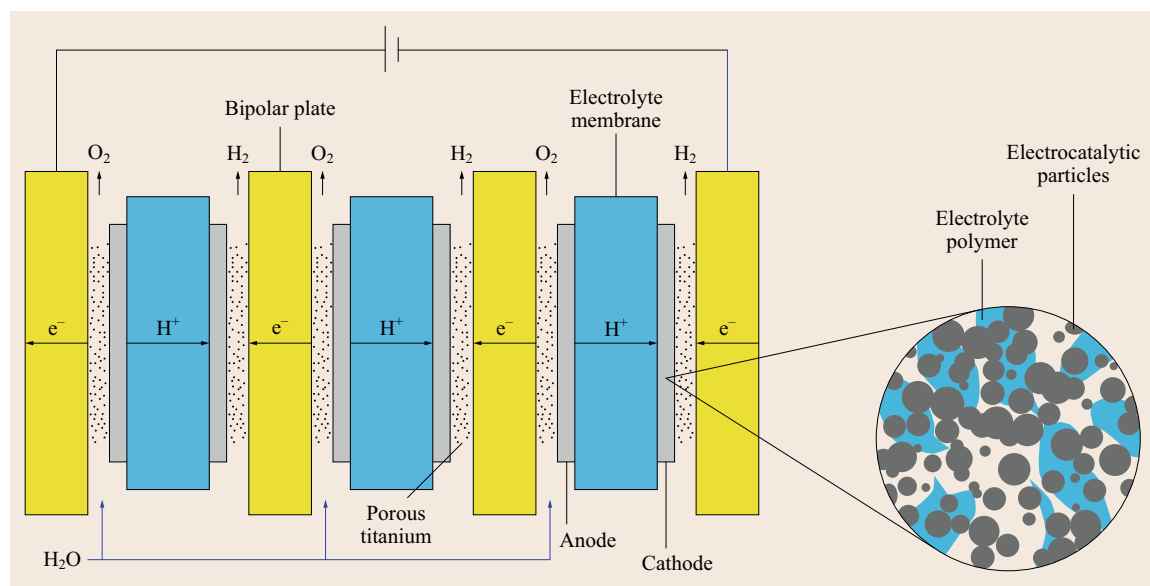

Fig. 27.8 Schematic of a PEM electrolysis cell (after [27.48], courtesy of ECS)

the most active oxide for the oxygen evolution reaction (OER) [27.55]; however, it suffers from instability and therefore needs to be stabilized with another oxide such as IrO_2. IrO_2 exhibits better corrosion resistance but is more expensive and has slightly lower electrocatalytic activity than RuO_2.

Addition of non-noble metal oxides has been reported to improve the stability of the IrO_2- and RuO_2-based electrodes in acidic media. Ir–Ta oxides have been suggested as the most efficient electrocatalysts for oxygen evolution in acidic electrolytes due to their high activity and stability [27.56]. Industrial anodes have been customarily based on a RuO_2 and TiO_2 mixture, where RuO_2 is the active component and TiO_2 the stabilizing agent. It has also been shown that SnO_2 improves the stability of IrO_2–RuO_2 anodes without reducing the activity significantly [27.57]. CeO_2 is also often added in order to enhance the selectivity for the desired reaction or to increase the anodic stability. Table 27.4 compares the performance (applied voltage) of PEM electrolyzers with different anode catalysts and loadings.

Among the parameters affecting the anodic overpotential are the catalytic activity and electrical conductivity of the electrocatalyst, which in turn relates to the composition and loading of the active component. The stability is related to the crystal growth and corrosion properties. Also, it is known that the development of efficient and less expensive electrodes (by reducing the loading of noble metal oxides or replacing them with cheaper alternatives) for the OER will make the electrolysis process more economical. The field is still open to new developments and improvements because many parameters must be optimized.

Cathode. Metallic platinum is typically used at the cathode for the promotion of the hydrogen evolution reaction (HER). The use of platinum is made necessary due to the highly acidic environment encountered in a solid polymer electrolyte, which promotes the corrosion of non-noble metal catalysts. Cost considerations require a significant reduction of noble metal loadings, at both the electrodes, from a few mg/cm^2 (current state of the art) down to around $0.1\,mg/cm^2$. Low Pt contents ($0.3-0.5\,mg/cm^2$) have been used at cathodes by depositing Pt nanoparticles onto high surface area carbons; for example, Vulcan XC 72 carbon black [27.58], carbon nanofibers [27.59], and carbon nanotubes.

Pd is almost as active as Pt for the HER and significantly less expensive. Using Pd–Pt mixtures, cell efficiencies close to 85% (1.7 V at $1000\,mA/cm^2$) have been demonstrated at the lab-scale with $0.7\,mg/cm^2$ metal loadings. Efforts are still required to further reduce Pt loadings down to $0.1\,mg/cm^2$ range. However,

the cost of the noble metal is not only due to the metal itself, but also due to the cost of the precursor salts used in the synthesis. The chemistry required to produce the most appropriate precursor may have a significant impact. Thus, the overall cost can be significantly different from one process to another, even with a similar final metal loading.

However, the ultimate goal is to eliminate the need for noble metals. Carbon-supported cobalt clathrochelate catalysts [27.60] have been developed for the HER. In these compounds, the metal ion is locked in a close-knit structure, inhibiting ligand exchange in the more labile oxidation states of the encapsulated metal ion. This, in turn, explains the low chemical activity of this family of stable complexes. A cell efficiency of 80% at a current density of $500\,mA/cm^2$ was obtained at 90 °C. Additional encouraging results have been obtained with polyoxometallates [27.61]. Commercially available tungstosilicic acid hydrate (α-$H_4SiW_{12}O_{40}$) adsorbed at the surface of the cathodic titanium current collector yielded an efficiency of 70% at a current density of $1000\,mA/cm^2$.

Membranes. Perfluorosulfonic acid (PFSA) membranes have found use in modern PEM electrolyzers and fuel cells [27.62]. These membranes have excellent proton conductivity, mechanical strength, and chemical stability. They serve three basic functions:

1. Conduct protons between the anode and the cathode
2. Provide electrical insulation
3. Provide a barrier that prevents the produced gases from mixing.

Implicit in this list is the additional requirement that the membranes have a suitably long lifetime for the desired application. This usually means that the polymers must have hydrolytic and oxidative stability and have good mechanical integrity. In addition to these basic requirements, modern PFSA membranes need to be humidified in order to achieve maximum performance (conductivity) and durability. This requirement has several drawbacks such as the additional expense of humidifiers and parasitic power losses from the operation. Hence, there is a need for membranes that depend less on water for conductivity, allowing hotter and drier operating conditions.

Up to now, proton-conducting perfluorinated sulfonic acid membranes, in the form of DuPont's Nafion or Dow Chemical's materials, have been used as the gas-separator and the electrolyte simultaneously. They contain sulfonic acid groups ($-SO_3H$) attached to perfluorinated carbon backbones, which upon contact with water produce polar hydrated sulfonic groups ($H^+SO_3^-$). They allow the mass and charge transfer in

Table 27.4 Summary of PEM water electrolyzer performance at an operating current density of 1000 mA/cm^2 and temperature of 80 °C using Nafion 115 membrane

Anode	Cathode	Noble metal loading (mg/cm^2)	ΔE_{app} (V)
Ir	40% Pd/C	3.36	1.697
Ir–Ru oxide (70 : 30)	20% Pt/C	2.4	1.623
Ir-oxide	10% Pt/C	2.4	1.645
Ir–Ta oxide	10% Pt/C	2.4	1.572
Ru oxide	Pt	8	1.675
Ir	Pt	3−6	1.620
Ir-oxide	Pt black	7	1.620
Pt–Ir	Pt	1	1.750
Ir oxide	Pt black	3	1.680

a PTFE insulator. The conductivity of the membranes increases with the acid content of the polymer, which is realized by lowering its equivalent weight (nonsulfonic group content). However, lowering the equivalent weight increases the solubility of the polymer in water making it mechanically unstable. Hence there is a compromise between performance and durability.

Recently, Ballard Power Systems developed low-cost nonperfluorinated polymer-based electrolytes. A series of sulfonated polyaromatic polymers were synthesized, and fabricated into membranes via solution casting. A comparison of the performance of the membranes in single solid polymer fuel cells showed that sulfonated polyaromatic membranes performed equally well or better than the standard Nafion membrane [27.63]. Some other nonperfluorinated membranes have been developed more widely for fuel cell applications. It is expected that the development of this new generation of low-cost solid polymer membranes will have a beneficial impact on industrial acid electrolyzers.

Bipolar Plates. Current collectors are porous structures located between the membrane–electrode assembly and bipolar plates to allow a uniform distribution of the electric current. Carbon-based materials such as carbon paper or felts can be used on the cathode side of PEM electrolyzers. However, carbon undergoes electrochemical oxidation on the anode side at voltages greater than 0.9 V [27.64]. Hence, porous structures made from titanium are used on the anode side. The main drawbacks of Ti are the formation of a resistive oxide layer at the surface and the high cost of the material. The performance of sintered Ti is superior to that of other structures, but it is also the most expensive choice followed by felt and expanded mesh.

A well-designed bipolar plate must have a high electrical conductivity, high gas permeability, and permit water flow to the electrode. In single electrolysis cells, the MEA and current collectors are sandwiched between two electrically conductive endplates. Several single cells are connected electrically in series and hydraulically in parallel as a stack. A bipolar plate separates two adjacent cells so that it acts as an anode of one and cathode of the adjacent cell simultaneously. As for current collectors, bipolar plates have to be constructed from corrosion-resistant materials, such as expensive titanium, stainless steel, or cheaper graphite composite materials. In order to reduce the contact resistance between a bipolar plate and the adjacent current collector, the plate is coated with precious metals such as gold or platinum [27.65].

System and Operating Conditions. The system configuration of a PEM electrolyzer is similar to that of an alkaline unit (Fig. 27.9). However, the system is simpler due to the absence of caustic as the liquid electrolyte. The power is supplied through a transformer and a rectifier to convert the AC voltage to the required DC voltage. The feed water pump supplies water to the circulation loop on the oxygen side of the electrolyzer. The water is pumped through a heat exchanger, ion-exchange resin, and gas–water separator. The circulation pump in the loop is used to cool the stack. On the hydrogen side, the product gas is separated by a gas–water separator, followed by a demister to remove droplets, heat exchanger and condensate trap to reduce the dew point to room temperature.

PEM electrolysis stacks offer very high power densities at similar voltage efficiencies compared to alkaline electrolysis stacks. At present, current densities from 500 to 2000 mA/cm^2 and cell voltages from 1.7 to 2.1 V are usual. In most cases, PEM electrolyzer stacks operate at temperatures between 50 and 90 °C, and at pressures in the range of 0.8−20 MPa [27.67]. In terms of operating hours and lifetime, considerable progress has been made over the years. Due to the endothermic reaction, higher efficiencies, and efficient cooling by the water recirculation, thermal management is facilitated compared with PEM fuel cells. However, mechanical
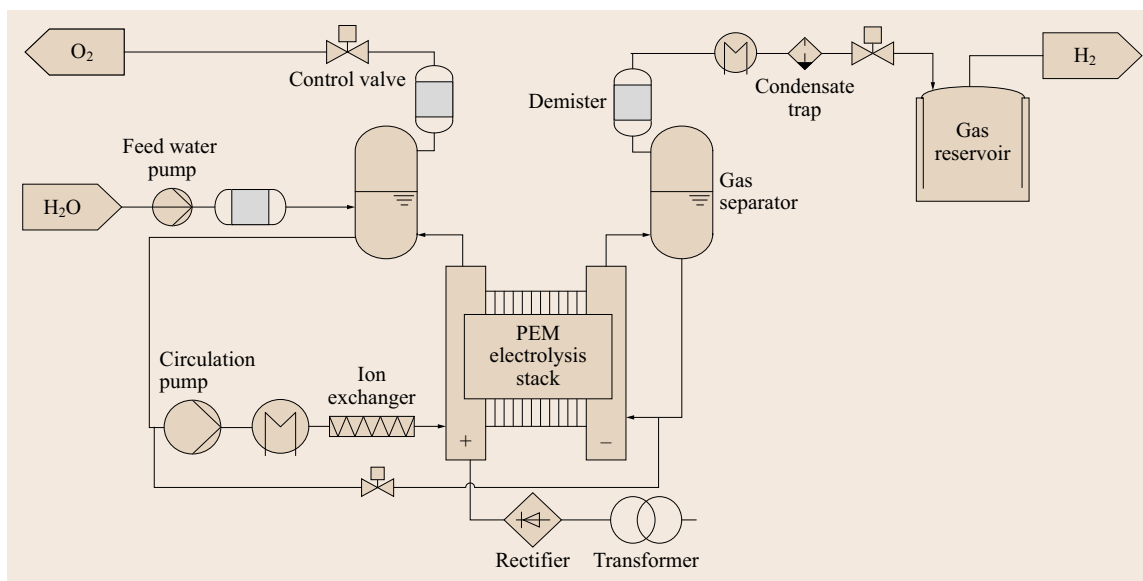
Fig. 27.9 Schematic of a PEM water electrolysis plant (after [27.66], courtesy of Wiley-VCH)

stress could be higher, as the stacks are operated under high pressures, with fluctuations caused during startup and shutdown. The most critical component of a PEM electrolyzer is the membrane, with thinning and ultimately failure leading to the mixing of gases. The lifetime of a well-designed and correctly operated PEM electrolyzer stack can reach up to several tens of thousands of hours. Water quality also has a strong effect on the degradation of the MEA, and typically deionized water with resistance values higher than $10\,M\Omega cm$ should be used.

27.2.2 High–Temperature Electrolysis

High-temperature electrolysis using SOEC is capable of operation at extremely high electrical efficiency, near 100%. Similar to SOFCs, high operating temperatures, typically $800-900\,°C$, are required due to the limited electrolyte conduction at low temperatures. As the resistance decreases (and ΔG decreases, Fig. 27.3) with increasing temperature, the current density will increase if the cell voltage is at the thermoneutral voltage. Since hydrogen production is stoichiometric with current density (which is limited by the cell resistance), it is apparent that optimum current density and cell resistance values are critical variables for the most efficient production of hydrogen.

Common Electrolytes and Electrodes
The most common electrolyte by far used in SOEC application is YSZ or yttria-stabilized zirconia. Most often, yttria is present in about $6-8\%$ concentration.

Such materials have very good oxygen ion conductivities, but these conductivities are only achieved at high temperatures ($> 750\,°C$). The maximum conductivity of YSZ is reported to occur at 7% loading, but significant differences (factor of 1.5) in conductivity measurements on samples with Y levels of $6-8\%$ are not due to dopant levels [27.68]. Yttria (and other dopants) is used to stabilize the cubic fluorite phase of zirconia as well as to increase the concentration of oxygen vacancies [27.69]. Scandium is also reported to be an effective dopant for scandia-stabilized zirconia (ScSZ) and the conductivity of ScSZ is comparable to, or slightly higher than, YSZ at temperatures of interest for fuel cell or electrolysis cell applications.

Doped ceria also has a fluorite structure and is a common electrolyte in fuel cells. It has a higher *conductivity* than zirconia, especially at lower temperatures, but possesses electronic conductivity at low oxygen partial pressures [27.70]. Ceria is often doped with gadolinium (GDC) or samarium (SDC) to generate oxygen vacancies, which increases ionic conductivity [27.71–73]. Similar to the YSZ–ScSZ system, the conductivity is maximized with dopant ions that have the lowest size mismatch. Conductivity increases with Gd content, reaching a reported maximum at $\approx 10\,mol\%$ Gd, and then decreases [27.74]. *Fergus* [27.69] summarizes comparative conductivity data for YSZ, ScSZ, and GDC samples. The GDC samples consistently show higher conductivity than the zirconia species below $600\,°C$, and the level of Gd has a sensitive effect on stability toward low oxygen partial pressures.

A notably different approach is the use of strontium-doped zirconate and cerate as proton conductors for SOEC [27.75]. These materials, which are perovskite-type oxides, exhibit proton conduction at intermediate temperatures ($\approx 400\,^\circ$C). However, the cell design is such that protons, produced at the anode, are *pumped* through the electrolyte to the cathode, where they are reduced to form H_2. This eliminates the need to separate H_2 from steam, which simplifies the process, and lowers the overall costs for stacks and system. In addition, the intermediate temperature will potentially allow a greater selection of materials for flow channels, interconnects, etc. (i. e., balance of plant materials). The ceria derivatives are reportedly hydrothermally unstable, reacting with water vapor to form $Sr(OH)_2$ and CeO_2.

Electrodes. By far, the most common cathodic (produce hydrogen) materials are nickel cermets (ceramic–metallic blends). Most commonly, this is nickel mixed with zirconia [27.76] or YSZ [27.26, 77, 78]. It has been reported that Ni–YSZ electrodes have lower activity in electrolysis mode versus fuel-cell mode, and a diffusion-limited process was proposed to account for this behavior [27.79]. In addition, the aging of Ni–YSZ electrodes in a steam-rich environment has been reported, and ascribed primarily to coarsening of Ni particles [27.80]. This effect can be overcome to a large extent by ensuring that a reducing atmosphere over the electrode is maintained. Maintaining some hydrogen partial pressure with the steam feed can accomplish this. *Kim-Lohsoontorn* and coworkers have reported the performance of gadolinium doped ceria (GDC)-impregnated Ni–YSZ cathodes [27.81]. Addition of GDC to Ni–YSZ-enhanced performance, and the addition of 0.5 wt% Rh to the GDC led to significant improvement in the performance of both electrolysis and fuel-cell mode as compared to Ni–YSZ and Ni–GDC electrodes. The latter showed decreasing performance as the steam–H_2 ratio increased from 50/50 to 90/10, but the GDC-Ni YSZ analogue was relatively insensitive to these changes.

Anodic materials for O_2 generation (27.6) are commonly composites of YSZ and perovskites such as lanthanum manganite ($LaMnO_3$), ferrite ($LaFeO_3$), and cobaltite ($LaCoO_3$) which have been partially substituted with strontium [27.82]. Very commonly the strontium-substituted lanthanum manganite is used, termed LSM. However, there is a very wide range of oxide materials used, usually in combination (i. e., LSM with LSCF (lanthanum strontium cobalt ferrite). The composites are referred to as YSZ–LSM, YSZ–LSCM, YSZ–LSF, etc.

The use of LSM and LSM-derived anodes for SOEC is common, due to cost (relative to noble metals), ease of anode preparation, and thermal expansion characteristics [27.71, 76, 77]. It has been reported that LSF–YSZ composite exhibited higher catalytic activity for the oxidation on O^{2-} to O_2 [27.76]. LSM can be sintered together with YSZ at relatively high temperatures without forming insulating layers comprised of zirconates [27.83]. However, it is known that anodes based on LSCo and LSF exhibit much lower polarization losses than LSM, but LSCo–YSZ electrodes are reported to deactivate slowly due to solid-state reactions [27.77].

Marina et al. have reported a study on electrode performance in fuel cell and electrolysis modes; in both half- and full-cell mode [27.84]. The authors report that Ni-YSZ has higher losses than a La-substituted strontium titanate–ceria composite in electrolysis mode, but similar performance in fuel-cell mode. The titanate–ceria electrode performance was diminished at high steam partial pressure. Anode materials also showed higher losses in electrolysis mode, particularly for mixed conductor electrodes made from LSCuF and LSCoF. With fuel cells using a thin electrolyte, polarization losses were higher in electrolysis mode. The anodic polarization arising from O_2 evolution operation is expected to decrease oxygen vacancy concentrations, which would then give rise to higher polarization losses [27.84]. *Singh* and coworkers have reported a study on the effect of O_2 partial pressure on the stability of LSM–YSZ composite [27.85]. They report that the unit cell volume for LSM increases during exposure to lower O_2 partial pressures (1×10^{-7} MPa), but YSZ unit cell volume is unchanged. Lower O_2 partial pressure also results in grain growth and formation of $La_2Zr_2O_7$ and MnO_x compounds, which lower the stability, but the reaction was shown to be reversible upon sintering at O_2 partial pressure of 0.021 MPa.

Cells and Stacks

Leung's team has published a relatively recent review on SOEC technology development [27.77]. Electrolytes, electrodes, and cell–stack designs are covered. Although the earlier work by *Doenitz* [27.19] and *Isenberg* [27.20] utilized tubular cells, planar cells have received much more attention recently, due to better manufacturability and also more uniform distribution of gas species on the planar cells [27.71]. The latter characteristic improved the performance relative to tubular cells.

Mogensen and coworkers at the Riso National Laboratory in Denmark have published a number of papers over the last several years describing the develop-

ment of planar SOEC cells [27.78, 86, 87]. Ceramatec, Inc. and collaborators have also published a number of papers on stack production and testing [27.76, 88–90]. The work by Mogensen and coworkers describe planar, Ni–YSZ-supported cells (5×5 cm) with active electrode areas of $16 \, \text{cm}^2$, which are produced at the Riso National Lab for Sustainable Energy at the Technical University of Denmark. Typically, the cells have a $300 \, \mu\text{m}$ thick NiO–YSZ porous support layer prepared by tape casting, a $10-15 \, \mu\text{m}$ thick YSZ electrolyte, spray painted onto the support tape. After these half cells are stamped and sintered, a $10-15 \, \mu\text{m}$ thick LSM–YSZ (50 : 50) composite oxygen electrode (anode) is spray painted onto the cells followed by re-sintering. The cell construction consists of aluminum housing, Ni foil current collector, gas sealing, and a gas distributor based on Ni-YSZ. The air distributor is based on LSM, and another current collector (gold foil) and remaining alumina housing are placed on top to prove a cross flow for the gases. Ceramatec also uses a planar cell design. The cells are electrolyte-supported, using ScSZ electrolytes ($\approx 140 \, \mu\text{m}$ thick), Ni-cermet cathodes, and manganite-based anodes [27.70]. The cells are slightly larger (10×10 cm) than those reported by Mogensen, with an active area of $64 \, \text{cm}^2$ per cell. Interconnects are made from ferritic stainless steel. Stacks are assembled from single cells, and for laboratory testing commonly contain 10 or 25 individual cells [27.88, 89]. The Idaho National Laboratory (INL) in the United States established a significant program on HTE coupled with nuclear energy. Ceramatec was a partner in this effort. As part of the scale up and demonstration activities, INL commissioned a 15 kW HTE test facility, termed the integrated laboratory scale (ILS) HTE test facility [27.91]. The ILS includes three electrolysis modules, each consisting of four stacks with 60 cells, yielding 240 cells per module and 720 cells total. The cells are planar cells based on Ceramatec's technology. Each module has an independent support system, which supplies electrical power, feedstock (steam with some H_2), sweep gas for removal of produced O_2, and exhaust gas handling. Other equipment includes dewpoint measurement for inlet and outlet feeds, steam generators, condensers for residual steam, and H_2 vent. All three modules were housed in a single hot zone.

Bo and coworkers at the Institute of Nuclear and New Technology (INET), Tsinghua University, Beijing, have also reported on their efforts for HTE process development [27.92]. Again, a major thrust of the work was the utilization of nuclear-based heat. This group also uses planar cells and designs, using Ni–YSZ cathodes, YSZ electrolyte, and both LSM and BSCF ($Ba_{0.5}Sr_{0.5}Co_{0.8}Fe_{0.2}O_{3-\delta}$) anodes. The BSCF gave improved performance (lower cell resistance, higher H_2 production) compared to LSM.

Kim and coworkers at the Korea Institute of Energy Research recently reported a three-cell flat-tubular solid oxide electrolysis stack [27.93, 94]. The NiO-YSZ cathode supports were extruded in the shape of flat tubes by a well-defined process. After heat treating the tubes for 3 h at $1150 \,^\circ\text{C}$, gas channels were formed by machining one side. The other side was used for a ceramic interconnector. After dip coating into a YSZ slurry, the ceramic interconnector was applied via spray coating of perovskite-type ceramic powders. Tubes were then calcined at $1400 \,^\circ\text{C}$ for 3 h. Lastly, the anode catalyst was spray-coated onto the gas channel using a LSM slurry, followed by heat treatment again at $1150 \,^\circ\text{C}$ for 3 h. A Ba–Si-based glass ceramic sealant was used for gas seals and stack manufacturing. The seals were cured via a two-step process, first at $900 \,^\circ\text{C}$ for 1 h (spreading and adhesion), then $800 \,^\circ\text{C}$ for 3 h for complete fixation and sealing.

Other workers have also recently reported studies on microtubular electrolysis cells. *Lagunna-Bercero* et al. [27.95] fabricated a cathode-supported Ni-YSZ/YSZ/LSM cell, with a $20 \, \mu\text{m}$ electrolyte thickness. The Ni–YSZ tube was 2.4 mm diameter and $10-15$ cm in length, fabricated by cold isostatic pressing at 200 MPa. The gas-tight electrolyte was applied by wet powder spraying, then fired at $1400 \,^\circ\text{C}$. After firing, the LSM anode (LSM and 50/50 LSM–YSZ) was applied via dip coating, then re-sintered at $1250 \,^\circ\text{C}$. Researchers from the Energy Research Center of The Netherlands recently reported their progress on planar SOEC technology [27.96]. These cells used Sc–Ce-doped zirconia (ScCeZ) as electrolytes made by conventional tape casting. The anode was a $5 \, \mu\text{m}$ thick layer of YDC ($Y_{0.2}Ce_{0.8}O_{2-\delta}$), applied via screen printing. After firing at $1400 \,^\circ\text{C}$ for 1 h, the cathode layer was applied. This cathode had three layers, $5 \, \mu\text{m}$ thick layer of GDC, then a $\approx 15 \, \mu\text{m}$ thick NiO–GDC (65/35) layer was applied, followed by a $20 \, \mu\text{m}$ thick NiO layer. After firing the cathode at $1250 \,^\circ\text{C}$ for 1 h, a final layer of LSCF was applied to the anode and the assembly given a final heat treatment at $1100 \,^\circ\text{C}$ for an hour.

Kerafol GmbH has also reported its efforts with ScYZ electrolytes [27.97] These newer electrolyte-supported cells, developed with HC Stark, utilize a YSZ–LSM cathode and GDC–NiO anode. The electrolyte thickness is $\approx 150 \, \mu\text{m}$. Optimum cathode sintering temperature was determined to be $1100 \,^\circ\text{C}$. Kerafol also describes its efforts in developing ceramic glass sealing tapes and processes to improve reliability and lower costs.
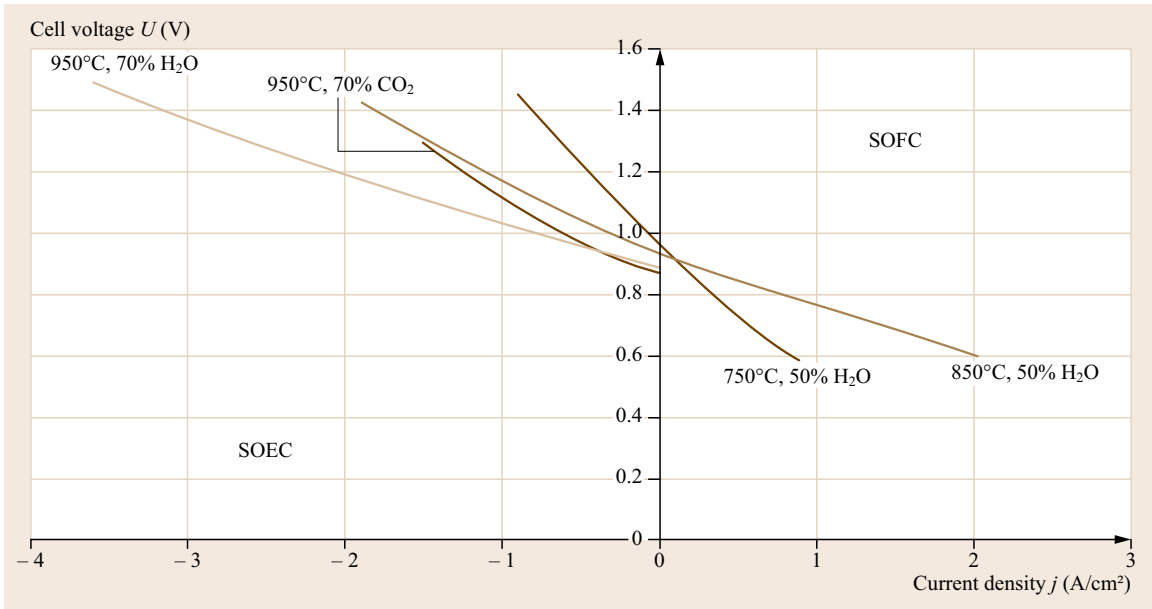
Fig. 27.10 Current–voltage curve from a planar cell (after [27.86])

Cell and Stack Performance. Current density versus cell voltage (I/V) curves are most often used to demonstrate performance characteristics of cells and stacks. Figure 27.10 shows cell voltage versus current density from a planar cell produced at Riso Laboratory described above. The positive current density is fuel-cell mode, and negative current density is electrolysis mode. (Current densities in this section will be reported without the negative sign, but it should be understood where these lay with respect to fuel-cell mode.) Note that the various curves (corresponding to different temperatures and gas partial pressures) have a similar *y*-intercept at zero current density. This is the opens-circuit voltage (OCV) and is often around 0.9 to 1.0 V for SOEC-type devices (the exact OCV can be calculated with the Nernst equation for a given gas composition and temperature). Note that very high current density ($\approx 3600 \, \text{mA/cm}^2$) is achieved at 950 °C with 70% steam/30% H_2 feed (and steam utilization of 37%). Typically, some fraction of the feed stream is H_2 to keep the Ni cathode from oxidizing and coarsening. *Jensen* et al. believed that this was the highest current density reported at that time (2007) for SOEC operation [27.86]. It is certainly much more common to find current densities in the 200–600 mA/cm^2 range especially for longer term testing. However, the microtubular cell reported by *Lagunna-Bercero* et al. is claimed to withstand 6000 mA/cm^2 current density at 895 °C without apparent cell damage [27.95].

A similar *I–U* curve has been published by *Schiller* et al. and is shown in Fig. 27.11 [27.21]. Here, both voltage (U) and power density (p) are plotted against current density. In this case, a single cell was operated in both electrolysis and fuel-cell modes at temperatures between 750 °C and 850 °C. The negative current density indicates electrolysis mode. A 70/30 steam–hydrogen feed was used in these tests. Note here that the OCV again is near 0.95 V. The effect of temperature is readily apparent: At 750 °C, a voltage of 1.2 V gives a current density of $\approx 375 \, \text{mA/cm}^2$, whereas at 850 °C, the same voltage results in a current density of 800 mA/cm^2.

Another representation is shown in Fig. 27.12. This graph (with calculated values) shows heat flux versus voltage and current density for a planar-type stack. It illustrates that the heat generation in the stack can be negative, zero, or positive, depending on the voltage. Again, the open-circuit voltage (or open cell potential) is about 0.86 V. The calculation assumed an operating temperature of 927 °C, H_2 mole fractions of 0.1 and 0.95 at the inlet and outlet, respectively, and a R_{ASR} (area-specific resistance) of 1.25 Ωcm^2. The ohmic heat flux is given by

$$q_\Omega = j^2 R_{\text{ASR}} = j(V_{\text{op}} - V_{\text{N}}) \tag{27.24}$$

where j is the current density, V_{N} is the mean Nernst potential for the cell, and R_{ASR} is the area-specific resistance. The reaction heat flux is given by

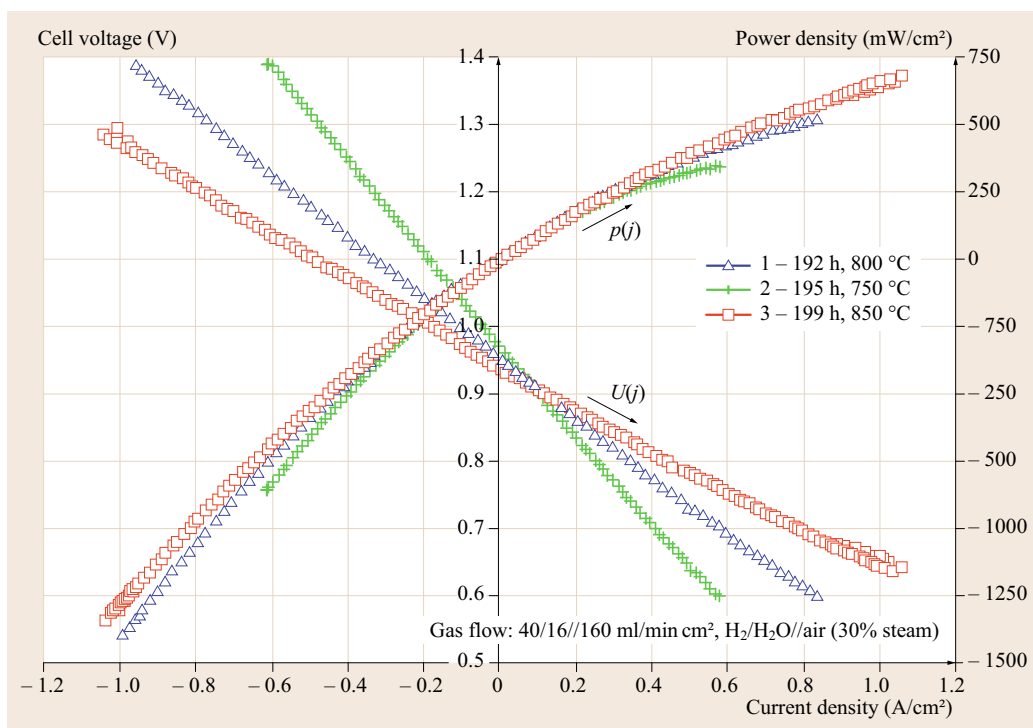$$q_{\text{rxn}} = \frac{j}{2F}(T \Delta S_{\text{e}}) , \tag{27.25}$$

Fig. 27.11 I/U and j/p characteristics of a metal-supported cell (after [27.21])

where ΔS_e is the entropy change for the electrolysis process, accounting for the reactant and product partial pressures.

In fuel-cell mode, the net heat flux is always positive, and increases with operating voltage and current density [27.91]. In electrolysis mode, the net heat flux is negative at low current densities, increases to zero, then is positive at the higher current densities. The point at which the net heat flux is *zero* is the thermoneutral voltage (Sect. 27.1.4 and (27.23)) [27.91].

The thermoneutral voltage increases only slightly in magnitude over the typical operating temperature range for SOEC devices (1.287 V at 800 °C to 1.292 V at 1000 °C) [27.91]. At typical SOEC temperatures and R_{ASR} values, operation at the thermoneutral voltage will give rise to current densities in the $200-600\,\text{mA/cm}^2$ range [27.91]. The very high current density reported by Mogensen et al. may result from very low internal resistance associated with their cell ($0.17\,\Omega\text{cm}^2$). For example, the Riso cell achieved the $-3600\,\text{mA/cm}^2$ current density at 1.48 V. With an OCV of 0.88, the internal resistance is

$$\frac{1.48-0.88\,\text{V}}{3.6\,\text{A/cm}^2} = 0.17\,\Omega\,\text{cm}^2\,.$$

If the resistance were in the range of 1.0 to 1.5, the current density would be $400-600\,\text{mA/cm}^2$.

In order to produce large volumes of hydrogen, individual cells must be assembled into stacks. Figure 27.13 shows a schematic of a stack assembly.

Commonly, a lab scale stack will contain 10 identical electrolyte-supported cells (less frequently there are 25). A *cell* is defined as one anode–electrolyte–cathode assembly. The individual cells have been described in Sect. 27.2.2 and are also discussed in [27.76].

The stack is assembled by layering the cells with metallic interconnect assemblies. The interconnects comprise a metallic separator plate sandwiched between two metallic flow-field layers (Fig. 27.13). These conductive metal layers provide electrical contact between the anode and cathode of adjacent cells, connecting the cells in series. Interconnects can be fabricated from low-Cr ferritic stainless steel. It includes an impermeable separator plate approximately 0.46 mm thick, with edge rails and two corrugated/perforated flow fields. The flow-field layers provide channels for gas flow to the anode and cathode with which they were in contact (the cells were arranged in parallel with respect to gas flow). The steam–H_2 flow field is fabricated from Ni foil; same for the air side is ferritic stainless steel. To improve performance, the air-side separator plates have the surface pretreated to form a rare-earth conductive oxide scale. A perovskite rare-earth coating is also applied to the separator-plate oxide scale by screen printing or plasma spraying; a thin ($\approx 10\,\mu\text{m}$) nickel
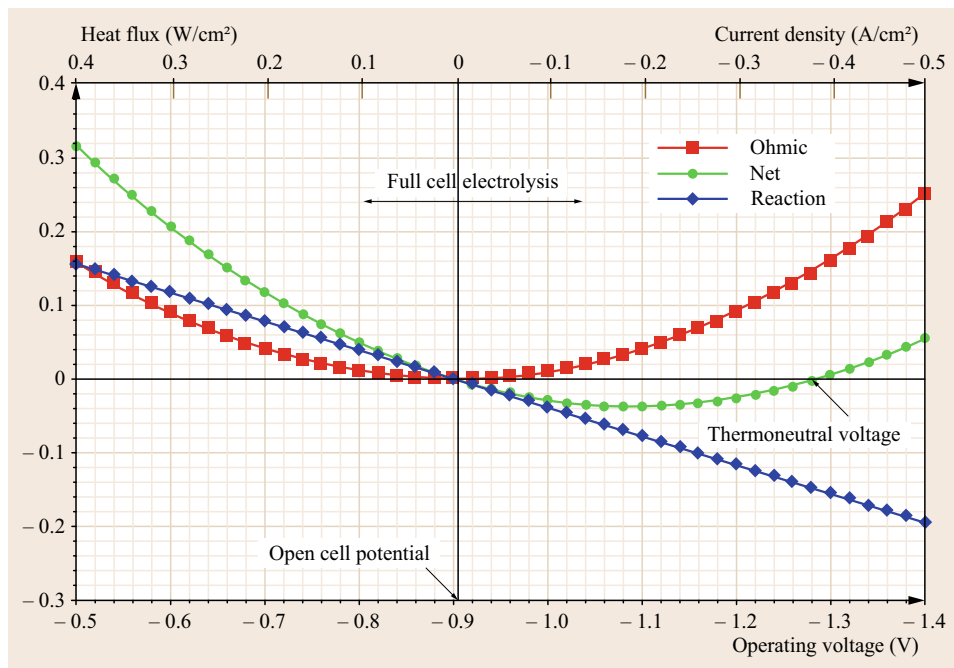
Fig. 27.12 Thermal contributions in electrolysis and fuel cell operations (after [27.91], courtesy of INL)

metal coating is applied to the steam–H_2 side of the separator plate.

Gas inlet and outlet manifolds were added to the sides of the stack assemblies. Two sets of manifolds were used, one to provide steam–H_2 to the stack cathodes and one to provide sweep gas (air) to the stack anodes. The sweep gas is not a reactant; rather, it is used to ensure a constant oxygen partial pressure at the stack anodes. Stack operating voltages are measured by spot-welding wires onto power lead attachment tabs that were integral to the upper and lower interconnect separator plates. Since the stack air outlet plane is open, the small air-flow channels are accessible for small leads to provide intermediate cell voltages. Additionally, four miniature thermocouples were inserted into the air-flow channels to monitor internal stack temperature. The entire stack assembly is then placed into a stack holder inside a large furnace or kiln.

The process test system included automated dew point sensors on the steam–hydrogen inlet and process outlet streams. Typical flow rates in the system were 2000 sccm (standard cubic centimeters per min) N_2, 400 sccm H_2, and 4000 sccm water (corresponds to an inlet dew point temperature of 83 °C). Air flow rate was 3500 sccm. Figure 27.14 provides data from such a stack test. In each of the tests shown in Fig. 27.14, the furnace temperature and gas flows were held constant, and the power supply programmed to vary the applied stack voltage between 8 and 14 V. The sweep rate was ≈ 8 mV/s; thus each sweep in the figure was

approximately 25 min in duration. The curves labeled *FLUENT* were calculated with the FLUENT modeling package. The OCV values were calculated values. The simulation empirically adjusted gap contact resistances to yield overall R_{ASR} values that matched experiment. The area-specific contact resistance values for sweep 4 were reported to be 0.74 Ωcm^2 between the electrodes and flow channels, and 0.18 Ωcm^2 between flow channels and the separator plate.

Sweep 1 was performed with low inlet steam content, and had a large ASR value as inferred from I–V curves. This behavior is an example of a mass-transfer-limited overpotential. Sweep 2 was an intermediate steam content test, and is nearly linear over the range of current densities tested. Sweeps 3 and 4 (inlet dew point of ≈ 83 °C) show linear behavior at lower current densities, then become concave-down at the higher values. Herring et al. suggested that the lower slope in these sweeps is related to the mean electrolyte temperature as the operating voltage increases (as the ionic conductivity of the electrolyte increases with temperature). Sweep 5 has a shallower slope than the others, reflective of the higher furnace temperature.

The internal temperatures measured in the stack at four different locations showed lower temperatures than the stack inlet temperature. At voltages between OCV and thermoneutral, the endothermic reaction heat requirement is less than the ohmic heating and a net stack cooling occurs. The thermal minimum was reached at 11.2 V and full thermal recovery (internal stack temper-
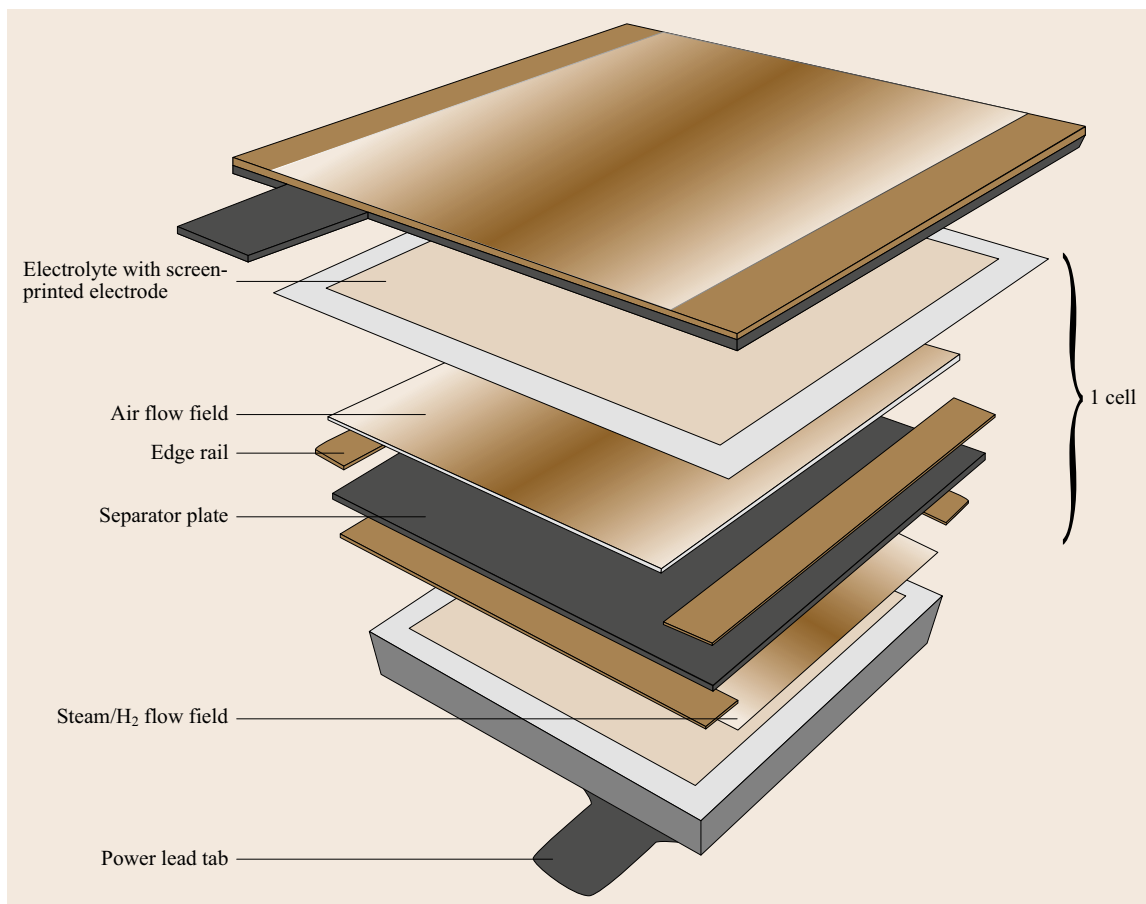
Fig. 27.13 SOEC stack diagram (courtesy of INL and Ceramatec)

atures near the inlet temperature) was realized near the thermoneutral voltage of 12.9 V.

Hydrogen production rates can be calculated from the stack current according to

$$H_2 \text{ molar flow rate} = \frac{I}{2F}(\text{no. of cells}),\qquad (27.26)$$

where I is current (A) and F is the Faraday number. The product of the electrical current and number of cells is the total ionic current. In addition, the hydrogen production rate can be calculated independently from the inlet and outlet dewpoint temperatures. The production rates from sweep 2 in Fig. 27.14 are shown in Fig. 27.15.

Note that both methods are in good agreement, although there is a bit more noise in the values based on dewpoint. The production rate of H_2 is linear since it is directly proportional to stack current. The authors indicate that up to 0.09 Nm^3/h H_2 production was achieved with this stack.

Researchers at the Korea Institute of Energy Research have published results from a three cell flat-

tubular solid oxide stack. The details of the cell assembly were described above. Figure 27.16 shows the gas flows, stack voltage, current, and H_2 production rate from an 80 h test at 750 °C. The stack was operated at 3.9 V (1.3 V per cell), and stack current was monitored. The average current flow was 3.23 A, and the equivalent H_2 production rate was 0.004 Nm^3/h. The authors report a total of 0.144 Nm^3 of H_2 produced over 37.1 h of operation. At an average 0.004 Nm^3/h, and the 30 cm^2 cell area, a production rate of 2.95 kg H_2/d per square meter cell area can be calculated.

Lifetime and Degradation Testing. Operation at higher current density offers the possibility of producing a given volume of H_2 with less cell/stack area. In turn, the expected overall stack investment will be lower. These savings may be offset by more rapid degradation at the higher current density. Invariably, SOE cells and stacks will degrade with time. If this degradation rate can be managed to an acceptably slow rate (i. e., < 1%/1000 h), a sufficient lifetime can be an-
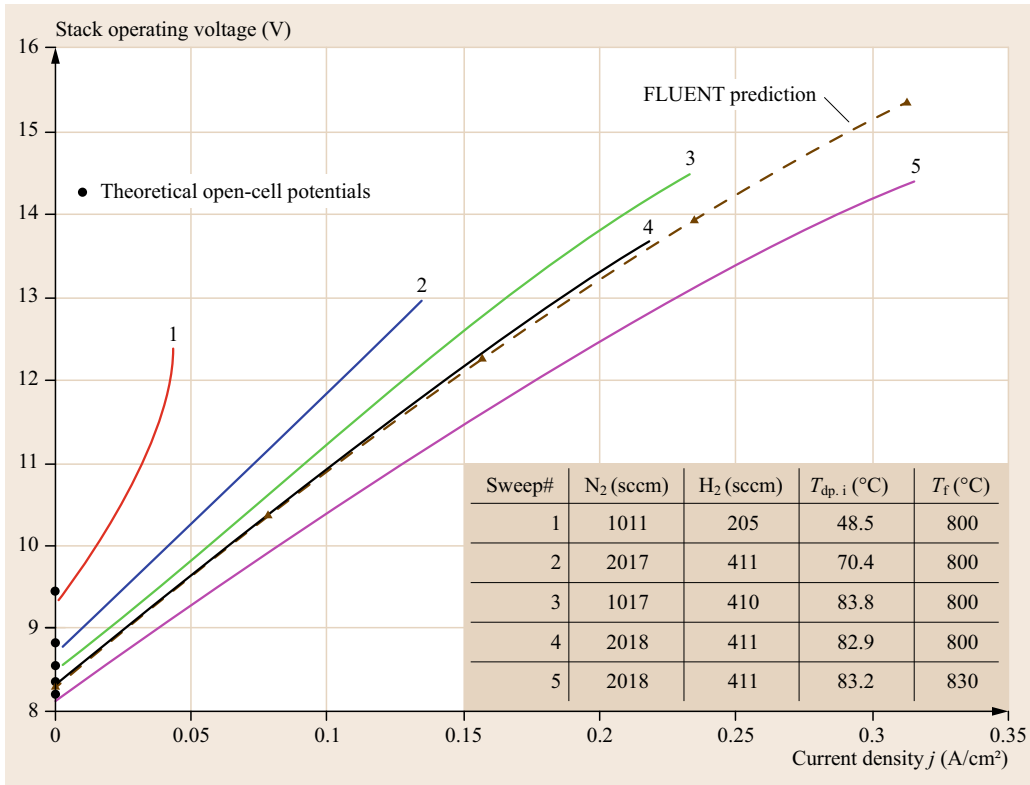
Fig. 27.14 Stack operating potential as a function of current density (after [27.76])

Sweep#	N_2 (sccm)	H_2 (sccm)	$T_{dp.\,i}$ (°C)	T_f (°C)
1	1011	205	48.5	800
2	2017	411	70.4	800
3	1017	410	83.8	800
4	2018	411	82.9	800
5	2018	411	83.2	830
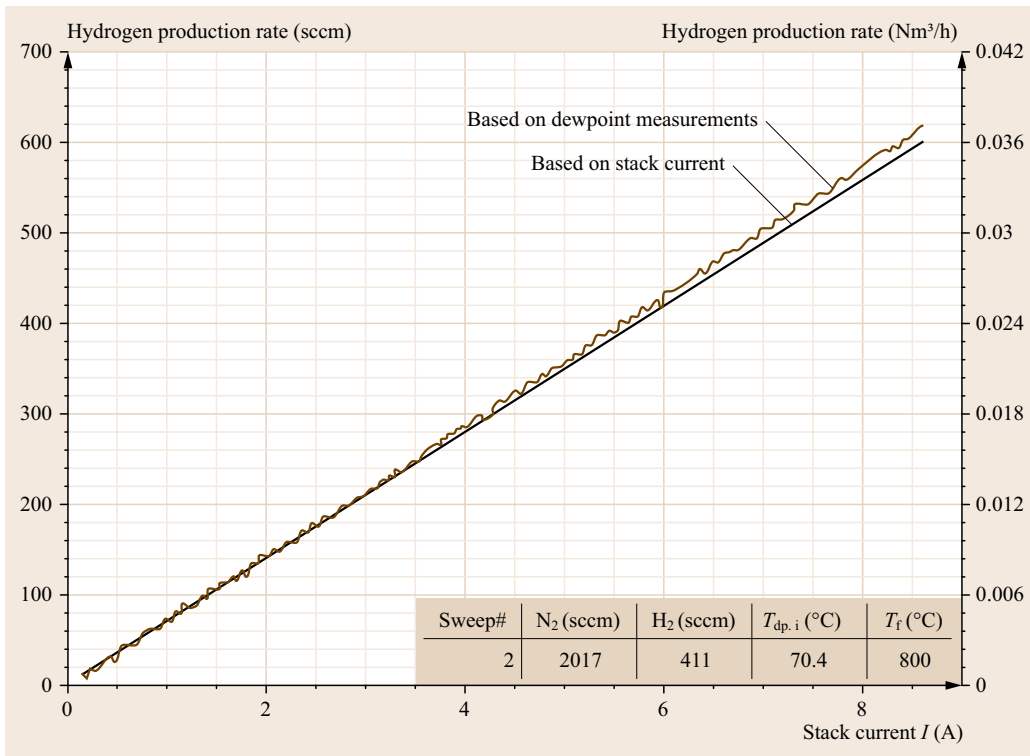
Fig. 27.15 H_2 production rates during DC potential sweep (after [27.76])

Sweep#	N_2 (sccm)	H_2 (sccm)	$T_{dp.\,i}$ (°C)	T_f (°C)
2	2017	411	70.4	800

Part E | 27.2

Fig. 27.16 Performance of a three-cell flat-tubular solid oxide electrolysis stack at 750 °C (after [27.93])
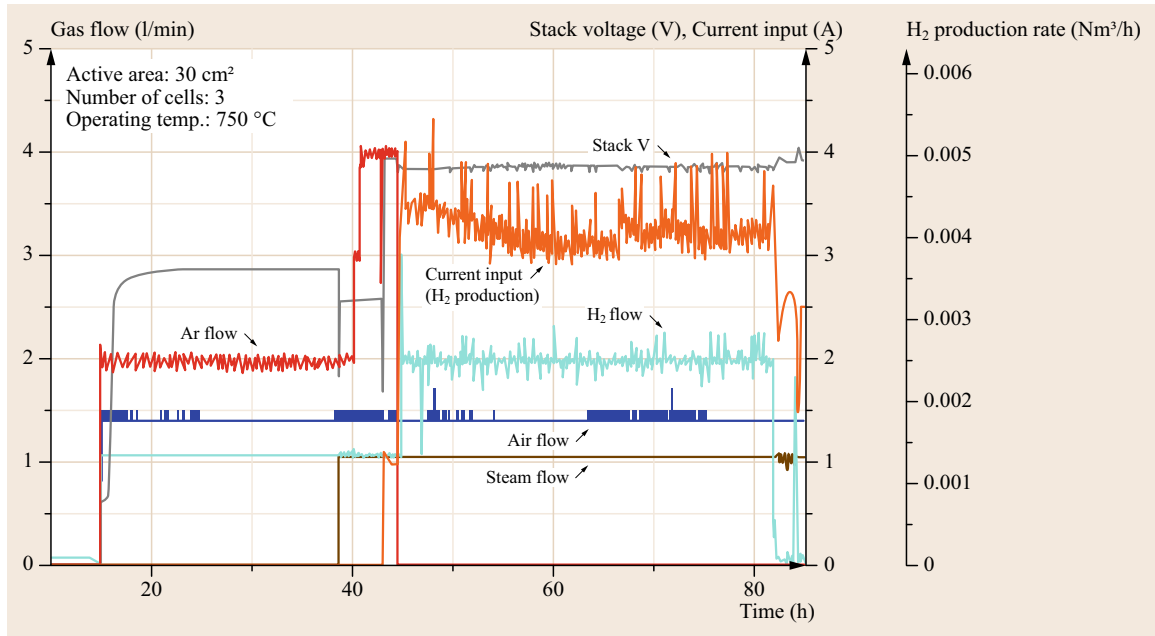
ticipated. Commonly, targets of 4.5−5 years stack life are targeted in the literature as *acceptable*, based in part on the relative insensitivity of H_2 production price to the lifetime longer than 3−4 years [27.98]. Operational integrity and reliability (up-time) are always essential characteristics.

However, while many researchers have reported good initial performance over short periods of time, demonstrating the maintenance of such performance over thousands of hours is much more challenging. There are multiple pathways for SOEC degradation, both *chemical* (impurities, Cr, Mn poisoning, etc.) and *mechanical* (bonding, sealing, electrode adhesion, metallurgy, etc.). In addition, long-term testing is not always possible due to resource and time constraints. There is much less information available regarding long-term (thousand's of hours) operation of SOEC cells and stacks than the short-term testing and performance characterization data. Nevertheless, a few groups have reported such studies.

Schiller et al. [27.21] reported the performance characteristics of the metal-supported cell described above. Over 2000 h, at 300 mA/cm², the voltage loss was 3.2%/1000 h. The Riso National Lab results show a similar result, but initial periods (≈ 100 h) have voltage increases, then begins to decrease. They reported tests of > 700 h.

One of the longest term test periods has been reported by *Schefold* et al. in Germany [27.99]. This 9300 h test (387 d) was performed on an anode-supported SOEC (45 cm² area) at 780 °C and 1000 mA/cm² current density. The cell consisted of a YSZ electrolyte, Ni–YSZ cathode, and LSCF anode.

This report also provides an excellent summary of the degradation studies to date for both cells and stacks. At current densities between 300 and less than 500 mA/cm² in SOEC mode, the lowest rates for voltage losses were in the range of 2−3%/1000 h. These authors also document studies where degradation rates of up to 10%/1000 h were noted. When the current density was increased to ≈ 1000 mA/cm², drastic acceleration in degradation was documented, owing to an increasing resistance of YSZ electrolyte as well as increases in ohmic resistances.

Such long-term tests are not without process upsets. Such upsets are commonly encountered in most labs, pilot plants, and operating facilities. Mechanical shocks, unstable steam supply, impacts from evaporator purging, blocked evaporator, and loss of gas flow are all documented [27.93]. Nevertheless, the test duration represents about double the longest stack test and about an order of magnitude longer than cell tests. In addition, the high current density is significantly above most long term test studies. Remarkably, the voltage loss over the entire test was 3.8%/1000 h, corresponding to 40 mV. During the initial 5600 h, the loss was lower (2.5%/1000 h) and, during an incident-free period, it was even lower at 1.7%/1000 h.

These authors also correctly point out that SOEC degradation data are not based on standardized test-
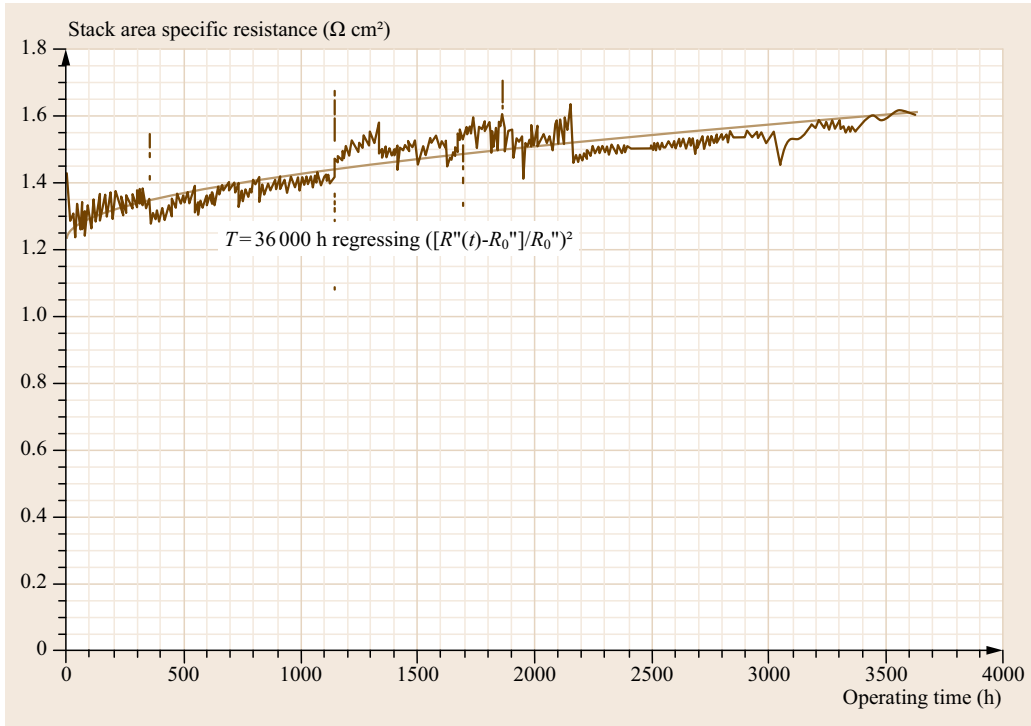
Fig. 27.17 Regression fit in stack with low degradation (after [27.100], courtesy of Ceramatec)

ing conditions. Steam content, current density, steam utilization, constant current versus constant voltage operation, etc., are all different in many of these studies. Degradation could be defined as an increase in voltage (if operating at constant current), a decrease in current (if operating at constant voltage, as in this experiment), or an increase in resistance. These quantities are all related as shown in (27.27)

$$R_{ASR} = \frac{U - U_0}{nj} \, , \tag{27.27}$$

where R_{ASR} is the average ASR, U is the stack voltage, U_0 is the stack open-circuit voltage, j is the current density, and n is the number of cells. If U, U_0, and n are held constant, the ASR is simply proportional to the reciprocal of current density (j). Essentially, lower current density at a given operating voltage means a higher resistance.

One challenge in using the 1000 h percent degradation metric is that it is sometimes difficult and somewhat arbitrary to choose an appropriate baseline or initial value, particularly in a specific case where there is a relatively high level of noise in the data. Ceramatec [27.100] has reported that long-term degradation follows a square root dependence with time, as shown

in

$$R_{ASR} = R_0 \left(1 + \sqrt{\frac{t}{\tau}} \right) \, , \tag{27.28}$$

where R_0 is the initial resistance, t is time, and τ is a time constant, which is defined as the time required to double the initial ASR. This represents another way to quantify the long-term performance of a cell or stack of cells. An example of Ceramatec's approach is given in Fig. 27.17. The resulting τ value is 36 500 h, or just over 4 years, for this stack to double the resistance.

Degradation Mechanisms. At present, a complete understanding of, and complete agreement upon the causes of degradation and the electrochemical mechanisms behind them does not exist. However, this has been the focus of much work in the SOEC community, and certain degradation routes are well-characterized. *O'Brien* et al. [27.89] have suggested three main categories for degradation:

1. Progressive, constant rate degradation
2. Degradation corresponding to transients caused by thermal or redox cycling phenomena
3. Degradation resulting from a sudden failure or malfunction of a component.

Degradation data is available for both individual cells as well as stacks. Degradation routes in stacks are not the same as those for individual cells [27.101]. Stack degradation is faster than cell degradation. Degradation in SOECs is more rapid than the same cell run in SOFC mode, as much as five times faster. Thus, the body of work that exists for SOFC technology can be used as a starting point and reference, but the development of SOEC technology will require study of SOEC components and stacks. In early work, *Jensen* and *Mogensen* reported cells that showed lifetimes of a hundred hours or so [27.102]. A second-generation design showed limited degradation over a 1 year test. The authors reported that the degradation in SOFC mode was far less than in SOEC mode for the same system. More recently, they have reported that degradation (or passivation) of their cells occurs mainly over the first 100 h, and can be partially reactivated by *I–U* scanning in fuel-cell mode. Additionally, after the initial degradation, some reactivation occurred by operation at constant galvanostatic electrolysis conditions. Very recently, *Mogensen* and coworkers have reported the degradative effect of very low levels of impurities in the feed gases (≈ 5 ppb) on SOEC performance [27.87, 103, 104]. Treatment of the inlet gases to remove impurities fed to the Ni–YSZ electrode and LSM–YSZ electrode led to essentially no degradation over 600 h, at current densities up to $-750\,\text{mA/cm}^2$. Presumably, trace levels of sulfur compounds were responsible.

Sohal et al. have summarized degradation issues in SOECs during HTE [27.105]. The total polarization loss (degradation) consists of three dominant parts: Activation (or charge transfer) polarization (η_{act}), concentration (or diffusion) polarization which includes chemical reaction effects (η_{conc}), and ohmic resistance polarization (η_{ohm}). At the same temperatures and current densities, the η_{act} and η_{ohm} are likely to be very similar. The η_{conc} is different because the gas transport mechanisms through the electrodes are different. A nonexhaustive list of leading causes for SOEC degradation is as follows:

- Microstructural changes in bond layer on the anode (O_2 electrode)
- Cr poisoning and dissociation of the bond layer on the anode
- Resulting delamination of the anode
- Loss of electrical–ionic conductivity of the electrolyte
- Generation of contaminants from the interconnects.

Delamination of the anode and the resulting degradation has been a significant problem, especially related to LSM-type materials [27.79, 91]. *Chen* and

Jiang [27.106] recently reported the degradation of an LSM anode in SOEC mode over 48 h ($-500\,\text{mA/cm}^2$ current density, 800 °C) [27.106]. Significant increases in electrode polarization and ohmic resistances were observed. In the delaminated cell, the formation of nanoparticles at the electrode–electrolyte interface was noted, caused by local disintegration of LSM grains at the interface. One proposed mechanism for the delamination is the incorporation of O^{2-} ions from the YSZ electrolyte into the LSM grain, leading to shrinkage of the LSM lattice. This, in turn, creates local tensile strains, resulting in microcracks and subsequent nanoparticle formation. O'Brien et al. have also raised the possibility that the high rate of O_2 production can exert high pressure at the electrolyte–electrode interface, increasing chances for delamination.

Many authors make use of electrochemical impedance spectroscopy (EIS) as a tool to characterize the degradation [27.21, 26, 76, 77, 83, 96, 99, 104, 106]. *Kong* et al. noted that after thermal cycling, polarization resistances increased on the anode, indicating degradation of the TPB [27.82]. *Ebbesen* et al. [27.103] reported extensive EIS data for Ni–YSZ–YSZ–LSM–YSZ cells. At current densities up to $-500\,\text{mA/cm}^2$ at 850 °C, these researchers only observed polarization degradation (no ohmic degradation). They divide the polarization degradation into two mechanisms, one located at the Ni–YSZ electrode (100−200 Hz in the impedance spectra), and one minor mechanism located either at the Ni–YSZ or LSM–YSZ electrodes with a frequency of 1000−3000 Hz. The low-frequency mechanism is heavily influenced by feed impurities. An additional detailed EIS study, with an equivalent circuit, for SOEC is given by *Ouweltjes* et al. [27.96].

Impurities and Poisons. Chromium (Cr) and silica (Si) have also been reported as poisons in SOEC systems [27.91, 103]. Silica can be present at low levels in the steam, but can also be produced from glass seals used in stack manufacturing. Cr can arise from the materials used for interconnects and other balance of plant components, which liberate Cr vapor at electrolysis conditions [27.91, 103]. These contaminants often migrate to grain boundaries, blocking the active TPB, and increasing the polarization resistance. *Hauch* and coworkers in Denmark reported the formation of a glassy phase containing Si impurities developed at the TPB of the Ni–YSZ electrode in their cells [27.107]. The majority of the increased polarization resistance was confirmed by EIS to be due to this electrode.

Virkar has recently reported on the mechanism of oxygen electrode delamination in SOEC [27.109]. An electrochemical model was developed, which indicates

Table 27.5 Solar conversion efficiencies and other related data for solar photolysis of water using global AM1.5 solar radiation (after [27.108])

Scheme	Conditions	η_P (%)	η_C (%)	U_{loss} per photon (eV)	Threshold wavelengths (nm)	
					λ_0 or λ_1	λ_2
S1	Ideal limit	5.3	–	0.49	420	–
S2	Ideal limit	30.7	–	0.37	775	–
S2	Chemical conversion	–	23.5	0.60	680	–
S2	Chemical conversion	–	17.4	0.80	610	–
S2	Chemical conversion	–	12.7	1.00	555	–
S4	Ideal limit	30.6	–	0.31	1340	–
D2	Ideal limit	42.4	–	0.38[a]	655	930
D4	Ideal limit	41.0	–	0.31[a]	910	2610
D4	Chemical conversion	–	32.3	0.60	785	1465
D4	Chemical conversion	–	27.1	0.80	720	1120
D4	Chemical conversion	–	21.6	1.00	655	925

In schemes D2 and D4, it is assumed that equal photon fluxes are used by the two photosystems
[a] Average U_{loss} per photon

oxygen electrode delamination arises via high internal oxygen pressure within the electrolyte. Particularly noteworthy findings from this modeling are that modest changes in the *electronic* conductance can cause orders of magnitude changes in the oxygen pressure, and a small amount of electronic conduction through the electrolyte is actually preferred from a stability standpoint. Thus, addition of ceria (or other metal oxides comprised of metals with multiple valence states) should decrease the delamination tendency [27.109].

27.2.3 Photoelectrolysis

There are two parts to the efficiency of photoelectrolysis: the photovoltaic (η_{pv}) and Faradaic (η_F) efficiencies. The overall efficiency, often referred to as the solar-to-hydrogen (STH) efficiency of a cell (η_{sth}), is defined as the product of these quantities

$$\eta_{sth} = \eta_{pv} \times \eta_F .$$

Challenges and Strategies in Cell Design

Even in the case of the most quickly degrading photoelectrodes, the Faradaic efficiency is nearly unity [27.110]. Implicit in this observation are the conclusions that (1) even the smallest measurable Faradaic inefficiency is extremely important to the long-term success of the PEC cell, and (2) discussion of the overall STH efficiency is dominated by the photovoltaics half of the problem.

Efficiency Limits. The photovoltaic efficiency limits of PEC processes have been evaluated for various cell-operating scenarios [27.108, 111].

Reproduced in Table 27.5 is a summary of the conclusions from *Bolton* et al. [27.108], who investigated the photovoltaic-based efficiency limits of PEC cells in both the 1-junction and 2-junction scenarios. In all cases there is a necessary loss of energy, relative to the band gap of the light harvester, which is required to drive the charge separation and electrochemical processes. Without knowing exactly what those losses will be for a real system, the authors give efficiencies for a realistic range of values in each case, either ignoring (U_{loss} under *ideal limit*) or taking into account (U_{loss} under *chemical conversion*) the overpotential for electrolysis. The scheme abbreviations are defined as follows: S1 is a single junction cell that converts 1 photon into 2 electron–hole pairs (requires 1 photon for each molecule of hydrogen produced); S2 is a single junction cell that converts 2 photons into 2 electron–hole pairs (requires 2 photons for each molecule of hydrogen produced); D2 is a stacked double junction cell that converts 2 photons into 2 electron–hole pairs (requires 2 photons for each molecule of hydrogen produced); and D4 is a stacked double junction cell that converts 4 photons into 2 electron–hole pairs (requires 4 photons for each molecule of hydrogen produced). In the case of a double junction (type *D*) cell, the efficiency limits depend on the bandgaps of both junctions, as shown in Fig. 27.18, and are maximized when the achievable photocurrents of the two junctions are equivalent (i. e., when the top junction absorbs the same number of short-wavelength photons as the underlying junction absorbs penetrating, longer wavelength photons). The most physically realistic designs are S2 and D4, which are reported to have theoretical efficiency maxima in the ranges of 13−24% and 22−32%, respectively.
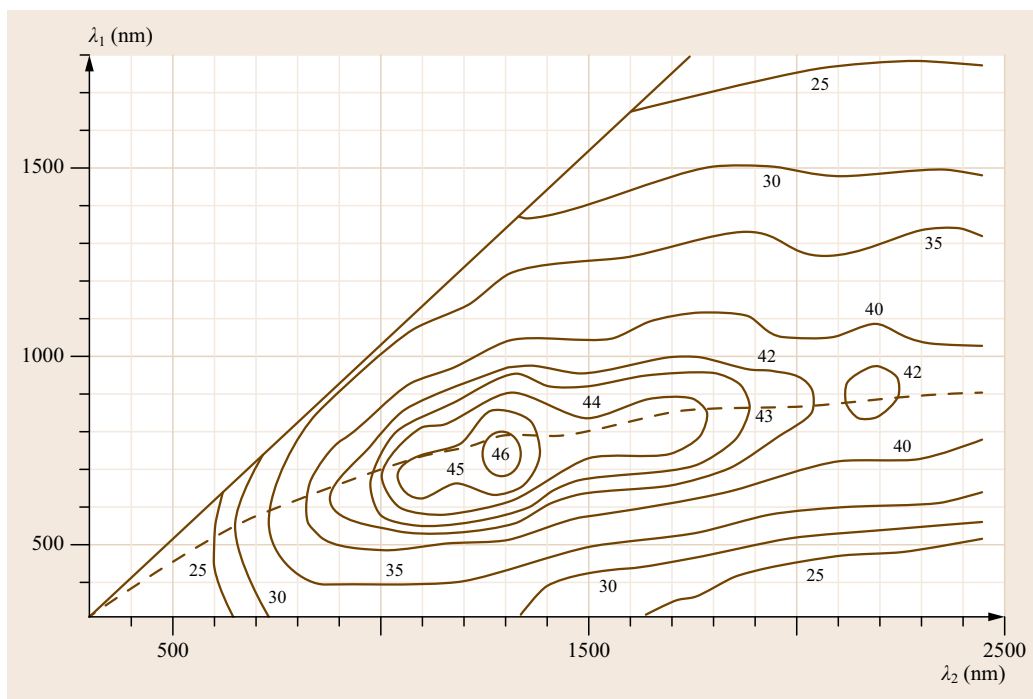
Fig. 27.18 Contour diagram showing the ideal limiting efficiencies η_P, in a layered dual-bandgap system with bandgap wavelengths λ_1 and λ_2. *Dashed line*: Path of equal effective photon fluxes used in two photosystems as required for use of the two halves in series (after [27.108])

Electrochemical Stability. It has been recognized that materials known to possess good photovoltaic properties, for example, transition metal chalcogenides and pnictogenides, are poorly suited for use in PEC due to electrochemical instability [27.112, 113]. Meanwhile, electrochemically stable materials typically exhibit poor photovoltaic efficiency. The two strategies that research has adopted in response to this significant challenge are (1) an attempt to imbue stable semiconductors (metal oxides) with better photovoltaic properties and (2) an effort to electrochemically stabilize known photovoltaic materials. As a result, the main thrust in this field has been in the direction of material discovery [27.114, 115] and novel photoelectrode design [27.116].

Photoelectrolysis presents a significant material challenge. Conventional solar cells are typically encapsulated to prevent exposure to moisture and oxygen, either of which can lead to photocorrosion problems over time. When immersed in water and used to generate oxygen under high illumination, temperature, and pressure, extreme electrochemical stability is required from the light absorber. Typical materials used in photovoltaics, particularly group IV elements, III–V compounds [27.114, 117–119], II–VI materials [27.120–123], Cu(In,Ga)Se$_2$ [27.124], and other metal chalcogenides [27.125], are especially susceptible to PEC degradation in aqueous environment. Because these materials are more vulnerable to anodic rather than ca-

thodic degradation, it was universally found that their stability is enhanced at low pH under cathodic protection.

The same is not always true for metal oxide semiconductors, where photodegradation is often caused by cathodic stress. Unconventional in the field of photovoltaics due to their generally poor charge transport and often large bandgaps compared to nonoxide semiconductors, metal oxide materials are often employed as photoanodes for hydrogen production due to the promise of enhanced stability. However, even the most stable of these materials can have problems in the harsh environments of photoelectrolysis. Strontium titanate, for example, is known to be indefinitely stable in alkaline electrolyte, but photodegrades very quickly at low and neutral pH [27.110]. Similarly, the stability of most metal oxide semiconductors prefers a specific pH range, the value of which can vary tremendously. In Table 27.6 a survey of common metal oxides and mixed oxides can be found, with stable pH range, reproduced from a thorough review of metal oxide stabilities by *Scaife* [27.126].

Peripheral Challenges. In addition to the chemical challenges involved with achieving efficient PEC hydrogen evolution, there are also several engineering obstacles to consider. The impracticality of storing or transporting large amounts of near-atmospheric pressure hydrogen gas necessitates its compression. Pres-

Table 27.6 Thermodynamic stability of oxides toward photoanodic decomposition (after [27.126])

Oxides stable pH 0–14	Oxides unstable pH 0–14	Oxides stable over some pH range with pH range for stability					
Fe_2O_2	MnO	CoO (6.8–14)	Al_2O_3 (2.9–14)	$MgTiO_3$ (4.7–14)	$CrNbO_4$ (0–4.3)	$MgNb_2O_6$ (1.9–14)[a]
TiO_2	SnO	NiO (6.2–14)	In_2O_3 (2.2–14)	$CaTiO_3$ (6.5–14)	Co_2TiO_4 (4.4–14)	$FeNb_2O_6$ (0.2–11.9)[a]
SnO_2	PbO	CuO (3.7–14)	Ga_2O_3 (0.9–14)	$SrTiO_3$ (5.9–14)	Zn_2TiO_4 (4.2–14)	$ZnNb_2O_6$ (0.2–13.9)[a]
ZrO_2	Cr_2O_3	ZnO (5.8–14)	Bi_2O_3 (1.5–14)	$Sr_{0.5}Ba_{0.5}TiO_3$ (6.8–14)	Cd_2SnO_4 (5.3–14)	$FeTa_2O_6$ (3.2–10.7)
Ta_2O_5	La_2O_3	CdO (7.6–14)	Y_2O_3 (8.5–14)	$Ca_{0.2}Ba_{0.8}TiO_3$ (7.3–14)	Zn_2SnO_4 (3.5–14)	$CrTi_2O_7$ (1.0–4.8)
$NaNbO_3$	Ti_nO_{2n-1}[b]	HgO (1.2–14)	Nb_2O_5 (0–12.2)	$BaTiO_3$ (7.4–14)	$CdFe_2O_4$ (1.6–14)	$La_2Ti_2O_7$ (3.0–14)[a]
$KNbO_3$	NbO_2	WO_3 (0–2.4)		$FeTiO_3$ (4.9–14)	$CdIn_2O_4$ (3.4–14)[a]	Sr_2FeNbO_6 (5.1–14)[a]
$FeNbO_4$	U_3O_8			$CoTiO_3$ (1.7–14)	$CdGa_2O_2$ (2.4–14)	
$LaNbO_4$	$MnTiO_3$			$NiTiO_3$ (2.1–14)	Al_2TiO_5 (2.0–14)	
$FeTaO_4$	$CdTiO_3$			$PbTiO_3$ (1.1–2.3)	$MgTi_2O_5$ (3.5–14)	
Fe_2TiO_5	Mn_2TiO_4			$LiNbO_3$ (1.1–14)		
$CaNb_2O_5$	Fe_2TiO_4			$YFeO_3$ (4.2–14)		
$SrNb_2O_6$[a]				$CdSnO_3$ (0.4–14)[a]		
$BaNb_2O_6$[a]				$BaSnO_3$ (0.4–14)[a]		
$CoNb_2O_6$[a]						
$NiNb_2O_6$[a]						
$TiNb_2O_7$						
$Hg_2Nb_2O_7$						
$Hg_2Ta_2O_7$						
$Pb_4Ti_3WO_{13}$[a]						
$PbFe_{12}O_{19}$						

[a] Using estimated values of ΔG_f (298.15); [b] where $n = 4$–8

surization of hydrogen is more challenging than that of other gases due to its small mass. While it contains the largest energy density of any possible fuel, it also results in the largest pressure density of any possible product gas. A multiple stage hydrogen compressor is required to affordably bring hydrogen to significant pressure. While this equipment contributes significantly to the one-time expense of a hydrogen-producing facility, its energy requirement is also nonnegligible in the long run. Figure 27.19 from the work of *Bossel* is a diagram depicting the power requirement of hydrogen compression [27.127]. For viewing convenience, the energy axis was herein normalized by the combustion energy of the hydrogen product under standard conditions, rather than reported in the originally published megajoules per kilogram.

This thermodynamic requirement of compression, along with the large capital cost of the compressor, both highlight the advantages possible in producing hydrogen electrochemically at already-elevated pressure. However, such a task becomes very difficult when the other requirements of PEC hydrogen production are put into place:

1. Light is required to efficiently penetrate the pressurized cell.

2. The compressed hydrogen and oxygen products must be kept separate from each other, requiring either a low-resistance membrane or laminar flow-cell design.

3. In designs that rely on both a photocathode and photoanode operating in series, the incoming light must be distributed to both halves of the reaction, or, in the ideal case the two electrodes would make use of different spectral regions of sunlight, and be situated on top of each other in a monolithic arrangement.

Owing to the underdeveloped technical state of PEC hydrogen production, these future issues surrounding cell design are rarely discussed in detail.

Electrode Design. Module design plays a major role in determining a conventional solar cell's efficiency limit [27.128]. Analogously PEC hydrogen generation, which is strongly limited by the photovoltaics side of the process, has been shown to benefit from the use of advanced cell designs [27.129]. Discussed in this section are several common strategies that have been explored.

The most straightforward PEC cell design consists of a single photoelectrode connected in series with a counter electrode. This system possesses the
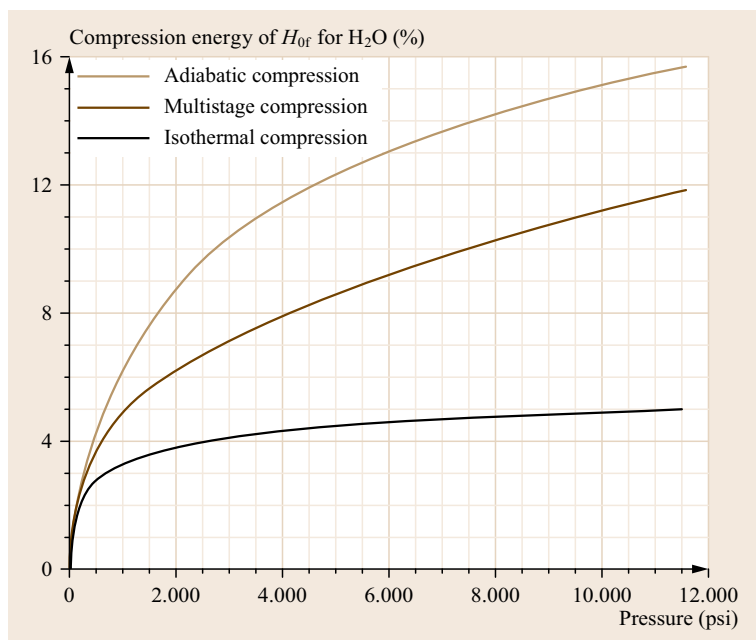
Compression energy of H_{0f} for H_2O (%)

Fig. 27.19 The energy cost of hydrogen compression starting from ambient atmosphere, given in units of hydrogen combustion energy as a function of final pressure (after [27.127])

advantage of simplicity; the study of individual photo-electrodes is facilitated when only one light-sensitive electrode is present. A voltage bias between the two electrodes, from a power supply, is often used to mimic the contribution from a second photoactive junction. In this way, the study of single junctions enables the careful study of photoelectrodes that are intended ultimately for use in multiple-junction PEC cells. However, photo-electrodes intended for self-sufficient (unbiased) use in single-photoelectrode cells are not known to reach solar-to-hydrogen efficiencies beyond 1% [27.130]. The explanation is a deficit of photovoltage. In addition to the 0.4 V energy drop required to drive exciton separation [27.131], an additional 0.3 V of overpotential is necessary to drive each of the electrode processes (anodic and cathodic) at reasonable current, on top of the 1.23 V thermodynamic requirement [27.132]. Each photon usable by a single, unbiased photoelectrode must therefore contain energy in excess of $\approx 2.2\,\mathrm{eV}$, limiting the efficiency to 12.7% and narrowing the list of usable semiconductors. In practice, it is observed that closer to 3 eV band gaps are necessary to achieve measurable performance, limiting η_{sth} to 2% [27.108, 116, 130, 133, 134].

A photoanode–photocathode combination has the capacity to be more efficient than a single photoelectrode. The critical difference lies in their respective absorption of the solar spectrum. Two photoelectrodes in series can have small band gaps, yet still be capable of driving electrolysis using the sum of their photovoltages. This allows their absorption to extend much

further into the visible wavelengths of the solar spectrum, improving η_{pv}. It should be noted, however, that because the two junctions operate in series, their photocurrents are by definition identical. The implication is that two photons are now absorbed to generate each electron that is ultimately passed around the external circuit, limiting the external quantum efficiency (EQE) to 50% of what can be expected from a single junction. Overall, the improved light absorption outweighs this limitation in the theoretical efficiency limit. The first tandem PEC cell was reported in 1975 by *Yoneyama* et al. [27.113]. Similar to the single photoelectrode cell demonstrated by *Fujishima* and *Honda* [27.25], the Yoneyama cell used a p-GaP photocathode in series with n-TiO$_2$ to provide the additional photovoltage needed to split water, with a rapidly degrading η_{STH} starting at 1.2%. Similar cells were described shortly thereafter by *Nozik* [27.135] and then later more efficiently by *Bockris* and *Kainthla* (8.2% solar-to-hydrogen efficiency) [27.136] and others.

The concept of biasing photoelectrodes with standard p–n junctions has also been explored. When the p–n junction lies monolithically beneath (i. e., absorbing from the same pool of light as) the photoelectrode, the device is referred to as a buried junction. Khaselev and Turner reported 12.4% solar-to-hydrogen efficiency under 11 suns illumination from a platinum-catalyzed p-GaInP$_2$ photocathode biased with a GaAs p–n buried junction. It was stated to be essential for device performance that the absorption of light by the underlying GaAs layer limit the overall photocurrent generated
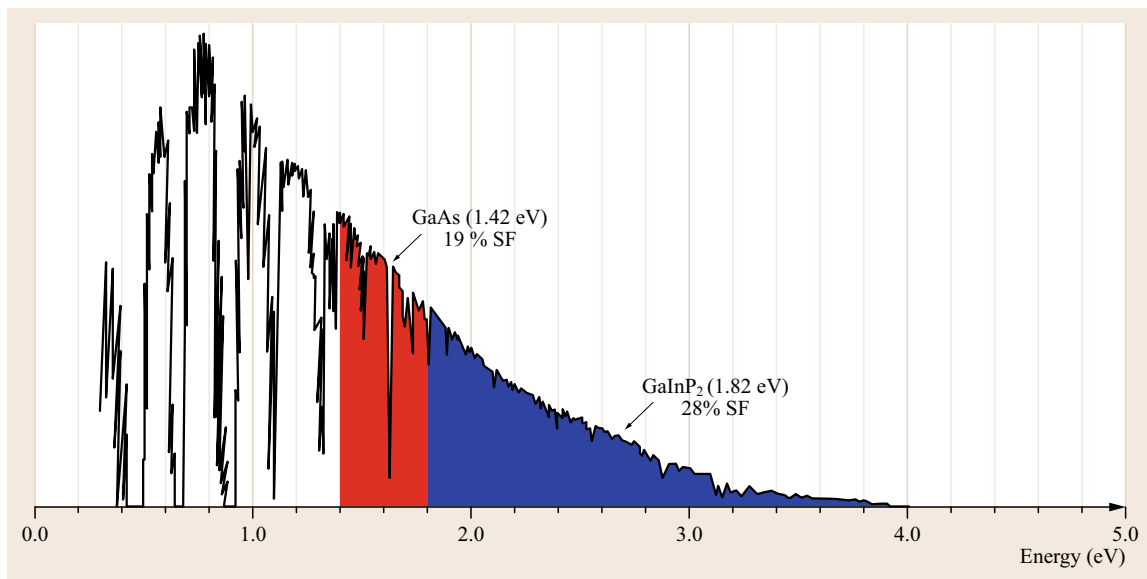
Fig. 27.20 Solar spectrum utilization from the photocathode reported by *Khaselev* and *Turner*, broken down by layer (after [27.29]). The photocurrent generated by the GaAs layer limits that of the overall device

by the device. The spectral utilization of each layer is shown in Fig. 27.20. As with many examples of III–V light harvesters, this efficient photocathode suffered from electrochemical instability.

Notable Photoelectrode Materials
Most of the photoactive materials common to photovoltaics have been studied as cathodes in PEC cells.

Conventional for PV. There are examples demonstrating appreciable and sometimes extraordinary performance from photocathodes based on silicon [27.137], group III–V materials [27.29, 113, 138], group II–VI materials [27.139, 140], Cu(In,Ga)Se$_2$ [27.141], and Cu$_2$ZnSnS$_4$ [27.142].

The use of these semiconductors as photoanodes, however, is less common due to problems with electrochemical corrosion under oxidative stress. There are nevertheless a few examples in which researchers have enhanced the stability of these materials, generally by coating the photoactive layer with a very thin film of stable metal oxides [27.143–146].

Unconventional for PV. A wide variety of mixed metal oxide semiconductors have been explored for favorable electrochemical and photovoltaic properties, namely a reasonably small band gap, good charge mobility in both the conduction and valence band, appropriate band edge potentials, electrochemical stability, and photochemical stability. No single material, oxide or otherwise, has yet been reported to embody all these qualities. A noncomprehensive survey of nonconventional (oxide) semiconductors studied for PEC, reproduced from the work of *Scaife* [27.126], is presented in Fig. 27.21. The most commonly studied classes of material include zinc oxides [27.147], tantalates [27.148, 149], tungstates [27.150], chromates [27.151], ferrites, and titanates [27.152–154].

One of the key challenges when working with metal oxides is the movement of charge throughout the solid. Hematite, Fe$_2$O$_3$, has been widely recognized as an interesting PEC challenge [27.155]. Despite being abundant, stable, and good at absorbing light [27.156], hematite has poor electron and hole conductivity, rampant charge recombination (as a consequence), nonideal band-edge potentials, and poor catalytic activity toward water decomposition [27.157, 158]. Much work has been done by the *Grätzel* group to compensate for the drawbacks of Fe$_2$O$_3$ by doping it with other elements [27.159], as well as reducing the dimensions of the photoactive layer [27.160, 161]. Photovoltages achieved by hematite-based photoanodes are on the order of 0.8 V, with photocurrents reaching a maximum of $\approx 3\,\mathrm{mA/cm^2}$ when biased externally [27.162].

It is far rarer to find reports of metal oxide photocathodes. There have been a handful of studies related to photocathodes based on cuprates [27.163] and ferrites [27.164], though with stability issues in each case. The cathodic degradation mechanism is different than anodic. Instead of material dissolution from the photoactive layer, the metal atoms in the cathodes tend to reduce, forming splinters of conductive metal within
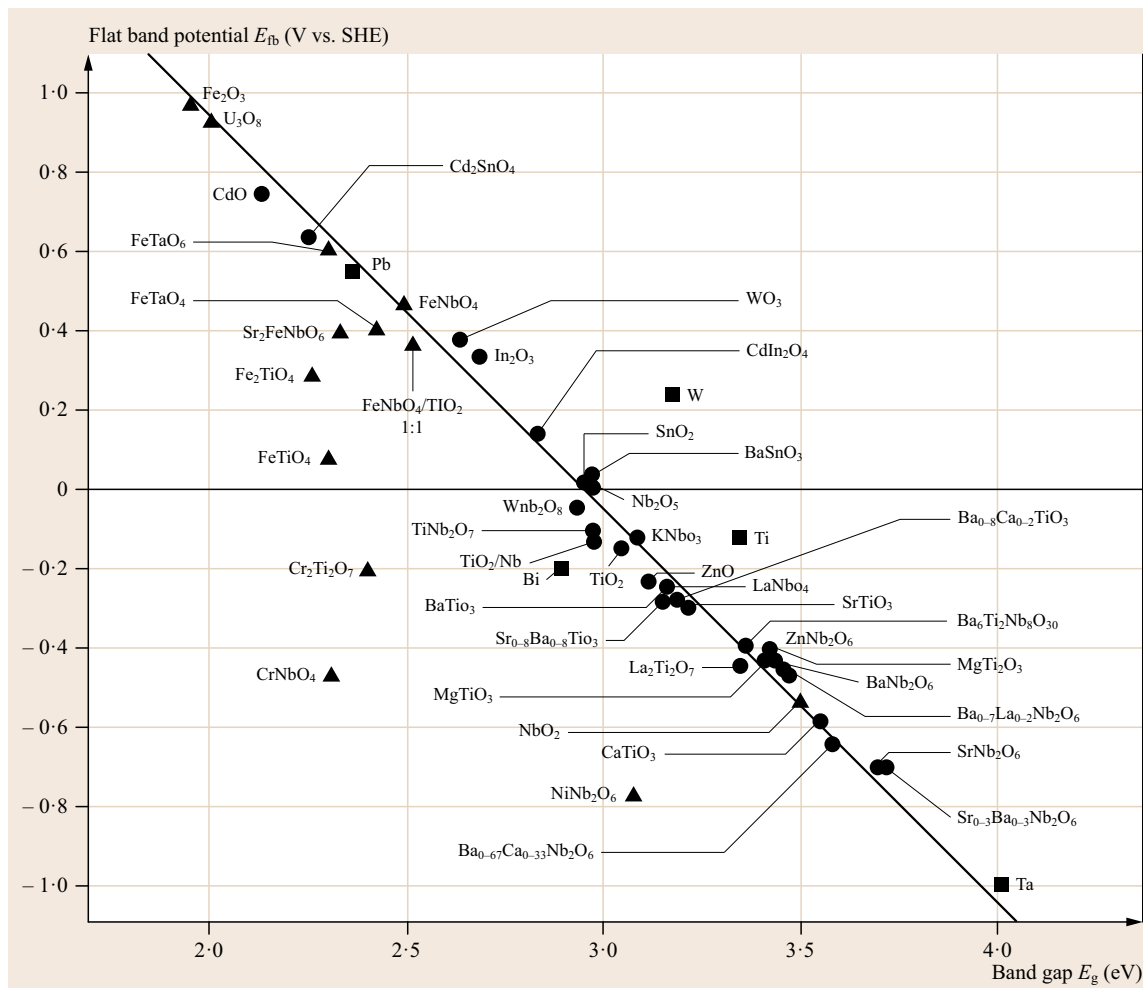
Fig. 27.21 Measured flat band potentials and effective band gaps in semi-conducting oxides. *Circles*: Oxides without partially filled d-levels. *Triangles*: Oxides with partially filled d-levels. *Squares*: Oxides formed anodically on metals (after [27.126])

the oxide semiconductor. When this happens, the electrolyte interface can short circuit with the underlying conductive support, rendering charge separation ineffective.

Performance–Enhancing Surface Modification. It has become more widely recognized in recent years that electrode surfaces can be modified with submicron features, or with performance-enhancing additives, to enable unexpected photo- or electrocatalytic properties [27.165]. As an illustrative example, the surface modification of TiO_2 to achieve ordered nanotube arrays has received much recent attention [27.166–173]. It was found by the Bard and Misra groups that anodically prepared TiO_2 nanotube arrays exhibit dramatically enhanced photovoltaic characteristics over

typical TiO_2 wafers. The *Bard* group reported more than a factor of 10 improvement in photocurrent from carbon-doped TiO_2 nanotubes as compared to a $15\,\mu m$, featureless film of the same material [27.174]. Using catalyst-enhanced TiO_2 nanotube arrays for both the photoanode (carbon doped) and cathode, the *Misra* group reports a PEC cell efficiency for water splitting of 8.5% [27.175, 176].

Addition of submicron catalyst particles to the surface of photoelectrodes is also known to strongly affect performance. An example of the powerful effect that electrochemical catalysis can have on the activity and stability of a photoelectrode is presented by the *Domen* group [27.177]. In their study of a tantalum oxynitride photoelectrode (TaON), it was discovered that $\approx 1\,mA/cm^2$ photocurrent diminished to zero very

quickly during operation (on the order of seconds), due to the photocorrosion of the electrode to form Ta_2O_5. It was found that addition of an IrO_2 oxygen evolution catalyst to the surface of the TaON electrode had a profound effect on the electrode's performance. First, the photocurrent generated by the electrode was improved by a factor of 3 over uncatalyzed TaON. In addition, incorporation of IrO_2 as a charge collector prevented anodic leaching of nitrogen out of the electrode surface. The result was an electrode that sustained its photocurrent on the order of hours instead of seconds.

A final way in which surface additives can aid solar-to-hydrogen efficiency is by enhancing the absorption of light by the semiconductor. An area of growing interest is the addition of plasmonic metal nanostructures to the surface of semiconductors [27.178]. Surface plasmon resonance describes the storage of photonic energy in the form of a standing wave within a metal body. It has been shown by *Ingram* and *Linic* that photovoltaic enhancement of a PEC cell can be achieved with visible wavelengths by the addition of silver nanostructures to a n-TiO_2 photoanode [27.179]. The authors saw significant, sustained photocurrent enhancement (roughly an order of magnitude) over the silver-free control electrode. They attribute this effect to an enhanced probability of photonic absorption at the semiconductor's surface, due to the presence of the silver, as opposed to more general absorption within the bulk of the TiO_2 (where the charge-separating electric field is much weaker).

27.3 Development Perspectives

Findings from a technoeconomic analysis of today's commercial electrolyzers suggest that electricity costs are a major contributor to the cost of hydrogen, regardless of the system size [27.15]. It was also found that capital cost reduction is needed for smaller scale electrolyzers to reduce H_2 costs. Figure 27.22 shows the status of current-day commercial electrolyzers in terms of the electricity consumption as a function of the electrolyzer capacity. The HHV of hydrogen is $3.5\,kWh/Nm^3$ and the system efficiency is defined as the ratio of the HHV and the electricity consumption (y-axis of Fig. 27.22).

System efficiencies of large-scale alkaline electrolyzers ($> 100\,Nm^3/h$) such as those made by StatOil (previously Norsk Hydro) and ELT are in the range of 75−80%. Medium-sized electrolyzers ($10−100\,Nm^3/h$) by Teledyne (PEM) and Hydrogenics (alkaline) have lower system efficiencies (60−70%). Small-scale electrolyzers ($< 10\,Nm^3/h$) manufactured by Proton Energy Systems and PIEL (ILT Technologies) have system efficiencies in the range of 50−60%. Electrolyzers with high production capacities achieve lower power consumption or higher efficiency. This can be mainly attributed to the improved efficiency of ancillary components with increasing size. Existing commercial alkaline electrolyzers spans three orders of magnitude in capacity. All these electrolysis units are sized to meet the demands of current nonrefinery hydrogen markets. Only electrolyzers 10−100 times the size of today's largest units could meet the minimum capacity requirement of a typical refinery.

The cost of the electricity will have a dominant effect on the H_2 price, accounting for $> 75\%$ of the total cost in SOEC-based systems. Researchers at the National Renewable Energy Laboratory reported in 2007 the boundary electricity cost effect on H_2 costs. The electricity price would have to be less than $0.01/kWh for H_2 to be produced at $2/kg ($0.18/Nm^3). This is less than the cost to produce electricity from coal. For a production target of $3/kg, electricity costs were estimated to be $0.04 to $0.055/kWh for electrolyzer efficiencies of 72−58%, respectively. In another estimate, the electricity cost of $0.075 was needed to meet the $3/kg H_2 target even at 100% efficiency [27.180].

Floch et al. [27.181] reported a study on using off-peak grid power for an alkaline electrolyzer. Various production capacities up to $\approx 7200\,Nm^3$ H_2/h were modeled. Their results show a minimum in production cost of $2.56\,\text{€}/kg$ at $48\,\text{€}/MWh$ electricity cost (2005 basis). This corresponded to a 64.3% uptime, mainly operation at nights and on weekends. Savings by using the off-peak power were said to be significant, but varied enormously in different markets.

In addition to the efficiency limitation and cost of grid electricity, the associated CO_2 emission (a reasonable US value is $\approx 0.59\,kg$ CO_2/kWh) [27.182] is a significant barrier to the adoption of electrolysis as a low-carbon hydrogen production technology. The only meaningful choice for comparison of carbon intensity is the SMR technology. Praxair has published a white paper indicating that historical SMR units produce $\approx 10.8\,kg$ CO_2/kg H_2 [27.183]. Modern units are closer to $9.5\,kg$ CO_2/kg H_2. With credits for the high-quality steam that is typically exported in refineries, a 22% reduction is found for historical units ($\approx 8.7\,kg$ CO_2/kg H_2). This CO_2 is produced during water gas shift (process related) and from burning natural gas/fuel to provide heat (combustion-related).
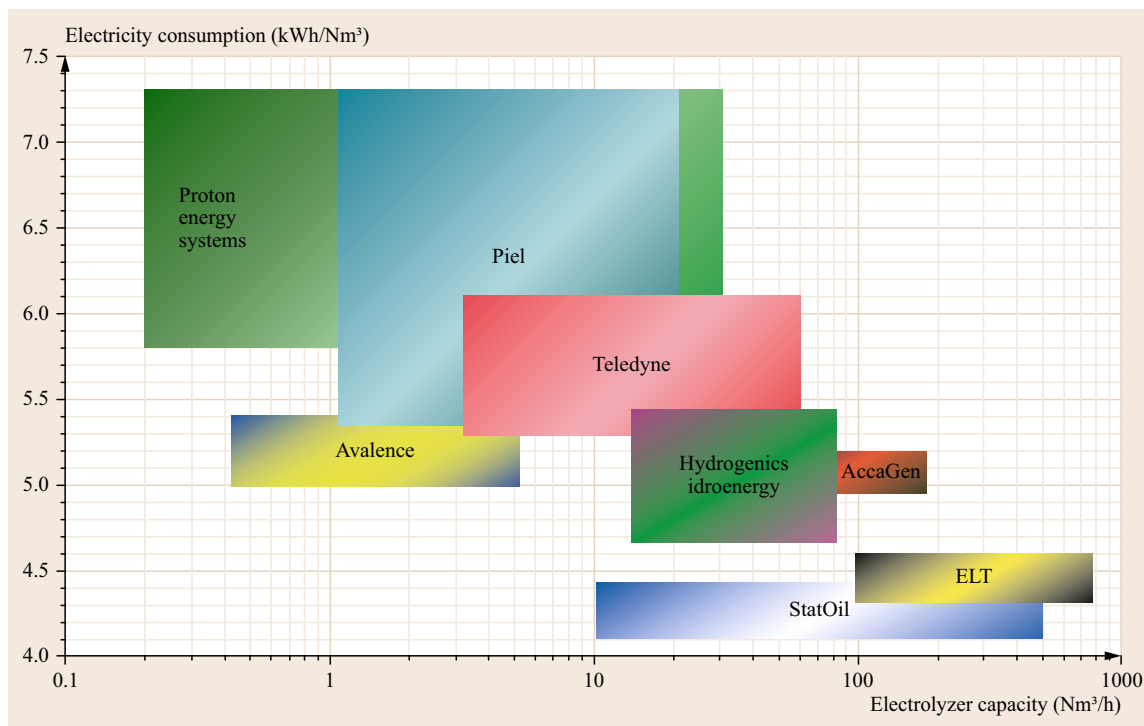
Fig. 27.22 Status of current commercial water electrolyzers in terms of the electricity consumption as a function of the electrolyzer capacity ($Nm^3 \equiv$ normal cubic meter $= 0.09\,kg\,H_2$)

For the purpose of comparison, a CO_2 production rate of $10.8\,kg\,CO_2/kg\,H_2$ can be used as a reasonable upper boundary for SMR technology. If one assumes an electricity demand of $33\,kWh/kg\,H_2$ (thermodynamic limit, V_N for low-temperature electrolysis), a CO_2 intensity of $19\,kg\,CO_2/kg\,H_2$ is easily calculated based on the assumed grid power CO_2 footprint given above (Fig. 27.23). This ignores any other source of CO_2 emissions for SOEC operations. At \$0.07/kWh, the electricity costs are seven times as expensive as natural gas on an energy basis, using a natural gas price of \$3 per gigajoule. Thus, using the lowest reasonable expected power consumption for electrolytic H_2 production, grid-powered electrolysis has double the amount of CO_2 relative to SMR.

Renewable and low-carbon electricity sources, such as solar, wind, and nuclear power, also play a critical role in the development of renewable H_2 production. Spanish researchers [27.184] have published a study on the performance of an alkaline electrolyzer ($1\,Nm^3/h$ rated H_2 production) working under emulated wind conditions. Wind speed data from a wind farm were used to establish a power profile for a wind turbine of some rated power that was emulated by a power supply designed and built in house. Their results indicated a narrow range of specific energy consumption

of $3.60-4.05\,kWh/Nm^3\,H_2$ ($40-45\,kWh/kg\,H_2$) over variable emulated wind energy input. The stack voltage matched the electric current–time profile, which the authors suggest is essentially ohmic behavior governed by internal resistances of the electrolyte (30% KOH) and cell components. No costs were provided, but good electrolyzer performance was noted.

In a recent report, researchers from National Renewable Energy Laboratory (NREL) the Colorado School of Mines and Xcel Energy in Colorado offered a technical report on opportunities for electrolysis for electric power utilities [27.185]. Hydrogen delivered costs as a function of electricity price were modeled where the electrolyzer farm was sized to the maximum wind farm capacity. With a capacity factor of 41% (an intermediate factor in their study), costs were about \$12/kg H_2 (2005 basis) at an electricity cost of \$0.10/kWh, using given economic assumptions. Some benefits (in addition to storage of intermittent wind energy) were to use electrolyzers in off-peak periods to run the power system closer to rated capacity (and raise its overall efficiency). Additionally, when off-peak power is inexpensive, H_2 can be produced and stored for later use via fuel cell or H_2-engine generator to produce power.

The NREL authors concluded that ample resources of solar and wind-derived power exist in the US for
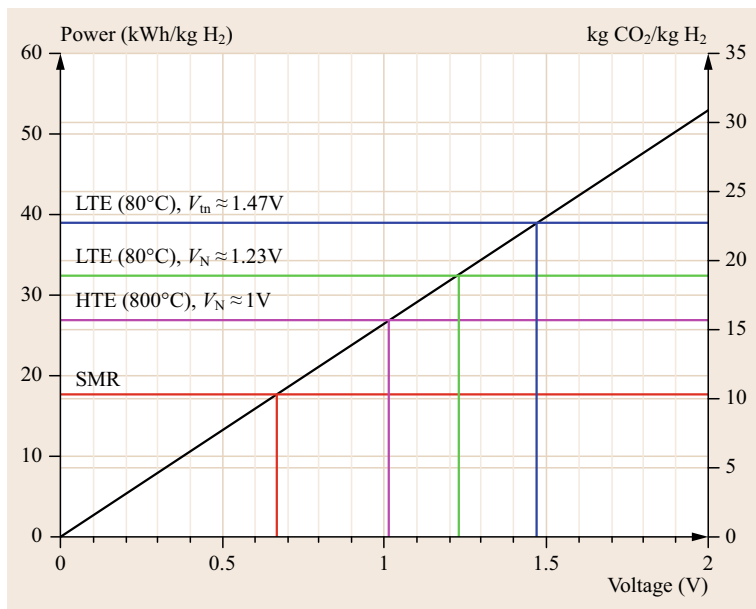
Fig. 27.23 Power requirements and CO_2 footprint as a function of the applied voltage for water electrolysis and comparison with SMR

electrolysis of H_2. Currently, electricity from these sources typically commands a premium price, although efforts are showing progress for *grid parity* of these clean power technologies. To produce H_2 electrolytically with a CO_2 footprint less than SMR, then using the hypothetical electrolysis system above the supply of electricity should have a carbon intensity of ≈ 0.32 kg CO_2/kWh or less. Natural gas supplied power plants approach this value, but still exceed it. A mix of wind, hydroelectric, nuclear, and/or solar, with natural gas, could conceivably produce a power supply with the appropriate CO_2 footprint. However, the power costs can prove challenging. Abbasi and Abbasi recently published estimates for *renewable* H_2 costs [27.186]. They report SMR costs at \$1.03/kg, coal gasification at \$0.96/kg, but wind electrolysis at \$6.64/kg. Both biomass pyrolysis (\$3.8/kg) and biomass gasification (\$4.63) are less than the wind-powered case. For reference, the authors report gasoline production cost of \$0.93/gallon refined.

For a solar-powered electrolysis process, the PV module costs must be reduced by one-third over the present cost. The National Research Council (NRC) in the United States estimated that the H_2 produced from a solar-powered electrolysis process would exceed \$28/kg at \$3.28/W_{Peak} (installed) and electricity cost of \$0.32/kWh [27.187]. The NRC projected that H_2 costs could be reduced to \$6.18/kg (assuming improvements in PV technology and electricity costs of \$0.098/kWh).

HTE of steam requires less electricity than conventional low-temperature electrolysis. However, there are still significant barriers to large-scale implementation.

The largest factors impacting the potential economics of HTE are:

1. The cost of electricity
2. Capital expense (CAPEX)
3. Cell degradation
4. Uncertainties with scale up of new technology.

INL has been involved with a detailed program on HTE for large-scale H_2 and syngas production from nuclear energy. A report on the simulation and economics in 2010 showed the potential for a 2.2 million Nm^3/d (≈ 200 t H_2/d) plant with a 600 MW reactor [27.188]. Production cost using the H2A Analysis Methodology developed by Department of Energy H_2 program was estimated to be \$3.23/kg (leaving the plant gate at 5 MPa pressure). The estimated price was shown to be most sensitive to the assumed after-tax internal rate of return (typically 10%) and unplanned replacement costs. In this case, 70% of the H_2 price was due to capital costs (high costs for nuclear reactors). The authors report a commodity price of \$2.50/kg for H_2 from SMR technology for comparison, but this is probably too high at current natural gas prices. Nevertheless, these transparent and documented procedures likely result in a reasonable estimate of H_2 production cost from a *world scale* SOEC plant.

A dated but informative life cycle analysis (LCA) by NREL on wind-powered electrolysis shows a remarkably low 0.97 kg CO_2/kg of net produced H_2 [27.190]. The bulk of the CO_2 was associated with turbine production and operation (78%) with a lesser fraction for compression and storage (17.6%) and very
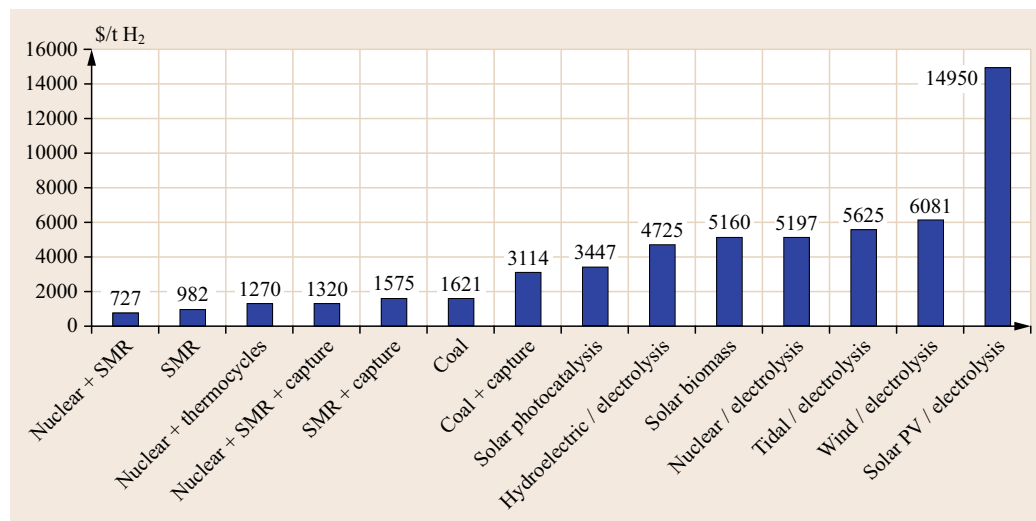
Fig. 27.24 H_2 production costs from different sources (after [27.189])

low emissions for electrolysis production and operations (4.4%). In addition, the energy balance was very favorable, with considerably more energy in the H_2 produced relative to the amount of fossil energy consumed.

Koroneos and coworkers [27.191] have published the results of an LCA for electrolysis powered by various renewable sources (PV, solar thermal, wind, hydroelectric, biomass) along with SMR from methane as a comparison. Impacts in addition to CO_2 (i.e., smog, acidification, eutrophication, carcinogens, ozone depletion, solid waste, and heavy metals) were considered in their analysis following generally accepted LCA methodology. Their conclusion was that wind, solar-thermal, and hydroelectric-based power for electrolysis were the most environmentally friendly options. *Ewan* and *Allen* assigned figures of merit for several different routes to H_2, and electrolysis was a common step in several approaches [27.189]. SMR, SMR + CO_2 capture, coal and other integrated nonelectrolysis processes were included (Fig. 27.24). Four feasibility criteria used in their analysis were CO_2 reduction, land use impacts, power limitations with the primary energy source, and production costs. A figure of merit (FOM) for each criteria was calculated. In turn, an overall FOM was then calculated from the individual FOM values. The results (not unexpectedly) showed processes based on SMR and coal had the best economics, but nuclear/thermocycle and coal + CO_2 capture scored reasonably high. The best score for an electrolysis-related process was the combination with nuclear energy. Solar PV, wind, and hydroelectric sources for electrolysis all had relatively low overall scores, primarily due to higher production costs. Interestingly, the hydroelectric case had the lowest overall score.

Lemus and *Duart* have provided a detailed cost analysis study for various H_2 production methods that include both electrolytic and bio-based technologies [27.192]. These authors have taken literature data for production costs, accounted for inflation, and provided some estimates for future costs. Their results for renewable energy/electrolysis processes show estimated H_2 production costs of \$5$-$15/kg, in reasonable agreement with Fig. 27.24.

A recent LCA on various hydrogen production strategies found that, among SMR, coal gasification, water electrolysis via wind and solar power, and a Cu–Cl thermochemical water-splitting cycle, the wind and solar powered electrolysis had the lowest global warming potentials [27.193]. In terms of CO_2 equivalent emissions, the wind/electrolysis route was the lowest, at $< 1 \, \text{kg} \, CO_2$ e/kg of net produced H_2, in agreement with *Spath* and *Mann* [27.188]. However, the authors pointed that out the production capacities for these processes were 4 orders of magnitude lower than the coal gasification example used in their study. The thermochemical Cu–Cl cycle also had very low reported CO_2 equivalent emissions, and was advantaged over the electrolysis options in view of greater production capacity opportunity. This study has a detailed and comprehensive set of economic inflows, emissions, and global warming potential (GWP).

A high-level review of water electrolysis technologies for hydrogen production has appeared recently, which includes possible configurations for coupling renewable energy systems to electrolysis in both autonomous and grid-connected systems [27.194]. The autonomous systems are separate from the grid and the hydrogen is completely renewable. Two types of au-

tonomous, or off-grid, systems were identified by *Ursua* et al. [27.194]. In one, the wind or solar PV system is coupled to the electrolyzer and H_2 (as well as O_2) is the only product. Such systems are subject to variable production, since the availability of wind and solar power fluctuates. The second off-line system incorporates H_2 storage and fuel cells, such that surplus renewable energy is stored as H_2, then converted to power in areas where the main grid is not accessible.

In grid-connected systems, three configurations were identified. In one, all electricity generated by the wind or solar system is continuously injected onto the grid. The electrolyzer is driven by a constant operating profile derived from the average of the renewable energy system, but does not include the variations. A second type uses the renewable energy directly, and excess renewable energy is supplied to the grid. In this case, the electrolyzer is subject to renewable energy variability. Under most circumstances, such an electrolyzer would be underutilized. The third configuration for grid-connected system allows the electrolyzer to participate in the instantaneous adjustment between the renewable energy generated by wind or solar units and the energy demanded by loads connected to the grid.

Demonstration projects integrating renewable energy and electrolysis were also noted for the United States, Canada, Germany, Italy, Norway, Finland, UK, Japan, and Spain [27.192]. Most were autonomous systems, isolated from the grid or microgrids. The use of solar PV energy is more common than wind, but some consider both options. Alkaline electrolyzers are typically employed but PEM-based systems are utilized as well.

The Wind2H2 project, led by NREL and Xcel Energy, integrates wind turbines and photovoltaic (PV) arrays with electrolyzer stacks to produce hydrogen (and oxygen) with renewably generated electricity [27.195]. The system uses two variable speed wind turbines with 100 and 10 kW capacity. Two PEM electrolyzers ($1.05\,\mathrm{Nm}^3/\mathrm{h}$ each) and one alkaline electrolyzer ($5.6\,\mathrm{Nm}^3/\mathrm{h}$) produce the hydrogen. Integration of these technologies as well as the operation of electrolyzers with different gas output pressures are part of the study. The H_2 is compressed and stored for later use in a hydrogen internal combustion engine where it is converted to electricity and fed into the utility grid during peak demand hours. Refueling of a passenger car was demonstrated in 2009. Base-line production price for the hydrogen was 6.25/kg.

Another demonstration project in Spain has been described recently [27.196]. In this project, excess energy from the large Sotovento wind farm (17.56 MW) is used to power an alkaline electrolyzer to produce hydrogen at a rate of $60\,\mathrm{Nm}^3/\mathrm{h}$. The hydrogen is compressed to 200 bar, then used as fuel for a 55 kW engine to supplement power when wind energy falls below targeted levels.

The demonstration projects described here and elsewhere [27.134, 197] clearly show that renewable hydrogen via electrolysis is feasible, but cost challenges remain. Technical improvements in all system components are documented, and cost reduction targets are identified.

27.4 Conclusions

As discussed in this chapter, the use of electrolysis for large scale, centralized hydrogen production is challenged by component costs and high electricity costs without assuming an unrealistic regulatory incentive. These technologies are unlikely to replace the mature and low-cost SMR in the foreseeable future, due largely to the contemporary expansion in the supply of natural gas in the United States (and Eurasia/Middle East) that has suppressed the costs of SMR-derived hydrogen.

However, the electrochemical hydrogen production technologies do offer potential advantages in a distributed hydrogen market, especially when the technologies are combined with renewable or low-carbon electricity sources. At smaller production capacities, the cost of H_2 from SMR increases due to the unfavorable economy of scale down. In anticipation of demand for renewable hydrogen (i. e., for greenhouse gas reduction and renewable fuels production), the coupling of low-carbon power sources to different electrolysis technologies has been demonstrated. In addition, electrochemical hydrogen production offers an opportunity to store energy from intermittent power sources such as wind and solar. As improvements and cost reductions in system components are realized, truly renewable hydrogen may emerge as a cost-effective commodity.

References

27.1   US Department of Energy: US Crude Oil, Natural Gas, and Natural Gas Liquids Proved Reserves 2009 (US Department of Energy, Washington 2010) http://www.eia.gov/pub/oil_gas/natural_gas/data_publications/crude_oil_natural_gas_reserves/current/pdf/arrsummary.pdf

27.2   C. Yang, J.M. Ogden: H_2 Production via Natural Gas Reforming, Task 4.1 Technology Assessments of Vehicle Fuels and Technologies (California Energy Commission, Sacramento 2007)

27.3   J.M. Ogden: Agreement on the Production and Utilization of Hydrogen Task 16, Hydrogen from Carbon-Containing Materials (International Energy Agency, Paris 2001)

27.4   National Research Council: Front Matter. The Hydrogen Economy: Opportunities, Costs, Barriers, and R and D Needs (National Academies Press, Washington 2004)

27.5   R. De Levie: The electrolysis of water, J. Electroanal. Chem. 476(1), 92–93 (1999)

27.6   S. Trasatti: Water electrolysis: who first?, J. Electroanal. Chem. 476(1), 90–91 (1999)

27.7   S. Trasatti: Alessandro Volta's electric pile: Two hundred years, but it doesn't seem like it, J. Electroanal. Chem. 460(1), 1–4 (1999)

27.8   W. Kreuter, H. Hofmann: Electrolysis: The important energy transformer in a world of sustainable energy, Int. J. Hydrogen Energy 23(8), 661–666 (1998)

27.9   K.J. Laidler: The chemical history of a current, Can. J. Chem. 75(11), 1552–1565 (1997)

27.10   G. Sandstede: Status of the technology and development in water electrolysis, Dechema Monogr. 125, 329–355 (1992)

27.11   R.L. Le Roy: Industrial water electrolysis: Present and future, Int. J. Hydrogen Energy 8(6), 401–417 (1983)

27.12   J.E. Noeggerath: Electrolytic apparatus, US Patent 1 799 116 (1931)

27.13   J.E. Noeggerath: Electrode vessel for electrolytic apparatus, US Patent 1 896 718 (1933)

27.14   H. Vandenborre: New developments in alkaline water electrolysis, Dechema Monogr. 98, 313–328 (1985)

27.15   J. Ivy: Summary of electrolytic hydrogen production. In: Milestone Completion Report (National Renewable Energy Laboratory, Golden 2004)

27.16   D. Pletcher, F.C. Walsh: Industrial Electrochemistry (Blackie Academic Professional, London 1990)

27.17   K.A. Mauritz, R.B. Moore: State of understanding of Nafion, Chem. Rev. 104(10), 4535–4585 (2004)

27.18   B.V. Tilak, P.W.T. Lu, J.E. Colman, S. Srinivasan: Electrolytic production of hydrogen. In: Comprehensive Treatise of Electrochemistry, Vol. 2, ed. by J.M. Bockris, B. Conway, E. Yeager, R. White (Plenum, NY 1981) pp. 1–104

27.19   W. Doenitz, R. Schmidberger, E. Steinheil, R. Streicher: Hydrogen production by high temperature electrolysis of water vapour, Int. J. Hydrogen Energy 5, 55–63 (1980)

27.20   A. Isenberg: Energy conversion via solid oxide electrolyte electrochemical cells at high temperatures, Solid State Ion 3–4, 431–437 (1981)

27.21   G. Schiller, A. Ansar, M. Lang, O. Patz: High temperature water electrolysis using metal supported solid oxide electrolyser cells (SOEC), J. Appl. Electrochem. 39, 293–301 (2009)

27.22   A.E. Becquerel: Mémoire sur les effets électriques produits sous l'influence des rayons solaires, Comptes Rendus 9, 561–567 (1839)

27.23   W.H. Brattain, C.G.B. Garrett: Physical theory of semiconductor surfaces, Phys. Rev. 99, 376–387 (1955)

27.24   C.N.R. Rao, J. Gopalakrishnan: New Directions in Solid State Chemistry (Cambridge Univ. Press, Cambridge 1997) pp. 416–419

27.25   A. Fujishima, K. Honda: Electrochemical photolysis of water at a semiconductor electrode, Nature 238, 37–38 (1972)

27.26   A. Brisse, J. Schefold, M. Zahid: High temperature water electrolysis in solid oxide cells, Int. J. Hydrogen Energy 33, 5375 (2008)

27.27   H. Gerischer: Electrochemical photo and solar cells – Principles and some experiments, Electroanal. Chem. Interf. Electrochem. 58, 263–274 (1975)

27.28   J.O. Bockris, K. Uosaki: Photoelectrochemical production of hydrogen, ACS Adv. Chem. 163, 33–70 (1977)

27.29   O. Khaselev, J.A. Turner: A monolithic photovoltaic-photoelectrochemical device for hydrogen production via water splitting, Science 280, 425–426 (1998)

27.30   S.U.M. Kahn, M. Al-Shahry, W.B. Ingler Jr.: Efficient photochemical water splitting by a chemically modified n-TiO$_2$, Science 297, 2243–2245 (2002)

27.31   M.S. Casper (Ed.): Hydrogen Manufacture by Electrolysis, Thermal Decomposition and Unusual Techniques (Noyes, Park Ridge 2007)

27.32   C.L. Mantell: Electrochemical Engineering, 4th edn. (McGraw Hill, New York 1960)

27.33   D.H. Smith: Industrial water electrolysis. In: Industrial Electrochemical Processes, ed. by A.T. Kuhn (Elsevier, Amsterdam 1971), Chap. 4

27.34   B. Kroposki, K. Harrison, P.K. Sen, J. Levene, F. Novachek: Electrolysis: Information and Opportunities for Electric Power Utilities (National Renewable Energy Laboratory, Golden 2006)

27.35   R.L. Costa, P.G. Grimes: Electrolysis as a source of hydrogen and oxygen, Chem. Eng. Prog. 63(4), 56–58 (1967)

27.36   J. Fischer, H. Hofmann, G. Luft, H. Wendt: Fundamental investigations and electrochemical engineering aspects concerning an advanced concept for alkaline water electrolysis, AIChE J. 26(5), 794–802 (1980)

27.37 P. Vermeiren, W. Adriansens, J.P. Moreels, R. Leysen: Evaluation of the Zirfon separator for use in alkaline water electrolysis and Ni-H2 batteries, Int. J. Hydrogen Energy **23**(5), 321–324 (1998)

27.38 K. Zeng, D. Zhang: Recent progress in alkaline water electrolysis for hydrogen production and applications, Prog. Energ. Combust. Sci. **36**(3), 307–326 (2010)

27.39 M. Raney: Method of preparing catalytic nickel, US Patent Application 1 563 587 (1925)

27.40 M. Raney: Method of producing finely-divided nickel, US Patent Application 1 628 190 (1927)

27.41 E. Justi, W. Scheible, A. Winsel: Doppelskelett-Katalysator-Elektrode, German Patent Application DE1 019 361 (1954)

27.42 I. Abe, T. Fujimaki, M. Matsubara: Hydrogen production by high-temperature high-pressure water electrolysis; results of test plant operation, Int. J. Hydrogen Energy **9**(9), 753–758 (1984)

27.43 W. Vielstich, E. Knauf: Investigation of nickel whisker networks as electrodes for hydrogen and oxygen evolution comments, J. Electrochem. Soc. **129**(6), 1273 (1982)

27.44 J. De Carvalho, G. Tremiliesi-Filho, L.A. Avaca, E.R. Gonzalez: Iron-based coatings for hydrogen evolution in alkaline solutions, Adv. Hydrogen Energ. **5**, 250–257 (1986)

27.45 I.A. Raj, V.K. Venkatesan: Investigations on the adoptability of electrocatalytic nickel-molybdenum-iron alloy cathode to industrial water electrolysis, Trans. SAEST **22**(4), 189–197 (1987)

27.46 H. Wendt, G. Imarisio: Nine years of research and development on advanced water electrolysis. A review of the research program of the Commission of the European Communities, J. Appl. Electrochem. **18**(1), 1–14 (1988)

27.47 K. Kinoshita: *Electrochemical Oxygen Technology* (Wiley, New York 1992)

27.48 R. Tunold, A.T. Marshall, E. Rasten, M. Tsypkin, L.E. Owe, S. Sunde: Materials for electrocatalysis of oxygen evolution process in PEM water electrolysis cells, ECS Trans. **25**(23), 103–117 (2010)

27.49 S.A. Grigoriev, V.I. Porembsky, V.N. Fateev: Pure hydrogen production by PEM electrolysis for hydrogen energy, Int. J. Hydrogen Energy **31**(2), 171–175 (2006)

27.50 A. Marshall, B. Borresen, G. Hagen, M. Tsypkin, R. Tunold: Hydrogen production by advanced proton exchange membrane (PEM) water electrolysers-reduced energy consumption by improved electrocatalysis, Energy **32**(4), 431–436 (2006)

27.51 P.W.T. Lu, S. Srinivasan: Advances in water electrolysis technology with emphasis on use of the solid polymer electrolyte, J. Appl. Electrochem. **9**(3), 269–283 (1979)

27.52 F. Barbir: PEM electrolysis for production of hydrogen from renewable energy sources, Sol. Energ. **78**(5), 661–669 (2005)

27.53 O. Savadogo: Water electrolysis in acid medium, Hem. Ind. **54**(3), 95–101 (2000)

27.54 A. Di Blasi, C. D'Urso, V. Baglio, V. Antonucci, A.S. Arico, R. Ornelas, F. Matteucci, G. Orozco, D. Beltran, Y. Meas, L.G. Arriaga: Preparation and evaluation of RuO2-IrO2, IrO2-Pt and IrO2- Ta2O5 catalysts for the oxygen evolution reaction in an SPE electrolyzer, J. Appl. Electrochem. **39**(2), 191–196 (2009)

27.55 A. Marshall, B. Borresen, G. Hagen, S. Sunde, M. Tsypkin, R. Tunold: Iridium oxide-based nanocrystalline particles as oxygen evolution electrocatalysts, Russ. J. Electrochem. **42**(10), 1134–1140 (2006)

27.56 A.T. Marshall, S. Sunde, M. Tsypkin, R. Tunold: Performance of a PEM water electrolysis cell using $Ir_x Ru_y Ta_z O_2$ electrocatalysts for the oxygen evolution electrode, Int. J. Hydrogen Energy **32**(13), 2320–2324 (2007)

27.57 A. Marshall, B. Borresen, G. Hagen, M. Tsypkin, R. Tunold: Preparation and characterization of nanocrystalline $Ir_xSn_1-xO_2$ electrocatalytic powders, Mater. Chem. Phys. **94**(2–3), 226–232 (2005)

27.58 P. Millet, N. Mbemba, S.A. Grigoriev, V.N. Fateev, A. Aukauloo, C. Etiévant: Electrochemical performances of PEM water electrolysis cells and perspectives, Int. J. Hydrogen Energy **36**(6), 4134–4142 (2010)

27.59 S.A. Grigoriev, P. Millet, V.N. Fateev: Evaluation of carbon-supported Pt and Pd nanoparticles for the hydrogen evolution reaction in PEM water electrolyzers, J. Power Sources **177**(2), 281–285 (2008)

27.60 O. Pantani, E. Anxolabehere-Mallart, A. Aukauloo, P. Millet: Electroactivity of cobalt and nickel glyoximes with regard to the electro-reduction of protons into molecular hydrogen in acidic media, Electrochem. Commun. **9**(1), 54–58 (2006)

27.61 P. Millet, R. Ngameni, S.A. Grigoriev, N. Mbemba, F. Brisset, A. Ranjbari, C. Etiévant: PEM water electrolyzers: From electrocatalysis to stack development, Int. J. Hydrogen Energy **35**(10), 5043–5052 (2010)

27.62 M.A. Yandrasits, S.J. Hamrock: Membranes for PEM fuel cells, ACS Symp. Ser. **1040**, 15–29 (2010)

27.63 A.E. Steck: *Membrane Materials in Fuel Cells* (Editions de l'Ecole Polytechnique de Montreal, Montreal 1995)

27.64 L.M. Roen, C.H. Paik, T.D. Jarvi: Electrocatalytic corrosion of carbon support in PEMFC cathodes, Electrochem. Solid-State Lett. **7**(1), A19–A22 (2004)

27.65 H.-Y. Jung, S.-Y. Huang, P. Ganesan, B.N. Popov: Performance of gold-coated titanium bipolar plates in unitized regenerative fuel cell operation, J. Power Sources **194**(2), 972–975 (2009)

27.66 T. Smolinka, S. Rau, C. Hebling: PEM water electrolysis. In: *Hydrogen and Fuel Cells*, ed. by D. Stolten (Wiley-VCH, Weinheim 2010)

27.67 A.B. LaConti, L. Swette: Special application using PEM-technology. In: *Handbook of Fuel Cells*, Vol. 4, ed. by W. Vielstich, A. Lamm, H.A. Gasteiger (Wiley, Chichester 2003)

27.68 J. Van Herle, A.J. McEvoy, K. Ravindranathan Thampi: Conductivity measurements of various yttria-stabilized zirconia samples, J. Mater. Sci. **29**, 3691 (1994)

27.69   J. Fergus: Electrolytes for solid oxide fuel cells, J. Power Sources **162**, 30 (2006)

27.70   B. Dalslet, P. Blennow, P.V. Hendriksen, N. Bonanos, D. Lybye, M. Mogensen: Assessment of doped ceria as electrolyte, J. Solid State Electrochem. **10**, 547–561 (2006)

27.71   K. Schwarz: Materials design of solid electrolytes, Proc. Nat. Acad. Sci. **103**(10), 3497 (2006)

27.72   D.A. Andersen, S.I. Simak, N.V. Skorodumova, I.A. Abrikosov, B. Johansson: Optimization of ionic conductivity in doped ceria, Proc. Nat. Acad. Sci. **103**(10), 3518–3521 (2006)

27.73   H, Yahiro, K. Eguchi, H. Arai: Electrical properties and reducibilities of ceria-rare earth oxide systems and their application to solid oxide fuel cell, Solid State Ion. **36**(1–2), 71–75 (1989)

27.74   D.J. Seo, K.O. Ryo, S.B. Park, K.Y. Kim, R.-H. Song: Synthesis and properties of $Ce_{1-x}Gd_xO_{2-x/2}$ solid solution prepared by flame spray pyrolysis, Mater. Res. Bull. **41**, 359–366 (2006)

27.75   T. Sakai, S. Matsushita, H. Matsumoto, S. Okada, S. Hashimoto, T. Ishihara: Intermediate temperature steam electrolysis using strontium zirconate-based protonic conductors, Int. J. Hydrogen Energy **34**, 56–63 (2009)

27.76   J.S. Herring, J.E. O'Brien, C.M. Stoots, G.L. Hawkes, J.J. Hartvigsen, M. Shahnam: Progress in high-temperature electrolysis for hydrogen production using planar SOFC technology, Int. J. Hydrogen Energy **32**, 440–450 (2007)

27.77   M. Ni, K.H. Leung, D.Y.C. Leung: Technological development of hydrogen production by solid oxide electrolyzer cell (SOEC), Int. J. Hydrogen Energy **33**, 2337–2354 (2008)

27.78   A. Hauch, S.H. Jensen, S. Ramousse, M. Mogensen: Performance and durability of solid oxide electrolysis cells, J. Electrochem. Soc. **153**(9), A1741–A1747 (2006)

27.79   A. Momma, T. Kato, Y. Kaga, S. Nagata: Polarization behavior of high temperature solid oxide electrolysis cells (SOEC), J. Ceram. Soc. Jpn. **105**, 369–373 (1997)

27.80   A. Hauch, S.H. Jense, M. Mogensen: Ni/YSZ electrodes in solid oxide electrolyser cells, Proc. 26th Risø Int. Symp. Mater. Sci.: Solid State Electrochem., ed. by S. Linderoth, A. Smith, N. Bonano, A. Hagen, L. Mikkelson, K. Kammer, D. Lybye, P.V. Hendriksen, F.W. Poulsen, M. Mogensen, W.G. Wang (Risø National Laboratory, Roskilde 2005) p. 203

27.81   P. Kim-Lohnsoontorn, Y.-M. Kim, N. Laosiripojana: Gadolinium doped ceria-impregnated nickel–yttria stabilised zirconia cathode for solid oxide electrolysis cell, Int. J. Hydrogen Energy **36**, 9420–9427 (2011)

27.82   J. Kong, Y. Zhang, C. Deng, J. Xu: Synthesis and electrochemical properties of LSM and LSF perovskites as anode materials for high temperature steam electrolysis, J. Power Sources **186**, 485–489 (2009)

27.83   W. Wang, Y. Juang, S. Jung, J. Vohs, J. Gorte: A Comparison of LSM, LSF, and LSCo for solid oxide

27.84   O.A. Marina, L.R. Pederson, M.C. Williams, G.W. Coffey, K.D. Meinhardt, C.D. Nguyen, E.C. Thomsen: Electrode performance in reversible solid oxide fuel cells, J. Electrochem. Soc. **154**(5), B452–B459 (2007)

27.85   M.K. Mahapatra, S. Bhowmick, N. Li, P. Singh: Role of oxygen pressure on the stability of lanthanum strontium manganite–yttria stabilized zirconia composite, J. Eur. Ceram. Soc. **32**(10), 2341–2349 (2012)

27.86   S.H. Jensen, P. Larsen, M. Mogensen: Hydrogen and synthetic fuel production from renewable energy sources, Int. J. Hydrogen Energy **32**, 3253–3257 (2007)

27.87   S. Ebbesen, M. Mogensen: Exceptional durability of solid oxide cells, Electrochem. Solid-State Lett. **13**(9), B106–B108 (2010)

27.88   J.E. O'Brien, J.S. Herring, C.M. Stoots, G.L. Hawkes, J.J. Hartvigsen, M. Shahnam: Progress in high-temperature electrolysis for hydrogen production using planar SOFC technology, Proc. AIChE Spring Nat. Meet. '05 (2005), Idaho National Laboratory (INL)/CON-05-00078 Rep.

27.89   J. O'Brien, C. Stoots, J. Herring, G. Hawkes, J. Hartvigsen: Thermal and electrochemical performance of a high-temperature steam electrolysis stack, Fuel Cell Seminar, Idaho National Laboratory (INL) (2006), /CON-06-11716 Rep.

27.90   J.E. O'Brien, J.S. Herring, C.M. Stoots, M.G. McKellar, E.A. Harvego, K.G. Condie, G.K. Housley, J.J. Hartvigsen: Status of the INL high-temperature electrolysis research program – Experimental and modeling, Proc. 4th Information Exchange Meeting on the Nuclear Production of Hydrogen (2009), Idaho National Laboratory (INL)/CON-09-15618 Rep.

27.91   J.E. O'Brien, C.M. Stoots, J.S. Herring, M.G. McKellar, E.A. Harvego, M.S. Sohal, K.G. Condie: High temperature electrolysis for hydrogen production from nuclear energy – Technology summary, Proc. Idaho National Laboratory (INL) (2010), EXT-09-16140 Rep.

27.92   Y. Bo, Z. Wenqiang, X. Jingming, C. Jing: Status and research of highly efficient hydrogen production through high temperature steam electrolysis at INET, Int. J. Hydrogen Energy **35**, 2829–2835 (2010)

27.93   S.-D. Kim, J.-H. Yu, D.-W. Seo, I.-S. Han, S.-K. Woo: Hydrogen production performance of 3-cell flat-tubular solid oxide electrolysis stack, Int. J. Hydrogen Energy **37**, 78–83 (2012)

27.94   S.D. Kim, S.H. Hyun, J. Moon, J.-H. Kim, R.H. Song: Fabrication and characterization of anode-supported electrolyte thin films for intermediate temperature solid oxide fuel cells, J. Power Sources **139**, 67–72 (2005)

27.95   M.A. Laguna-Bercero, R. Campana, A. Larrea, J.A. Kilner, V.M. Orera: Steam electrolysis using a microtubular solid oxide fuel cell, J. Electrochem. Soc. **157**(6), B852–B855 (2010)

27.96 J.P. Ouweltjes, L. Berkeveld, B. Rietveld: Recent progress in the development of solid oxide electrolyzers at ECN, Proc. 18th World Hydrogen Energy Conference, Essen '10 (2010)

27.97 A. Glauche, T. Betz, M. Ise: Product development for SOFC and SOE, App. ECS Trans. **35**(1), 157–165 (2011)

27.98 A. Hauch, S.J. Jensen, S.D. Ebbesen, M. Mogensen: Durability of solid oxide cells for hydrogen production. In: *Energy Solutions for Sustainable Development*, ed. by L.S. Petersen, H. Larsen (Risø National Laboratory, Risø 2007) pp. 327–338

27.99 J. Schefold, A. Brisse, F. Tietz: Nine thousand hours of operation of a solid oxide cell in steam electrolysis mode, J. Electrochem. Soc. **159**(2), A137–A144 (2012)

27.100 E. Elangoven, J. Hartvigsen: Progress in the conversion of CO_2 to liquid fuel, Proc. 220th ECS Meeting and Electrochemistry Summit, Boston (2011) p. 1509

27.101 A.V. Virkar: A model for solid oxide fuel cell (SOFC) stack degradation, J. Power Sources **172**, 713–724 (2007)

27.102 S.H. Jensen, M. Mogensen: *Perspectives of high Temperature Electrolysis Using SOEC* (European Institute of Energy Research (EIfER), Karlsruhe 2015), http://www.hi2h2.com/perspectives.htm

27.103 S.D. Ebbesen, J. Hogh, K.A. Nielsen, J.U. Nielsen, M. Mogensen: Durable SOC stacks for production of hydrogen and synthesis gas by high temperature electrolysis, Int. J. Hydrogen Energy **36**, 7363–7373 (2011)

27.104 S.D. Ebbesen, C. Graves, A. Hauch, S. Jensen, M. Mogensen: Poisoning of solid oxide electrolysis cells by impurities, J. Electrochem. Soc. **157**(10), B1419–B1429 (2010)

27.105 M.S. Sohal, J.E. O'Brien, C.M. Stoots, V.I. Sharma, B. Yildiz, A. Virkar: Degradation issues in solid oxide cells during high temperature electrolysis, J. Fuel Cell Sci. Technol. **9**(1), 011017 (2012)

27.106 K. Chen, S.P. Jiang: Failure mechanism of $(La,Sr)MnO_3$ oxygen electrodes of solid oxide electrolysis cells, Int. J. Hydrogen Energy **36**, 10541–10549 (2011)

27.107 A. Hauch, S.D. Ebbesen, S.H. Jensen, M.J. Mogensen: Highly efficient high temperature electrolysis, Mater. Chem. **18**, 2331–2340 (2008)

27.108 J.R. Bolton, S.J. Strickler, J.S. Connolly: Limiting and realizable efficiencies of solar photolysis of water, Nature **316**, 495–500 (1985)

27.109 A.V. Virkar: Mechanism of oxygen electrode delamination in solid oxide electrolyzer cells, Int. J. Hydrogen Energy **35**, 9527–9543 (2010)

27.110 C.W. De Kreuk, J.L.B. De Groot: Photocorrosion of strontium titanate photoanodes, Solar Energy Mater. **5**(4), 437–444 (1981)

27.111 M.C. Hanna, A. Nozik: Solar conversion efficiency of photovoltaic and photoelectrolysis cells with carrier multiplication absorbers, J. Appl. Phys. **100**(074510), 1–8 (2006)

27.112 R. Memming, G. Schandt: Electrochemical properties of gallium phosphide in aqueous solutions, Electrochimica Acta. **13**, 1299–1310 (1968)

27.113 H. Yoneyama, H. Sakamoto, H.A. Tamura: Photoelectrochemical cell with production of hydrogen and oxygen by a cell reaction, Electrochimica Acta. **20**, 341–345 (1975)

27.114 B.A. Parkinson: Combinatorial identification and optimization of new oxide semiconductors. In: *Photoelectrochemical Hydrogen Production*, ed. by V. De Krol, R.M. Grätzel (Springer, Berlin 2012) pp. 173–203

27.115 Y. Matsumoto: Energy positions of oxide semiconductors and photocatalysis with iron complex oxides, J. Solid State Chem. **126**, 227–234 (1996)

27.116 M.G. Walter, E.L. Warren, J.R. McKone, S.W. Boettcher, Q. Mi, E.A. Santori, N.S. Lewis: Solar water splitting cells, Chem. Rev. **110**, 6446–6473 (2010)

27.117 O. Khaselev, J.A. Turner: Electrochemical stability of p-$GaInP_2$ in aqueous electrolytes toward photoelectrochemical water splitting, J. Electrochem. Soc. **145**(10), 3335–3339 (1998)

27.118 B. Miller: Charge transfer and corrosion processes at III–V semiconductor/electrolyte interfaces, J. Electroanal. Chem. Interf. Electrochem. **168**(1), 91–100 (1984)

27.119 T.G. Deutsch, C.A. Koval, J.A. Turner: III–V Nitride epilayers for photoelectrochemical water splitting: GaPN and GaAsPN, J. Phys. Chem. B **110**, 25297–25307 (2006)

27.120 H. Gerischer: On the stability of semiconductor electrodes against photodecomposition, J. Electroanal. Chem. Interf. Electrochem. **82**(1), 133–143 (1977)

27.121 D. Meissner, R. Memming, B. Kastening: Fundamental problems of water splitting at cadmium sulfide, Chem. Phys. Lett. **127**, 419–422 (1986)

27.122 D. Meissner, C. Benndorf, R. Memming: Photocorrosion of cadmium sulfide: Analysis by photoelectron spectroscopy, Appl. Surf. Sci. **27**, 423–436 (1987)

27.123 D. Meissner, R. Memming: Photoelectrochemistry of cadmium sulfide. 1. Reanalysis of photocorrosion and flat–band potential, J. Phys. Chem. **92**, 3476–3483 (1988)

27.124 R.C. Valderrama, P.J. Sebastián, M. Miranda–Hernandez, J. Pantoja Enriquez, S.A. Gamboa: Studies on the electrochemical stability of CIGS in H_2SO_4, J. Photochem. Photobiol. A **168**(1), 75–80 (2004)

27.125 W. Kautek, H. Gerischer: Anisotropic photocorrosion of n–type MoS_2 $MoSe_2$, and WSe_2 single crystal surfaces: The role of cleavage steps, line and screw dislocations, Surf. Sci. **119**(1), 46–60 (1982)

27.126 D.E. Scaife: Oxide semiconductors in photoelectrochemical conversion of solar energy, Solar Energy **25**(1), 41–54 (1980)

27.127 U. Bossel: The physics of the hydrogen economy, Eur. Fuel Cells News **10**(2), 1–16 (2003)

27.128 K. Tanabe: A review of ultrahigh efficiency III–V semiconductor compound solar cells: Multijunction tandem, lower dimensional, photonic up/down conversion and plasmonic nanometallic structures, Energies **2**, 504–530 (2009)

27.129 S. Licht: Multiple band gap semiconductor/electrolyte solar energy conversion, J. Phys. Chem. B **105**, 6281–6294 (2001)

27.130 B. Neumann, P. Bogdanoff, H. Tributsch: TiO_2-protected photoelectrochemical tandem $Cu(In,Ga)Se_2$ thin film membrane for light-induced water splitting and hydrogen evolution, J. Phys. Chem. C **113**, 20980–20989 (2009)

27.131 W. Shockley, H.J. Queisser: Detailed balance limit of efficiency of p–n junction solar cells, J. Appl. Phys. **32**, 510–519 (1961)

27.132 N.D. McDaniel, S. Bernhard: Solar fuels: thermodynamics, candidates, tactics, and figures of merit, Dalton Trans. **39**, 10021–10030 (2010)

27.133 J.M. Bolts, M.S. Wrighton: Correlation of photocurrent–voltage curves with flat–band potential for stable photoelectrodes for the photoelectrolysis of water, J. Phys. Chem. **80**(24), 2641–2645 (1976)

27.134 J. Maclay, J. Brouwer, G.S. Samuelsen: Experimental results for hybrid energy storage systems coupled to photovoltaic generation in residential applications, Int. J. Hydrogen Energy **36**(19), 12130–12140 (2011)

27.135 A.J. Nozik: p–n photoelectrolysis cells, Appl. Phys. Lett. **29**, 150–153 (1976)

27.136 J. o'M. Bockris, R.C. Kainthla: The conversion of light and water to hydrogen and electric power, Int. J. Hydrogen Energy **13**(6), 375–383 (1988)

27.137 D.C. Bookbinder, N.S. Lewis, M.G. Bradley, A.B. Bocarsly, M.S. Wrighton: Photoelectrochemical reduction of N,N′-dimethyl-4,4′-bipyridinium in aqueous media at p-type silicon: Sustained photogeneration of a species capable of evolving hydrogen, J. Am. Chem. Soc. **101**(26), 7721–7723 (1979)

27.138 E. Aharon-Shalom, A. Heller: Efficient p-InP(Rh-H alloy) and p-InP(Re-H alloy) hydrogen evolving photocathodes, J. Electrochem. Soc. **129**, 2865–2866 (1982)

27.139 K. Ohashi, J. McCann, J.O.M. Bockris: Stable photoelectrochemical cells for the splitting of water, Nature **266**, 610–611 (1977)

27.140 H.S. Gurev, R.E. Hahn, K.D. Masterson: High temperature; stable, spectrally selective solar absorbers for thermochemical hydrogen production, Int. J. Hydrogen Energy **1**(3), 259–265 (1977)

27.141 B. Marsen, B. Cole, E.L. Miller: Photoelectrolysis of water using thin copper gallium diselenide electrodes, Sol. Energ. Mater. Sol. Cells **92**, 1054–1058 (2008)

27.142 D. Yokoyama, T. Minegishi, K. Jimbo, T. Hisatomi, G. Ma, M. Katayama, J. Kubota, H. Katagiri, K. Domen: H_2 evolution from water on modified Cu_2ZnSnS_4 photoelectrode under solar light, Appl. Phys. Express **3**(10), 101202–101204 (2010)

27.143 M. Kaneko, G.J. Yao, A. Kira: Efficient water cleavage with visible light by a system mimicking photosystem II, J. Chem. Soc. Chem. Commun. **18**, 1338–1339 (1989)

27.144 J. Hensel, G. Wang, Y. Li, J.Z. Zhang: Synergistic effect of CdSe quantum dot sensitization and nitrogen doping of TiO_2 nanostructures for photoelectrochemical solar hydrogen generation, Nano Lett. **10**, 478–483 (2010)

27.145 H. Hashiguchi, K. Maeda, R. Abe, A. Ishikawa, J. Kubota, K. Domen: Photoresponse of GaN: ZnO Electrode on FTO under visible light irradiation, Bull. Chem. Soc. Jpn. **82**, 401–407 (2009)

27.146 S. Yamane, N. Kato, S. Kojima, A. Imanishi, S. Ogawa, N. Yoshida, S. Nonomura, Y. Nakato: Efficient solar water splitting with a composite n-Si/p-CuI/n-i-p a-Si/n-p GaP/RuO₂, semiconductor electrode, J. Phys. Chem. C **113**(32), 14575–14581 (2009)

27.147 S. Shet, K.-S. Ahn, T. Deutsch, H. Wang, N. Ravindra, Y. Yan, J. Turner, M. Al-Jassim: Synthesis and characterization of band gap–reduced ZnO:N and ZnO:(Al,N) films for photoelectrochemical water splitting, J. Mater. Res. **25**(1), 69–75 (2010)

27.148 J. Ye, Z. Zou, H. Arakawa, M. Oshikiri, M. Shimoda, A. Matsushita, T. Shishido: Correlation of crystal and electronic structures with photophysical properties of water splitting photocatalysts $InMO_4$ (M=V5+,Nb5+,Ta5+), J. Photochem. Photobiol. A **148**, 79–83 (2002)

27.149 Z.G. Zou, J.H. Ye, K. Sayama, H. Arakawa: Direct splitting of water under visible light irradiation with an oxide semiconductor photocatalyst, Nature **414**, 625–627 (2001)

27.150 G. Hodes, D. Cahen, J. Manassen: Tungsten trioxide as a photoanode for a photoelectrochemical cell (PEC), Nature **260**, 312–313 (1976)

27.151 Y. Shimodaira, H. Kato, H. Kobayashi, A. Kudo: Investigations of electronic structures and photocatalytic activities under visible light irradiation of lead molybdate replaced with chromium (VI), Bull. Chem. Soc. Jpn. **80**, 885–893 (2007)

27.152 M.S. Wrighton, A.B. Ellis, P.T. Wolczanski, D.L. Morse, H.B. Abrahamson, D.S. Ginley: Strontium titanate photoelectrodes. Efficient photoassisted electrolysis of water at zero applied potential, J. Am. Chem. Soc. **98**(10), 2774–2779 (1975)

27.153 H.P. Maruska, A.K. Ghosh: Transition-metal dopants for extending the response of titanate photoelectrolysis anodes, Sol. Energ. Mater. **1**(3–4), 237–247 (1978)

27.154 L.G.L. De Haart, A.J. De Vries, G. Blasse: On the photoluminescence of semiconducting titanates applied in photoelectrochemical cells, J. Sol. State Chem. **59**(3), 291–300 (1985)

27.155 K. Sivula, F. Le Formal, M. Grätzel: Solar water splitting: progress using hematite (α-Fe(2) O(3)) photoelectrodes, Chem. Sus. Chem. **4**(4), 432–449 (2011)

27.156 P.C. Bailey: Absorption and reflectivity measurements on some rare earth iron garnets and alpha–

iron oxide, J. Appl. Phys. **31**, S39–S40 (1960)

27.157 L.A. Marusak, R. Messier, W.B. White: Optical absorption spectrum of hematite, α Fe$_2$O$_3$ near IR to UV, J. Phys. Chem. Solids **41**, 981–984 (1980)

27.158 J.H. Kennedy, K.W. Frese: Photo oxidation of water at α–Fe$_2$O$_3$ electrodes, J. Electrochem. Soc. **125**, 709–714 (1978)

27.159 A. Kay, I. Cesar, M. Grätzel: New benchmark for water photooxidation by nanostructured α – Fe$_2$O$_3$ films, J. Am. Chem. Soc. **128**(49), 15714–15721 (2006)

27.160 K. Sivula, F.L. Formal, M. Grätzel: WO$_3$–Fe$_2$O$_3$ photoanodes for water splitting: a host scaffold, guest absorber approach, Chem. Mater. **21**(13), 2862–2867 (2009)

27.161 K. Sivula, R. Zboril, F. Le Formal, R. Robert, A. Weidenkaff, J. Tucek, J. Frydrych, M. Grätzel: Photoelectrochemical water splitting with mesoporous hematite prepared by a solution-based colloidal approach, J. Am. Chem. Soc. **132**(21), 7436–7444 (2010)

27.162 S.D. Tilley, M. Cornuz, K. Sivula, M. Grätzel: Light-induced water splitting with hematite: Improved nanostructure and iridium oxide catalysis, Angew. Chem. Intl. Ed. **49**(36), 6405–6408 (2010)

27.163 A. Paracchino, V. Laporte, K. Sivula, M. Gräzel, E. Thimsen: Highly active oxide photocathode for photoelectrochemical water reduction, Nature Mater. **10**, 456–461 (2011)

27.164 Y. Matsumoto, M. Omae, K. Sugiyama, E.-I. Sato: New photocathode materials for hydrogen evolution: Calcium iron oxide (CaFe$_2$O$_4$) and strontium iron oxide (Sr$_7$Fe$_{10}$O$_{22}$), J. Phys. Chem. **91**, 577–581 (1987)

27.165 A.J. Nozik: Nanoscience and nanostructures for photovoltaics and solar fuels, Nano Lett. **10**(8), 2735–2741 (2010)

27.166 O.K. Varghese, D. Gong, M. Pailose, C.A. Grimes, E.C. Dickey: Crystallization and high-temperature structural stability of titanium oxide nanotube arrays, J. Mater. Res. **18**, 156–165 (2003)

27.167 K.S. Raja, M. Misra, K. Paramguru: Formation of self-ordered nano-tubular structure of anodic oxide layer on titanium, Electrochimica. Acta. **51**, 154–165 (2005)

27.168 C.-C. Chen, J.-H. Chen, C.-G. Chao, W.C. Say: Electrochemical characteristics of surface of titanium formed by electrolytic polishing and anodizing, J. Mater. Sci. **40**, 4053–4059 (2005)

27.169 J. Zhao, X. Wnag, R. Chen, L. Li: Fabrication of titanium oxide nanotube arrays by anodic oxidation, Sol. State Commun. **134**, 705–710 (2005)

27.170 S. Bauer, S. Kleber, P. Schmuki: TiO$_2$ nanotubes: Tailoring the geometry in H$_3$PO$_4$/HF electrolytes, Electrochem. Commun. **8**(8), 1321–1325 (2006)

27.171 P.S. Albu, A. Ghicov, J.M. Macak, P. Schmuki: 250 μm long anodic TiO$_2$ nanotubes with hexagonal self-ordering, Phys. Status Solidi **1**, R65–R67 (2007)

27.172 W.-J. Lee, M. Alhoshan, W.H. Smyrl: Titanium dioxide nanotube arrays fabricated by anodizing

27.173 Y.-C. Nah, A. Ghicov, D. Kim, S. Berger, P. Schmuki: TiO$_2$–WO$_3$ Composite nanotubes by alloy anodization: Growth and enhanced electrochromic properties, J. Am. Chem. Soc. **130**, 16154–16155 (2008)

27.174 J.H. Park, S. Kim, A.J. Bard: Novel carbon-doped TiO$_2$ nanotube arrays with high aspect ratios for efficient solar water splitting, Nano Lett. **6**(1), 24–28 (2005)

27.175 K.S. Raja, M. Misra, V.K. Mahajan, T. Gandhi, P. Pillai, S.K. Mohapatra: Photo-electrochemical hydrogen generation using band-gap modified nanotubular titanium oxide in solar light, J. Power Sources **161**, 1450–1457 (2006)

27.176 S.K. Mohapatra, M. Misra, V.K. Mahajan, K.S. Raja: Design of a highly efficient photoelectrolytic cell for hydrogen generation by water splitting: Application of TiO$_{2-x}$C$_x$ nanotubes as a photoanode and Pt/TiO$_2$ nanotubes as a cathode, J. Phys. Chem. C **111**, 8677–8685 (2007)

27.177 R. Abe, M. Higashi, K. Domen: Facile fabrication of an efficient oxynitride TaON photoanode for overall water splitting into H$_2$ and O$_2$ under visible light irradiation, J. Am. Chem. Soc. **132**(34), 11828–11829 (2010)

27.178 S. Linic, P. Christopher, D. Ingram: Plasmonic-metal nanostructures for efficient conversion of solar to chemical energy, Nature Mater. **10**, 911–921 (2011)

27.179 D.B. Ingram, S. Linic: S: Water splitting on composite plasmonic-metal/semiconductor photoelectrodes: Evidence for selective plasmon-induced formation of charge carriers near the semiconductor surface, J. Am. Chem. Soc. **133**, 5202–5205 (2011)

27.180 J.I. Levene, M.K. Mann, R.M. Magrolis, A. Milbrandt: An analysis of hydrogen production from renewable electricity sources, Solar Energ. **81**, 773–780 (2007)

27.181 P.-H. Floch, S. Gabriel, C. Mansilla, F. Werkoff: On the production of hydrogen via alkaline electrolysis during off-peak periods, Int. J. Hydrogen Energy **32**, 4641–4647 (2007)

27.182 IEA: *CO$_2$ Emissions from Fuel Combustion* (International Energy Agency, Paris 2011)

27.183 D. Bonhaquist: *Emissions, Reductions, and Capture for Large-Scale Hydrogen Production Plants*, Praxair White Paper (Praxair, Danbury 2010)

27.184 L.M. Gandia, R. Orosz, A. Ursua, P. Sanchis, P. Diegueuz: Renewable hydrogen production: Performance of an alkaline water electrolyzer working under emulated wind conditions, Energy Fuels **21**, 1699–1706 (2007)

27.185 B. Kroposki, J. Levene, K. Harrison, P.K. Sen, F. Novachek: *Electrolysis: Information and Opportunities for Electric Power Utilities* (National Renewable Energy Laboratory, Golden 2006), NREL Tech. Rep. NREL/TP-581-40605

27.186 T. Abbasi, S.A. Abbasi: Renewable hydrogen: Prospects and challenges, Renew. Sust. Energ.

Part E | 27

Rev. **15**, 3034 (2011)

27.187 National Research Council: *The Hydrogen Economy. Opportunities, Costs, Barriers, and R and D Needs* (National Academies, Washington 2004)

27.188 J.E. O'Brien, M.G. McKellar, E.A. Harvego, C.M. Stoots: High-temperature electrolysis for large-scale hydrogen and syngas production from nuclear energy – Summary of system simulation and economic analyses, Int. J. Hydrogen Energy **35**, 4808–4819 (2010)

27.189 B.C.R. Ewan, R.W.K. Allen: A figure of merit assessment of the routes to hydrogen, Int. J. Hydrogen Energy **30**, 809–819 (2005)

27.190 P.L. Spath, M.K. Mann: *Life Cycle Assessment of Renewable Hydrogen Production via Wind/Electrolysis* (National Renewable Energy Laboratory, Golden 2004), NREL Milestone Rep. MP-560-35404

27.191 C. Koronos, A. Dompros, G. Roumbas, N. Moussiopoulos: Life cycle assessment of hydrogen fuel production processes, Int. J. Hydrogen Energy **29**, 1443–1450 (2010)

27.192 R.G. Lemus, J.M.M. Duart: Updated hydrogen production costs and parities for conventional and renewable technologies, Int. J. Hydrogen Energy **35**, 3929–3936 (2010)

27.193 E. Cetinkaya, I. Dincer, G.F. Naterer: Life cycle assessment of various hydrogen production methods, Int. J. Hydrogen Energy **37**, 2071–2080 (2012)

27.194 A. Ursua, L.M. Gandia, P. Sanchis: Hydrogen production from water electrolysis: Current status and future trends, Proc. IEEE, Vol. 100 (2012) pp. 410–426

27.195 K.W. Harrison, G.D. Martin, T.G. Ramsden, W.E. Kramer, F.J. Novachek: *The Wind-to-Hydrogen Project: Operational Experience, Performance Testing, and Systems Integration* (National Renewable Energy Laboratory, Golden 2009), NREL TP/550-44082 Tech. Rep.

27.196 M. Rey Porto, T. Carretero, M. Aguado, R. Garde: H_2 production in Sotavento wind farm, Proc. 18th World Hydrogen Energy Conf., Vol. 78, ed. by D. Stolten, T. Grube (2010)

27.197 K.W. Harrison, R. Remick, G.D. Martin, A. Hoskin: *Hydrogen Production: Fundamentals and Case Study Summaries* (National Renewable Energy Laboratory, Golden 2010), NREL CP-550-47302 Tech. Rep.